

SURFACE ELECTROMAGNETIC WAVES GUIDED BY
INTERFACES WITH ISOTROPIC CHIRAL AND
UNIAXIALLY CHIRAL MATERIALS



By
Maimoona Naheed

SUBMITTED IN PARTIAL FULFILLMENT OF THE
REQUIREMENTS FOR THE DEGREE OF
DOCTOR OF PHILOSOPHY
AT
QUAID-I-AZAM UNIVERSITY
ISLAMABAD, PAKISTAN
AUGUST 2021

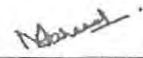


QUAID-I-AZAM UNIVERSITY
Department of Electronics

Certificate of Approval


This is to certify that the research work presented in this thesis, entitled "Surface Electromagnetic Waves Guided by Interfaces with Isotropic Chiral and Uniaxially Chiral Materials" was conducted by Ms. Maimoona Naheed under the supervision of Dr. Muhammad Farvad and co-supervision of Prof. Dr. Qaisar A. Naqvi. No part of this thesis has been submitted anywhere else for any other degree. This thesis is submitted to the Department of Electronics, Quaid-i-Azam University in partial fulfilment of the requirements for the degree of Doctor of Philosophy in Field of Electronics, Department of Electronics, Quaid-i-Azam University.

Student Name: Ms. Maimoona Naheed

Signature: 

Examination Committee:

A. Prof. Dr. Muhammad Junaid Mughal
Department of Electronics Engineering
Citt. Park Road Chak Shahzad Islamabad.

Signature: 


B. Dr. Akhtar Hussain
General Manager
P.O. Box 1702
National Development Complex (NDC), Islamabad.

Signature: 

C. Dr. Muhammad Farvad
Assistant Professor & Supervisor
Babar Ali School of Science & Engineering
LUMS Lahore.

Signature: _____

D. Prof. Dr. Qaisar Abbas Naqvi
Professor & Co-Supervisor
Department of Electronics
Quaid-i-Azam University, Islamabad.

Signature: 


Supervisor Name: Dr. Muhammad Farvad

Signature: _____

Co-Supervisor Name: Prof. Dr. Qaisar Abbas Naqvi

Signature: _____

Name of Chairman: Prof. Dr. Syed Aqeel A. Bukhari

Signature: 



QUAID-I-AZAM UNIVERSITY
Department of Electronics

Author's Declaration

I, Maimoona Naheed hereby state that my PhD thesis titled "Surface Electromagnetic Waves Guided by Interfaces with Isotropic Chiral and Uniaxially Chiral Materials" is my own work and has not been submitted previously by me for taking degree from Department of Electronics, Quaid-i-Azam University Or anywhere else in the country/world.

At any time if my statement is found to be incorrect even after my graduation, the university has the right to withdraw my PhD degree.

Maimoona Naheed

Date: _____



QUAID-I-AZAM UNIVERSITY
Department of Electronics

Plagiarism Undertaking

I solemnly declare that research work presented in the thesis titled

"Surface Electromagnetic Waves Guided by Interfaces with Isotropic Chiral and Uniaxially Chiral Materials"

is solely my research work with no significant contribution from any other person. Small contribution/help wherever taken has been duly acknowledged and that complete thesis has been written by me.

I understand the zero tolerance policy of the HEC and Quaid-i-Azam University towards plagiarism. Therefore, I as an Author of the above titled thesis, declare that no portion of my thesis has been plagiarized and any material used as reference is properly referred/cited.

I undertake that if I am found guilty of any formal plagiarism in the above titled thesis even after award of PhD degree, the University reserves the rights to withdraw/revoke my PhD degree and that HEC and the University has the right to publish my name on the HEC/University Website on which names of students are placed who submitted plagiarized thesis.

Student/Author Signature: M. Naheed.

Name: Maimoona Naheed

SURFACE ELECTROMAGNETIC WAVES GUIDED BY
INTERFACES WITH ISOTROPIC CHIRAL AND
UNIAXIALLY CHIRAL MATERIALS



By
Maimoona Naheed

SUBMITTED IN PARTIAL FULFILLMENT OF THE
REQUIREMENTS FOR THE DEGREE OF
DOCTOR OF PHILOSOPHY
AT
QUAID-I-AZAM UNIVERSITY
ISLAMABAD, PAKISTAN
AUGUST 2021

© Copyright by Maimoona Naheed, 2021

QUAID-I-AZAM UNIVERSITY
DEPARTMENT OF
ELECTRONICS

The undersigned hereby certify that they have read and recommend to the Faculty of Graduate Studies for acceptance a thesis entitled “**Surface electromagnetic waves guided by interfaces with isotropic chiral and uniaxially chiral materials**” by **Maimoona Naheed** in partial fulfillment of the requirements for the degree of **Doctor of Philosophy**.

Dated: August 2021

Supervisor:

Co-Supervisor:

Chairman:

QUAID-I-AZAM UNIVERSITY

Date: **August 2021**

Author: **Maimoona Naheed**

Title: **Surface electromagnetic waves guided by interfaces
with isotropic chiral and uniaxially chiral materials**

Department: **Electronics**

Degree: **Ph.D.**

Year: **2021**

Permission is herewith granted to Quaid-I-Azam University to circulate and to have copied for non-commercial purposes, at its discretion, the above title upon the request of individuals or institutions.

Signature of Author

THE AUTHOR RESERVES OTHER PUBLICATION RIGHTS, AND NEITHER THE THESIS NOR EXTENSIVE EXTRACTS FROM IT MAY BE PRINTED OR OTHERWISE REPRODUCED WITHOUT THE AUTHOR'S WRITTEN PERMISSION.

THE AUTHOR ATTESTS THAT PERMISSION HAS BEEN OBTAINED FOR THE USE OF ANY COPYRIGHTED MATERIAL APPEARING IN THIS THESIS (OTHER THAN BRIEF EXCERPTS REQUIRING ONLY PROPER ACKNOWLEDGEMENT IN SCHOLARLY WRITING) AND THAT ALL SUCH USE IS CLEARLY ACKNOWLEDGED.

*To my parents, siblings, and family especially my beloved
daughter “Momina Zahra”*

Table of Contents

Table of Contents	vi
List of Figures	ix
List of Acronyms	xviii
List of Symbols	xix
Acknowledgements	xxiii
Abstract	xxv
List of Publications	xxvii
1 Introduction	1
1.1 Surface Plasmon-Polariton (SPP) Waves	4
1.2 Isotropic Chiral Materials	6
1.3 Columnar Thin Films	7
1.4 Uniaxially Chiral, Bianisotropic Materials	10
1.5 Canonical Problem	12
1.6 Prism-Coupled Configurations	14
1.6.1 TKR configuration	14
1.6.2 Turbadar–Otto configuration	15
1.7 Objectives of the Thesis	16
1.8 Overview of the Thesis	17
References	19
2 Two Isotropic Chiral Materials	34
2.1 Introduction	34

2.2	Canonical Problem	36
2.3	Numerical Studies	40
2.4	Conclusions	48
References		50
3	Metal and Isotropic Chiral Medium	54
3.1	Introduction	54
3.2	Theory of Prism-Coupled Configurations	56
3.3	Theory of Canonical Problem	64
3.4	Results and Discussion	67
3.4.1	Canonical problem	67
3.4.2	Conditions for the excitation of the SPP waves	69
3.4.3	TKR prism coupling	69
3.4.4	Turbadar–Otto prism coupling	74
3.5	Conclusions	78
References		79
4	Metal and Non-Magnetic Uniaxially Chiral, Bianisotropic Material	83
4.1	Introduction	84
4.2	Theory: Prism-Coupled Configurations	84
4.3	Numerical Results and Discussion	86
4.3.1	Canonical boundary-value problem	87
4.3.2	TKR prism coupling	87
4.3.3	Turbadar–Otto prism coupling	91
4.4	Conclusions	95
References		96
5	Metal and Obliquely Mounted, Uniaxially Chiral, Bianisotropic Material	98
5.1	Introduction	99
5.2	Canonical Problem	99
5.2.1	Formulation of the dispersion equation	101
5.2.2	Solution of the dispersion equation	104
5.3	Prism-Coupled Configurations	107
5.3.1	TKR configuration	108
5.3.2	Turbadar–Otto configuration	110

5.4	Conclusions	113
References		114
6	Conclusions and Future Work	118
6.1	Conclusions	118
6.2	Future Work	121
Appendix A Metal and Columnar Thin Film		122
A.1	Introduction	122
A.2	Results and Discussion	124
A.2.1	Problem description	124
A.2.2	Turbadar–Otto configuration	130
A.2.3	Numerical results for Turbadar–Otto configuration	131
A.2.4	TKR configuration	133
A.2.5	Comparison with TKR configuration	134
A.2.6	Sensing in the Turbadar–Otto configuration	135
A.3	Conclusions	137
Appendix References		138

List of Figures

1.1	The typical profile of magnitude of the electric field of a surface wave is plotted versus z axis that is perpendicular to the interface. Both partnering mediums are considered homogeneous and isotropic for this.	4
1.2	The schematic of a CTF is shown.	9
1.3	The schematic of the uniaxial chiral bianisotropic material when the circular nano helixes are assembled perpendicular to the substrate. .	11
1.4	The schematic of the uniaxial chiral bianisotropic material when the circular nano helixes are assembled at some angle χ to the substrate.	12
1.5	The SPP-wave propagation along the interface of an isotropic chiral half-space and a metallic half-space is shown schematically in the canonical problem.	13
1.6	The schematic of the Turbadar–Kretschmann–Raether (TKR) configuration.	15
1.7	The schematic of the Turbadar–Otto configuration.	16
2.1	The interface of two isotropic chiral materials \mathcal{A} and \mathcal{B} is shown schematically as a canonical problem. Since material \mathcal{A} occupies half space $z > 0$	36

2.2	Bruggeman estimates of the $\text{Re}\{\cdot\}$ and $\text{Im}\{\cdot\}$ parts of the relative constitutive parameters $\varepsilon^{\mathcal{B}}$, $\mu^{\mathcal{B}}$, and $\xi^{\mathcal{B}}$ plotted against volume fraction $f_a^{\mathcal{B}}$ for $\varepsilon_a^{\mathcal{B}} = 2 - 0.02di$. Key: $d = 1.0$ (thick dashed red curve), 0.5 (thick broken dashed blue curve), 0.2 (thick solid green curve), -0.2 (thin dashed red curve), -0.5 (thin broken dashed blue curve), and -1.0 (thin solid green curve).	43
2.3	$\text{Re}\{\cdot\}$ and $\text{Im}\{\cdot\}$ parts of the relative wavenumber q/k_0 plotted versus volume fraction $f_a^{\mathcal{B}}$ for $\varepsilon_a^{\mathcal{B}} = 2 - 0.02di$. Key: $d = 1.0$ (thick dashed red curve), 0.5 (thick broken dashed blue curve), 0.2 (thick solid green curve), -0.2 (thin dashed red curve), -0.5 (thin broken dashed blue curve), and -1.0 (thin solid green curve).	44
2.4	Magnitudes of $\underline{E}_{\mathcal{A},\mathcal{B}}(z\hat{u}_z) \cdot \underline{n}$, and $\underline{H}_{\mathcal{A},\mathcal{B}}(z\hat{u}_z) \cdot \underline{n}$, along with $\underline{P}_{\mathcal{A},\mathcal{B}}(z\hat{u}_z) \cdot \underline{n}$, plotted against z/λ_0 , when $\varepsilon_a^{\mathcal{B}} = 2 - 0.02di$, $f_a^{\mathcal{B}} = 0.85$, $d = 0.5$, and $C_{\mathcal{A}1} = 1 \text{ Vm}^{-1}$. Key: $\underline{n} = \hat{u}_x$ (solid red curves); $\underline{n} = \hat{u}_y$ (dashed blue curves); $\underline{n} = \hat{u}_z$ (broken dashed green curves).	44
2.5	Bruggeman estimates of the $\text{Re}\{\cdot\}$ and $\text{Im}\{\cdot\}$ parts of the relative constitutive parameters $\varepsilon^{\mathcal{B}}$, $\mu^{\mathcal{B}}$, and $\xi^{\mathcal{B}}$ plotted against volume fraction $f_a^{\mathcal{B}}$ for $\varepsilon_a^{\mathcal{B}} = -2 + 0.02di$. Key: $d = 50$ (solid red curve), 100 (dashed blue curve), and 200 (broken dashed green curve).	45
2.6	$\text{Re}\{\cdot\}$ and $\text{Im}\{\cdot\}$ parts of the relative wavenumber q/k_0 plotted versus volume fraction $f_a^{\mathcal{B}}$ for $\varepsilon_a^{\mathcal{B}} = -2 + 0.02di$. Key: $d = 50$ (solid red curve), 100 (dashed blue curve), and 200 (broken dashed green curve).	46
2.7	Magnitudes of $\underline{E}_{\mathcal{A},\mathcal{B}}(z\hat{u}_z) \cdot \underline{n}$, and $\underline{H}_{\mathcal{A},\mathcal{B}}(z\hat{u}_z) \cdot \underline{n}$, along with $\underline{P}_{\mathcal{A},\mathcal{B}}(z\hat{u}_z) \cdot \underline{n}$, plotted against z/λ_0 , when $\varepsilon_a^{\mathcal{B}} = -2 + 0.02di$, $f_a^{\mathcal{B}} = 0.85$, $d = 100$, and $C_{\mathcal{A}1} = 1 \text{ Vm}^{-1}$. Key: $\underline{n} = \hat{u}_x$ (solid red curves); $\underline{n} = \hat{u}_y$ (dashed blue curves); $\underline{n} = \hat{u}_z$ (broken dashed green curves).	46
3.1	A general schematic for the SPP-waves excitation at the interface of two different homogeneous isotropic mediums is shown representing the prism coupling.	57

3.2	A general schematic for the SPP-waves propagation along the interface of two different isotropic homogeneous half-spaces is shown.	64
3.3	The $\text{Re}\{\cdot\}$ and $\text{Im}\{\cdot\}$ parts of the relative wavenumber of the SPP wave versus real part of $\xi^{\mathcal{B}}$ in the canonical problem. The imaginary part of $\xi^{\mathcal{B}}$ was fixed at 0.0001. Furthermore, $\varepsilon^{\mathcal{B}} = 1.77 + 0.01i$, $\mu^{\mathcal{A}} = \mu^{\mathcal{B}} = 1$, $\xi^{\mathcal{A}} = 0$, $\varepsilon^{\mathcal{A}} = \varepsilon_{met}^{\mathcal{A}} = -56 + 21i$, and $\lambda_0 = 633$ nm.	68
3.4	The absorptance A_p plotted versus the incidence angle θ for p -polarized incident electromagnetic wave in the TKR configuration when $n_p = 2.6$, $n_t = 1$, $L_{\mathcal{A}} = 15$ nm, $L_{\mathcal{B}} = 500$ nm, $\varepsilon^{\mathcal{A}} = \varepsilon_{met}^{\mathcal{A}} = -56 + 21i$, $\varepsilon^{\mathcal{B}} = 1.77 + 0.01i$, $\xi^{\mathcal{A}} = 0$, and $\text{Im}(\xi^{\mathcal{B}}) = 0.0001$. The downward arrow pinpoints the absorptance peak that signifies the SPP-wave excitation.	71
3.5	Same as Fig. 3.4 except that the absorptance is computed for the s -polarized incident planewave.	72
3.6	Same as Fig. 3.4 except that the absorptance is computed for different thicknesses of the chiral material and for fixed $\xi^{\mathcal{B}} = 0.03 + 0.0001i$ and $L_{\mathcal{A}} = 15$	72
3.7	The total reflectance R_p plotted versus the incidence angle θ for p -polarized incident electromagnetic wave in the TKR configuration when $n_p = 2.6$, $n_t = 1$, $L_{\mathcal{A}} = 15$ nm, $\varepsilon^{\mathcal{A}} = \varepsilon_{met}^{\mathcal{A}} = -56 + 21i$, $\varepsilon^{\mathcal{B}} = 1.77 + 0.01i$, $\xi^{\mathcal{A}} = 0$, and $\xi^{\mathcal{B}} = 0.03 + 0.0001i$ for different values of $L_{\mathcal{B}}$. The downward arrow pinpoints the reflectance dip that signifies the SPP-wave excitation.	73
3.8	Magnitudes of the three Cartesian components of power density $\underline{P}(0, 0, z)$ versus z in the TKR configuration when p -polarized electromagnetic wave is incident at the metal/chiral-medium interface for (a) $\xi^{\mathcal{B}} = 0.00 + 0.0001i$ and (b) $\xi^{\mathcal{B}} = 0.02 + 0.0001i$ when the incidence angle $\theta = 31.5^\circ$. The other parameters are the same as given in Fig. 3.4. The x -, y -, and z -components are denoted, respectively, by a solid red line, a dashed blue line, and a chain-dashed black line.	73

- 3.9 The absorptance A_p plotted versus the incidence angle θ for p -polarized electromagnetic wave in the Turbadar–Otto configuration when $n_p = 2.6$, $n_t = 1$, $L_{\mathcal{A}} = 500$ nm, $L_{\mathcal{B}} = 30$ nm, $\varepsilon^{\mathcal{A}} = 1.77 + 0.01i$, $\varepsilon^{\mathcal{B}} = \varepsilon_{met}^{\mathcal{B}} = -56 + 21i$, $\text{Im}(\xi^{\mathcal{A}}) = 0.0001$, and $\xi^{\mathcal{B}} = 0$. The downward arrow pinpoints the absorptance peak that signifies the SPP-wave excitation. 75
- 3.10 Same as Fig. 3.9 except that the absorptance is computed for different values of the thickness of the chiral medium for fixed $\xi^{\mathcal{A}} = 0.03 + 0.0001i$ and $L_{\mathcal{B}} = 30$ nm. The downward arrow pinpoints the absorptance peak that signifies the SPP-wave excitation. 75
- 3.11 The total reflectance R_p plotted versus the incidence angle θ for p -polarized electromagnetic wave in the Turbadar–Otto configuration when $n_p = 2.6$, $n_t = 1$, $L_{\mathcal{B}} = 30$ nm, $\varepsilon^{\mathcal{A}} = 1.77 + 0.01i$, $\varepsilon^{\mathcal{B}} = \varepsilon_{met}^{\mathcal{B}} = -56 + 21i$, $\text{Im}(\xi^{\mathcal{A}}) = 0.0001$, and $\xi^{\mathcal{B}} = 0$. The downward arrow pinpoints the reflectance dip that signifies the SPP-wave excitation. . . . 76
- 3.12 Magnitudes of the three Cartesian components of power density $\underline{P}(0, 0, z)$ versus z in the Turbadar–Otto configuration when p -polarized electromagnetic wave is incident at the chiral-medium/metal interface for (a) $\xi^{\mathcal{A}} = 0.00 + 0.0001i$ and (b) $\xi^{\mathcal{A}} = 0.02 + 0.0001i$ when the incidence angle $\theta = 31.1^\circ$. The other parameters are the same as given in Fig. 3.9. The x -, y -, and z -components are denoted, respectively, by a solid red line, a dashed blue line, and a chain-dashed black line. 76
- 3.13 Same as Fig. 3.9 except that the absorptance is computed for the s -polarized incident planewave. 77

3.14	Magnitudes of the three Cartesian components of power density $\underline{P}(0, 0, z)$ versus z in the Turbadar–Otto configuration when s -polarized light is incident at the chiral-medium/metal interface for (a) $\xi^{\mathcal{A}} = 0.00 + 0.0001i$ and (b) $\xi^{\mathcal{A}} = 0.02 + 0.0001i$ when the incidence angle $\theta = 27^\circ$. The other parameters are the same as given in Fig. 3.9. The x -, y -, and z -components are denoted, respectively, by a solid red line, a dashed blue line, and a chain-dashed black line.	77
4.1	A general schematic for the SPP-waves excitation at the interface of two different homogeneous materials is shown in the prism coupling. .	85
4.2	The (a) $\text{Re}\{\cdot\}$ and (b) $\text{Im}\{\cdot\}$ parts of the relative wavenumber q/k_0 plotted versus the real part of the relative chirality parameter $(\gamma^{\mathcal{B}}c) = \gamma^{\mathcal{B}}/\sqrt{\varepsilon_0\mu_0}$. The imaginary part of the parameter was fixed at $\text{Im}(\gamma^{\mathcal{B}}c) = 0.0001$	87
4.3	The angle of incidence of the SPP-wave excitation plotted versus the real part of the relative chirality parameter $(\gamma^{\mathcal{B}}c) = \gamma^{\mathcal{B}}/\sqrt{\varepsilon_0\mu_0}$ predicted by canonical problem.	89
4.4	Absorptances plotted versus the incidence angle θ and chirality parameter. The absorptances for the TKR configuration are given for (a) p -polarized incident planewave and (b) s -polarized incident planewave when $n_p = n_t = 1.73$, $L_{\mathcal{A}} = 15$ nm, $L_{\mathcal{B}} = 400$ nm, $\varepsilon^{\mathcal{A}} = -56 + 21i$, $\varepsilon_a^{\mathcal{B}} = 2$, $\varepsilon_b^{\mathcal{B}} = 3$, $\gamma^{\mathcal{A}} = 0$, and $\text{Im}(\gamma^{\mathcal{B}}c) = 0.0001$	90
4.5	Magnitudes of the three Cartesian components of power density in the TKR configuration when (a) $\theta = 58.7^\circ$ and (b) $\theta = 58.9^\circ$. The other parameters are $n_p = n_t = 1.73$, $L_{\mathcal{A}} = 15$ nm, $L_{\mathcal{B}} = 400$ nm, $\varepsilon^{\mathcal{A}} = -56 + 21i$, $\varepsilon_a^{\mathcal{B}} = 2$, $\varepsilon_b^{\mathcal{B}} = 3$, $\gamma^{\mathcal{A}} = 0$, and $\text{Im}(\gamma^{\mathcal{B}}c) = 0.0001$ for p -polarized incidence. The P_x , P_y , and P_z components are shown by a solid red line, a dashed blue line, and a chain-dashed black line, respectively.	91

4.6	Absorptances plotted versus the incidence angle θ and chirality parameter in the Turbadar–Otto configuration for (a) p -polarized incident planewave and (b) s -polarized incident planewave when $n_p = n_t = 1.73$, $L_{\mathcal{A}} = 400$ nm, $L_{\mathcal{B}} = 30$ nm, $\varepsilon_a^{\mathcal{A}} = 2$, $\varepsilon_b^{\mathcal{A}} = 3$, $\varepsilon^{\mathcal{B}} = -56 + 21i$, $\text{Im}(\gamma^{\mathcal{A}c}) = 0.0001$, and $\gamma^{\mathcal{B}} = 0$	93
4.7	Magnitudes of the three Cartesian components of power density in the Turbadar–Otto configuration when (a) $\theta = 56.4^\circ$, (b) $\theta = 55.6^\circ$, (c) $\theta = 39.8^\circ$, and (d) $\theta = 38.1^\circ$ for p -polarized incidence when $n_p = 1.73$, $n_t = 1$, $L_{\mathcal{A}} = 400$ nm, $L_{\mathcal{B}} = 30$ nm, $\varepsilon_a^{\mathcal{A}} = 2$, $\varepsilon_b^{\mathcal{A}} = 3$, $\varepsilon^{\mathcal{B}} = -56 + 21i$, $\text{Im}(\gamma^{\mathcal{A}c}) = 0.0001$, and $\gamma^{\mathcal{B}} = 0$. P_x , P_y , and P_z components are shown by a solid red line, a dashed blue line, and a chain-dashed black line, respectively.	94
4.8	Same as Fig. 4.7 except that the incident planewave is s -polarized and (a) $\theta = 54.8^\circ$ and (b) $\theta = 52.6^\circ$	95
5.1	The SPP-waves propagation along the interface of a plasmonic material and the uniaxially chiral, bianisotropic medium is shown schematically in the canonical problem.	100
5.2	The $\text{Re}\{\cdot\}$ and $\text{Im}\{\cdot\}$ parts of q/k_0 of the SPP waves plotted against the tilt angle χ when $\varepsilon_{met} = -56 + 21i$, $\varepsilon_a = 2.3 + 0.023i$, $\varepsilon_b = 3.7 + 0.037i$, $\mu_a = 0.8 + 0.008i$, and $\mu_b = 1 + 0.01i$ were chosen. . . .	106
5.3	Magnitudes of the three Cartesian components of power density of the SPP wave when $\chi = 75^\circ$, $\gamma = (0.3 + 0.003i)\sqrt{\varepsilon_0\mu_0}$, and $q/k_0 = 1.9364 + 0.03306i$. The data were calculated by setting $a_p = 1$ V/m. The other parameters are the same as given in Fig. 5.2. The P_x , P_y , and P_z components are shown by solid red, dashed blue, and chain-dashed black lines, respectively.	106
5.4	The schematic of the prism coupling for the SPP-waves excitation is shown.	108

- 5.5 Absorptances plotted against the incidence angle θ and tilt angle χ in the TKR configuration. The absorptances for the TKR configuration are given for (a) p -polarized incident electromagnetic wave and (b) s -polarized incident wave when $n_p = 2.6$, $n_t = 1$, $L_A = 15$ nm, $\varepsilon_{met}^A = -56 + 21i$, $L_B = 400$ nm, $\varepsilon_a^B = 2.3 + 0.023i$, $\varepsilon_b^B = 3.7 + 0.037i$, $\mu_a^B = 0.8 + 0.008i$, $\mu_b^B = 1 + 0.01i$, and $\gamma^B = (0.3 + 0.003i)\sqrt{\varepsilon_0\mu_0}$ 109
- 5.6 Magnitudes of the three Cartesian components of the power density in the TKR configuration vs. z when $\theta = 48.7^\circ$ and $\chi = 75^\circ$. The other parameters are $n_p = 2.6$, $n_t = 1$, $L_A = 15$ nm, $L_B = 400$ nm, $\varepsilon_{met}^A = -56 + 21i$, $\varepsilon_a^B = 2.3 + 0.023i$, $\varepsilon_b^B = 3.7 + 0.037i$, $\mu_a^B = 0.8 + 0.008i$, $\mu_b^B = 1 + 0.01i$, and $\gamma^B = (0.3 + 0.003i)\sqrt{\varepsilon_0\mu_0}$ for p -polarized incidence. The components P_x , P_y , and P_z are shown by solid red, dashed blue, and chain-dashed black lines, respectively. 110
- 5.7 Absorptances plotted against the incidence angle θ and tilt angle χ in the Turbadar–Otto configuration for (a) p -polarized incident electromagnetic wave and (b) s -polarized incidence when $n_p = 2.6$, $n_t = 1$, $L_A = 400$ nm, $L_B = 30$ nm, $\varepsilon_a^A = 2.3 + 0.023i$, $\varepsilon_b^A = 3.7 + 0.037i$, $\mu_a^A = 0.8 + 0.008i$, $\mu_b^A = 1 + 0.01i$, $\gamma^A = (0.3 + 0.003i)\sqrt{\varepsilon_0\mu_0}$, and $\varepsilon_{met}^B = -56 + 21i$ 111
- 5.8 The components of power density in the Turbadar–Otto configuration when $\theta = 47.8^\circ$ and $\chi = 75^\circ$ for p -polarized incidence when $n_p = 2.6$, $n_t = 1$, $L_A = 400$ nm, $L_B = 30$ nm, $\varepsilon_a^A = 2.3 + 0.023i$, $\varepsilon_b^A = 3.7 + 0.037i$ and $\mu_a^A = 0.8 + 0.008i$, $\mu_b^A = 1 + 0.01i$, $\gamma^A = (0.3 + 0.003i)\sqrt{\varepsilon_0\mu_0}$, and $\varepsilon_{met}^B = -56 + 21i$. The components P_x , P_y , and P_z are shown by solid red, dashed blue, and chain-dashed black lines, respectively. 112
- 5.9 Same as Fig. 5.8 except that the planewave is s -polarized when $\theta = 45.1^\circ$. 112
- A.1 The schematic of the TKR configuration is shown. A linearly polarized electromagnetic wave is incident at the metal-CTF bilayer. The CTF is infiltrated by a fluid of which the refractive index is to be sensed. . 124

A.2	The schematic of the Turbadar–Otto configuration is shown. A linearly polarized electromagnetic wave is incident at the CTF-metal bilayer from the CTF side.	125
A.3	The absorptances plotted against the incidence angles θ for various thicknesses of the CTF when $\psi = 20$ deg, $\chi_v = 30$ deg, $\lambda_0 = 633$ nm, $L_{met} = 30$ nm, $\varepsilon_m = -56 + 21i$, and $n_p = 2.6$. The CTF was chosen to be made of titanium oxide and uninfiltrated.	132
A.4	The magnitudes of the three components of power density $\underline{P}(0, 0, z)$ vs. z in the Turbadar–Otto configuration when p -polarized planewave is incident on the CTF-metal interface at $\theta = 53.2^\circ$, and $L_{ctf} = 200$ nm. The other parameters are the same as given in Fig. A.3. The components parallel to \hat{u}_1 , \hat{u}_2 , and \hat{u}_z , are shown by a solid red line, a dashed blue line, and a chain-dashed black line, respectively.	133
A.5	Same as Fig. A.3 except that the absorptances are computed in TKR configuration for $L_{met} = 15$ nm.	135
A.6	Same as Fig. A.3 except that the CTF is now infiltrated with a fluid of refractive index $n_\ell = \{1, 1.1, 1.2, 1.3, 1.4, 1.5\}$, and $L_{ctf} = 200$ nm for the p -polarized incidence.	137

List of Acronyms

ATR	attenuated total reflectance
CTFs	columnar thin films
STF	sculptured thin film
CSTF	chiral sculptured thin film
deg	degrees
DNA	deoxyribonucleic acid
e.g.	for example
FWHM	full-width at half-maximum
HCMs	homogenized composite materials
i.e.	that is
Im	imaginary part
MODE	matrix ordinary differential equation
PVD	physical vapor deposition
Re	real part
SPP	surface plasmon-polariton
SNTF	sculptured nematic thin film
TKR	Turbadar–Kretschmann–Raether

List of Symbols

a_s, a_p	scalar amplitudes of s - and p -polarized electromagnetic waves
A_s, A_p	absorptances for s - and p -polarized incidence
α_{met}	wavenumber of the SPP wave in the metal normal to the direction of propagation
α_n	n th eigenvalue corresponding to n th eigenvector $[t]^{(n)}$
\underline{B}	magnetic flux density
$C_{1,2}$	unknown scalar coefficients
c	phase speed in the free space
\underline{D}	electric flux density
$[\underline{\underline{D}}]$	2×2 depolarization matrix
$\Delta\theta$	the full-width at half-maximum (FWHM)
$\Delta\theta_{peak}$	a small shift in the angular location of the tip representing the excitation of the SPP waves
\underline{E}	electric field phasor
$\exp(\cdot)$	exponential part containing the propagating and decaying components of a planewave
ε_0	permittivity of free space
ε	relative permittivity scalar
$\underline{\mathcal{E}}$ or \underline{e}	auxiliary electric field phasor
$e_z(z)$	z -component of the auxiliary electric field phasor
$e_{zm}(z)$	z -component of the auxiliary electric field phasor in the metal
$\varepsilon_a, \varepsilon_b, \varepsilon_c$	principle relative permittivity scalars

$\underline{\underline{\varepsilon}}$	permittivity dyadic
$\underline{\underline{\varepsilon}}_{ctf}$	permittivity dyadic of the CTF
$\sqrt{\varepsilon_a}, \sqrt{\varepsilon_b}$	the refractive indices parallel and perpendicular to the optic axis, respectively
$\varepsilon_m, \varepsilon_{met}$	relative permittivity of a metal
ε_d	composite relative permittivity scalar
$ \underline{E} $	amplitude of electric field phasor
ξ, γ	relative chirality pseudoscalar
$\underline{\underline{\xi}}$	dyadic modeling magnetoelectric properties
η_0	impedance of free space
f_a	the volume fraction of the achiral part of the material
f_b	the volume fraction of the chiral part of the material
$[f]$	x - and y -constituents of \underline{e} and \underline{h} represented by a column vector
\underline{H} or \underline{h}	auxiliary magnetic field phasor
$h_z(z)$	z -component of the auxiliary magnetic field phasor
$h_{zm}(z)$	z -component of the auxiliary magnetic field phasor in the metal
\underline{H}	magnetic field phasor
$[\underline{I}]$	2×2 identity matrix
$\underline{\underline{I}}$	identity dyadic
k_0	wavenumber of free space
\underline{k}	wave vector of electromagnetic planewave
\underline{k}_{met}	wave vector of electromagnetic planewave in the metal
$[\underline{\underline{K}}_a], [\underline{\underline{K}}_b], [\underline{\underline{K}}]$	2×2 matrices
$[\underline{\underline{K}}_{inc}]$	4×4 incidence matrix containing coefficients of the incident and reflected electric and magnetic field phasors
$[\underline{\underline{K}}_{tr}]$	4×4 transmission matrix containing coefficients of transmitted electric and magnetic field phasors
κ_R	relative wavenumber for right circularly-polarized light
κ_L	relative wavenumber for left circularly-polarized light

κ	transverse wavenumber
$L_{\mathcal{A}}$	thickness of material \mathcal{A} in the prism-coupled problem
$L_{\mathcal{B}}$	thickness of material \mathcal{B} in the prism-coupled problem
$L_{\Sigma} = L_{\mathcal{A}} + L_{\mathcal{B}}$	combined thickness of material \mathcal{A} and material \mathcal{B}
L_{ctf}	thickness of the CTF
L_{met}	thickness of the metal slab
λ_0	wavelength of free space
$\underline{\underline{M}}$	4×4 coefficient matrix
n_p	the refractive index of prism
n_t	the refractive index of transmission half space
n_{ℓ}	the refractive index of the liquid infiltrating the vacant spaces of the CTF
\underline{P}	power density (time-averaged Poynting vector)
$P_{x,y,z}$	x -, y - and z -components of \underline{P}
$\underline{\underline{P}}$	coefficient matrix of MODE
$\underline{\underline{P}}_{met}$	$\underline{\underline{P}}$ matrix for metal
$\underline{\underline{P}}_{ch}$	$\underline{\underline{P}}$ matrix for isotropic chiral medium
$\underline{\underline{P}}_{\mathcal{A}}$	$\underline{\underline{P}}$ matrix for material \mathcal{A}
$\underline{\underline{P}}_{\mathcal{B}}$	$\underline{\underline{P}}$ matrix for material \mathcal{B}
q	wavenumber of a surface wave in the canonical problem
q/k_0	relative wavenumber of a surface wave in the canonical problem along the direction of propagation
r_s, r_p	reflection coefficients of s - and p -polarized waves
R_p	total reflectance for p -polarized incidence
ρ	sensitivity
$\underline{\underline{S}}_y$	rotation dyadic in the xz plane around the y axis
ψ	angle between the morphologically significant plane of the CTF and the incidence plane/direction of propagation of a surface wave
t_s, t_p	transmission coefficients of s - and p -polarized waves

$\hat{\underline{u}}_x, \hat{\underline{u}}_y, \hat{\underline{u}}_z$	unit vectors along x -, y -, and z -axis
μ_0	permeability of free space
μ	relative permeability scalar
μ_a, μ_b	relative permeability scalars
$\underline{\underline{\mu}}$	permeability dyadic
θ, θ_{inc}	incidence angle with the z axis
θ_t	transmission angle
θ_{peak}	incidence angle where the absorptance peak in the absorptance spectrum indicates the SPP-wave excitation
ϕ	incidence angle with the x axis in the xy plane
ω	angular frequency
χ_v	the angle of projection of physical vapors with the substrate
χ	the tilt of columns in a CTF
$\underline{\underline{Y}}$	4×4 coefficient matrix

Acknowledgements

First and foremost, I am thankful to Almighty Allah for bestowing me with strength and determination through every thick and thin in the course of completing this journey. Secondly, I would like to take this opportunity to thank my dissertation supervisor, Dr. Muhammad Faryad, who has been instrumental in the successful completion of this work. Undoubtedly, it would have been impossible to complete this work without his constant support and guidance. He always remained approachable throughout this period whenever I got stuck in my journey through the Ph.D. I am extremely indebted to him as he gave superb direction, guideline and suggestions for my work. He also unconditionally supported and encouraged me through hard times of my life and also played a pivotal role as a mentor to my personal and professional developments. His professional dedication, integrity and commitment will surely remain inspirational throughout my professional career in future.

I am greatly indebted to Dr. Tom G. Mackay for providing me an opportunity for doing research under his supervision during a research visit. I am thankful to him for polishing my research abilities with his tremendous support and guidance in pursuit of my research. He boosted my abilities through his marvelous direction, mentorship and showed me extreme kindness to achieve my research goals. He provided me an ideal research environment that helped me towards my research destination.

I am also grateful to Dr. Qaisar Abbas Naqvi for his mentorship, support, encouragement and facilitation in every possible way for providing me the best research environment to carry out my research with ease. Thanks are also due to the proficient faculty of Department of Electronics, especially, Dr. Azhar Abbas Rizvi, Dr. Hasan

Mahmood, Dr. M. Aqeel Ashraf, Dr. Musarat Abbas, Dr. Aqeel Abbas, Dr. M. Farhan Saif, Dr. M. Zeshan Akbar, Dr. M. Arshad Fiaz, and Dr. Muhammad Zia, for contributing in my educational excellence in their respective spheres.

My words can not express my feelings of love for my family. My beloved parents deserve my deepest admiration as they inculcated believe in me with their extreme selfless support, devotion and prayers which made this intimidating task to become a reality. Special thanks to my siblings M. Irfan, M. Usman, M. Nauman and M. Suleman who had been valuing my efforts and pacified me in my turbulent times.

Finally, the funding from Higher Education Commission (HEC) of Pakistan is gratefully acknowledged for a six-month research visit to The University of Edinburgh.

Maimoona Naheed

June, 2021

Abstract

The electromagnetic waves that propagate along the interface of two dissimilar materials are called surface waves. The surface plasmon-polariton (SPP) waves are the surface waves that are guided by an interface of the partnering plasmonic material. The surface waves propagate parallel to the interface and decay away from the interface. The surface waves also decay along the direction of propagation if one or both of the partnering materials are lossy. The main purpose of this thesis is to theoretically investigate the propagation and excitation of the SPP waves with isotropic chiral materials and uniaxially bianisotropic chiral materials. Firstly, the characteristics of the SPP waves with these materials are reported by investigations of the canonical boundary-value problems where both partnering materials are taken to fill up the half-spaces. Afterwards, the excitation of these SPP waves is shown with both types of prism-coupled configurations, i.e., the Turbador—Kretschmann—Raether (TKR) configuration and the Turbador—Otto configuration. The effects of the complex-valued chirality parameter on the SPP-waves excitation are also investigated.

Three basic problems are solved numerically in this thesis. The first deals with finding the characteristics of surface waves propagating along the interface of two isotropic chiral materials. The second problem deals with the interface of isotropic chiral material and a plasmonic material. After developing an understanding of the isotropic chiral medium, I moved on to investigate the SPP-waves excitation with the interface of uniaxially chiral bianisotropic material and a plasmonic material.

The SPP waves propagating along the interface of isotropic chiral material and a plasmonic material were found to exist only when the chirality was smaller than a

threshold value. These waves could be excited using both prism-coupled configurations, though the Turbadar—Otto configuration was found better than the TKR in delineating the excitation of the SPP waves. For the uniaxially chiral, bianisotropic materials, similar phenomenon was observed where the SPP waves could exist only when the chirality pseudoscalar was less than a threshold value. Though, this threshold value in the bianisotropic material can be tuned by changing other parameters of this material. The SPP waves studied in this thesis can be used for designing optical sensors to sense chirality of the materials. Furthermore, the existence of threshold value can be used to design plasmonic switches. Also, the finding of hybrid polarized SPP waves with chiral materials can be useful for optical circuits.

List of Publications

1. M. Naheed, M. Faryad, and T. G. Mackay, “Electromagnetic surface waves guided by the planar interface of isotropic chiral materials,” *J. Opt. Soc. Am. B* **36**, F1–F8 (2019).
2. M. Naheed and M. Faryad, “Excitation of surface-plasmon-polariton waves in the Turbadar–Otto configuration guided by an interface with a columnar thin film,” *J. Nanophoton.* **13**, 036001 (2019).
3. M. Naheed and M. Faryad, “Excitation of surface plasmon-polariton waves in the prism-coupled configurations guided by reciprocal, uniaxially chiral, bianisotropic material,” *Opt. Commun.* **465**, 125611 (2020). Erratum: **465**, 126279 (2020).
4. M. Naheed and M. Faryad, “Surface plasmon-polariton waves guided by an interface of a metal and an obliquely mounted uniaxially chiral, bianisotropic material,” *J. Electromagn. Waves Appl.* **34**, 1756–1770 (2020).
5. M. Naheed and M. Faryad, “Excitation of surface plasmon-polariton waves at the interface of a metal and an isotropic chiral material in the prism-coupled configurations,” *Eur. Phys. J. Plus* **135**, 724 (2020).

Chapter 1

Introduction

The surface electromagnetic waves propagate along the interface of two dissimilar materials [1]. These waves date back to the start of the twentieth century when the concept of surface waves along the interface of the nondissipative dielectric material (air) and the dissipative sea water was investigated by Uller [2]. Afterward, Zenneck proposed that a surface electromagnetic wave might also propagate along the interface of air and ground in the radio frequency regime [3]. Sommerfeld [4] and Bouwkamp [5] investigated the surface waves proposed by Zenneck in detail. These surface waves have recently been dubbed as Uller–Zenneck waves [6, 7].

The energy profile of surface waves, as shown in Fig. 1.1, concentrates near the interface and decays away from that interface. This property of surface electromagnetic waves is exploited in optical sensing of chemical and bio-chemical species [8]. Since surface waves are responsive to the permittivity of partnering materials, a change in the permittivity of either material affects the wavenumber of the surface wave. This change in the wavenumber is measured to determine the change in the permittivity. This is the basic principle of optical sensing using surface waves.

The objective of the research conducted for this thesis is to theoretically investigate the excitation and propagation of surface electromagnetic waves. The most famous surface electromagnetic waves are surface plasmon-polariton (SPP) waves. The SPP waves are surface waves propagating along the interface of a plasmonic material and another material. The other material is usually a dielectric but not

always. A vast majority of research on the SPP waves concerns the interface of a dielectric material and a plasmonic material. However, this thesis concerns surface electromagnetic waves propagating along the interfaces of isotropic chiral and bianisotropic chiral materials. Chiral materials are composed of constituents with broken mirror-symmetry, like helices. The SPP waves are highly confined to the interface with their fields decay perpendicular to the direction of propagation [9–11]. The characteristics of these SPP waves like wavelength, degree of confinement to the interface, attenuation rate along the direction of propagation, and the angular range in the interface plane within which the SPP waves can exist, depend mostly upon the material chosen to partner with the plasmonic material [11]. This partnering material can be isotropic, anisotropic, or bianisotropic [12]. In addition to the choice of anisotropy, the partnering material can be either homogeneous or periodically nonhomogeneous parallel [13] or perpendicular [14, 15] to the interface. The periodic nonhomogeneity perpendicular to the interface engenders many SPP waves of distinct phase speeds, polarization states, and degrees of localization, all at the same frequency. [14–18]. The anisotropy of the dielectric material generally affects the angular range of existence of the SPP waves, their degrees of localization, and sensitivity to the permittivity dyadic in addition to the polarization states. The partnering anisotropic or bianisotropic materials may also give rise to the SPP waves that cannot have any definite linear polarization state. The hyperbolic anisotropy underpins extremely sensitive plasmonic sensors both with the homogeneous dielectric partners and the periodically nonhomogeneous partners [19]. The SPP waves [9, 20] find utilities for optical sensing [10], biosensing [21, 22], bio-chemical sensing [23], near-field optics [24, 25], spectroscopy [26], far-field optics [27], nanocrystals and hybrid nanostructures [28], and imaging [29].

The SPP waves are of p -polarization state and propagate with the same properties in the interface plane when excited using the isotropic and homogeneous dielectric materials partnered with a plasmonic material [9, 30, 31]. However, when the isotropic dielectric material is replaced with an anisotropic dielectric material [12, 32–34], the

SPP waves exhibit different properties in different directions. The SPP-waves propagation has been investigated with several bianisotropic dielectric materials including anisotropic [12], uniaxial [35, 36], biaxial [36], isotropic chiral [37], uniaxial chiral [38], chiral omega [38], magnetic gyrotropic media [39], uniaxially bianisotropic enantiomeric media [40], and uniaxial bianisotropic media [41, 42]. The complex materials offer rich possibilities to engineer the properties of the SPP waves for a wide variety of applications. The optical properties of these waves are exploited in circular dichroism [43], hybrid surface plasmon-polariton wave [44], etc. In this thesis, the surface electromagnetic waves are chiefly studied with homogeneous isotropic chiral and homogeneous uniaxially chiral bianisotropic materials. The research reported in this thesis was mainly motivated by the longing to be able to launch surface waves with chiral materials for expanding the range of the applications of surface waves, e.g., enhancing the applications of sensing, imaging, and plasmonic communications. Apart from the interfaces of different chiral materials, the surface waves chiefly considered are the SPP waves.

In this chapter, basic concepts required for the rest of the thesis are provided. This chapter is arranged as follows: A literature review and applications of the SPP waves are penned in detail in Sec. 1.1. The isotropic chiral materials are introduced in Sec. 1.2. The columnar thin films (CTFs) and uniaxial materials are introduced in Sec. 1.3 as a preliminary context for the next section. The uniaxially chiral, bianisotropic materials are introduced in detail in Sec. 1.4. The canonical boundary-value problem for finding the characteristics of the SPP waves propagating along the interface of two different homogeneous partnering materials is explained in Sec. 1.5. The introduction of practical setups is given in Sec. 1.6. The objectives of the thesis are highlighted in Sec. 1.7. Lastly, the overview of this thesis is provided in Sec. 1.8.

In this thesis, the time dependency is taken as $\exp(-i\omega t)$ implicitly, the permeability and permittivity of free space are designated as μ_0 and ε_0 , respectively. The wavenumber in free-space is represented by $k_0 = \omega\sqrt{\varepsilon_0\mu_0}$ with $\lambda_0 = 2\pi/k_0$ as the free-space wavelength and the angular frequency is given by ω , the phase speed in

the free-space is specified by $c = 1/\sqrt{\varepsilon_0\mu_0}$ and the free-space impedance is given by $\eta_0 = \sqrt{\frac{\mu_0}{\varepsilon_0}}$. The imaginary and real parts of the complex-valued quantities are represented by $\text{Im}\{\cdot\}$ and $\text{Re}\{\cdot\}$, respectively, and $i = \sqrt{-1}$. The triad of unit vectors $\{\underline{\hat{u}}_x, \underline{\hat{u}}_y, \underline{\hat{u}}_z\}$ show alignment with the Cartesian axes. The vectors are underlined once and unit vectors are additionally decorated with a hat. The matrices are doubly underlined and confined in square brackets. The dyadics are underlined twice.

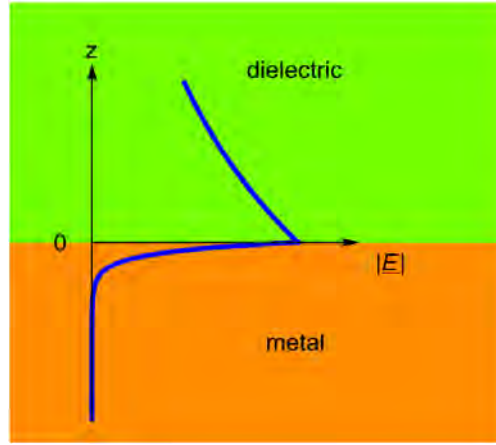


Figure 1.1: The typical profile of magnitude of the electric field of a surface wave is plotted versus z axis that is perpendicular to the interface. Both partnering mediums are considered homogeneous and isotropic for this.

1.1 Surface Plasmon-Polariton (SPP) Waves

Among the various types of surface electromagnetic waves, the SPP waves are the most investigated regarding their applicability and theoretical development [5, 45], however, rigorous work on the SPP waves [9, 46–48] started 60 years ago [49]. The SPP wave [8] is a surface electromagnetic wave that is propagated along the interface of a dielectric material and a plasmonic material [1]. The partnering dielectric material on the other side of the plasmonic material can be homogeneous, periodically non-homogeneous [50, 51], isotropic, or anisotropic [50, 52], such as a chiral sculptured thin

film (CSTF) [14, 52, 53] and a sculptured nematic thin film (SNTF) [14, 50, 54].

The SPP waves can be useful in a number of applications like sensing single molecules [55, 56], carrying various signals in one optical beam [57], intrinsic amplification of weak signals [58], remote measurement capability, and high sensitivity. The SPP waves can sense chemical and biochemical molecules in the optical regime [10, 59]. Using sensing techniques based on the SPP waves; the bioaffinity interactions with proteins, phage display libraries, DNA, carbohydrates, and peptides have been well studied [60].

The SPP waves are highly confined to the interface. The confinement to the interface supports its use in optical sensing because a significant change in the characteristics of the SPP wave results from a slight change in the dielectric properties of one of the two materials near the interface [51]. This change is usually exhibited as a shift in either the free-space wavelength or the angle of incidence of the incident electromagnetic wave exciting the surface wave in the prism coupling techniques [61]. Although, the dielectric material can be a porous material with a fluid containing the analyte to be sensed, infiltrating the material. Interestingly, the dynamic sensitivity of a prism/metal/porous material with infiltrating liquid/fluid setup measured experimentally has been found to significantly exceed the theoretical sensitivity of the prism/metal/fluid setup [50].

The SPP waves also find applications in imaging systems for highly efficient analysis of interactions between biomolecules, e.g., for proteomics, pathway elucidation, and drug discovery [62, 63]. Lithography can also be enhanced by using imaging techniques based on these SPP waves [9, 64]. The SPP waves also find applications in the field of communication by providing high-speed information exchange on computer chips [65]. Furthermore, ohmic losses for the SPP-wave-based transmission system [46] are small as compared to the wired-based transmission systems. So, the long-range communications can be enhanced by developing the communication systems based on the SPP waves [66]. Optical tweezers [67] and near-field optics [68] are a few more applications of plasmonics.

1.2 Isotropic Chiral Materials

A few decades ago, strong chirality was not available. But, now the chiral metamaterials with strong enough chirality [69, 70] for applications, particularly in the optical domain [71], are possible. Natural isotropic chiral materials/substances include glucose and aspartame.

In this thesis, the isotropic chiral materials are explored for surface-wave propagation due to their inherent magneto-electric coupling in Chaps. 2 and 3. The isotropic chiral material can be well explained as random distribution of helices or other chiral objects in a dielectric host [72].

The Tellegen constitutive relations in the frequency-domain of an isotropic chiral material [73] are given by the following equation

$$\left. \begin{aligned} \underline{D}(\underline{r}, \omega) &= \varepsilon_0 \varepsilon \underline{E}(\underline{r}, \omega) + i \sqrt{\varepsilon_0 \mu_0} \xi \underline{H}(\underline{r}, \omega) \\ \underline{B}(\underline{r}, \omega) &= -i \sqrt{\varepsilon_0 \mu_0} \xi \underline{E}(\underline{r}, \omega) + \mu_0 \mu \underline{H}(\underline{r}, \omega) \end{aligned} \right\}. \quad (1.2.1)$$

The relative permittivity scalar is represented by ε , the relative chirality pseudoscalar by ξ , and the relative permeability scalar by μ . Generally, these parameters are complex-valued and frequency dependent, per the causality principle represented by the Kramers–Kronig relations [74].

Because of the gyrotropic properties exhibited by isotropic chiral materials owing to their magneto-electric coupling, these materials are also known as optically active materials [75, 76]. Thus, the gyrotropic effects such as optical rotation, circular birefringence, and circular dichroism are manifestation of these chiral materials [77].

There is relatively little literature work available on the surface waves supported by chiral materials to date [78]. Pattanayak in 1981 dealt with finding of general structure of the electromagnetic fields in an optically active medium (chiral medium) occupying any arbitrary volume. The dispersion relation was obtained for surface waves propagating along the interface of a vacuum and a magnetoelectric half-space [75]. Another work presented by Nader Engheta in 1991 was on investigation of surface

waves in homogeneous sheets of chiral materials. The solution of the dispersion equation and the components of the electric field for guided surface waves were presented for a symmetric chiral slab waveguide and a grounded chiral slab waveguide. The effects of chirality were discussed and the potential applications of these chiral layered-structures in integrated optical devices, directional couplers and switches, microstrip antennas, and radar technology were addressed [79]. Fantino reported the work which presents the feasibility of surface-waves excitation at an interface of a chiral medium and achiral isotropic plasmonic material by exploiting the range of chirality parameter in which surface waves could be initiated. For this study, the dispersion relation of that interface was solved numerically [80]. A recent work combined a birefringent surface defect with a one-dimensional photonic crystal supporting chiral surface electromagnetic waves for improved circular dichroism. Thus, by exploiting the chiral properties of the probing electromagnetic field, the surface-enhanced spectroscopies in combination with the electromagnetic superchirality can be achieved. This has applications in microfluidic networks, lab-on-chip technologies and the analysis of the structures in proteins [43].

These materials can also be useful in the designing of directional couplers [76,81], switches, chirowaveguides [81–83], chirostrip antennas [84], integrated optical devices and advanced radar technology [85]. Hybrid modes [79,81] and hybrid SPP waves [44] have also been studied with these chiral metamaterials.

1.3 Columnar Thin Films

The basic theory on anisotropic nanostructured columnar thin films (CTFs) is presented here as a preliminary context for the next section on bianisotropic materials. These thin films are explored for SPP-wave propagation in both the prism-coupled configurations and the research is reported in the Appendix of this thesis. The CTFs are porous films of columnar morphology with all columns parallel to a straight line [86]. Using the physical vapor deposition (PVD) technique, these films are deposited by steering a vapor flux at a substrate at an oblique angle as depicted

in Fig. 1.2 [87].

The permittivity dyadic of the CTF is represented by

$$\underline{\underline{\varepsilon}}_{ctf} = \varepsilon_0 \underline{\underline{S}}_y \cdot (\varepsilon_a \underline{\hat{u}}_z \underline{\hat{u}}_z + \varepsilon_b \underline{\hat{u}}_x \underline{\hat{u}}_x + \varepsilon_c \underline{\hat{u}}_y \underline{\hat{u}}_y) \cdot \underline{\underline{S}}_y^{-1} \quad (1.3.1)$$

where the dyadic

$$\underline{\underline{S}}_y = \cos \chi (\underline{\hat{u}}_x \underline{\hat{u}}_x + \underline{\hat{u}}_z \underline{\hat{u}}_z) + \sin \chi (\underline{\hat{u}}_z \underline{\hat{u}}_x - \underline{\hat{u}}_x \underline{\hat{u}}_z) + \underline{\hat{u}}_y \underline{\hat{u}}_y \quad (1.3.2)$$

represents the rotation by an angle χ in the xz plane around the y axis, the ε_a , ε_b , and ε_c are known as principal relative permittivity scalars and the unit vectors in the Cartesian coordinate system are represented by $\underline{\hat{u}}_x$, $\underline{\hat{u}}_y$, and $\underline{\hat{u}}_z$. The principal relative permittivity scalars for the porous anisotropic CTF depends on whether the CTF is un-infiltrated or infiltrated by a liquid infiltrating the vacant spaces of the CTF.

Already amorphous silicon, amorphous germanium, oxides of aluminum, silicon, titanium, tantalum, tungsten, zirconium, bismuth, chromium, copper, iron, platinum, fluorides of calcium and magnesium, polymers of parylene, teflon, pyrolytic graphite, and silicon carbide have been experimented for the growth of thin films morphologies [87]. Firstly, the chiral morphology of STFs was reported and experimented by Young and Kowal [88, 89] in the mid-decade of the twentieth century. They deliberately rotated the substrate about the reference axis constantly during growth and created morphology of helically deposited thin films of calcium fluoride. The novel effect of optical activity was reported then. Afterwards, the novel effects of circular birefringence, circular dichroism, and circular Bragg phenomenon were also reported. These novel effects of chirality of the chiral nanostructures have potential applications in optical filters [90], laser mirrors [91, 92], bandwidth engineering [93–95], wave plates [96, 97], spectral hole filters [98, 99], optical fluid sensors [100–102], liquid crystals (LCs) displays [103], optical interconnects [104, 105], optical pulse-shapers [106, 107], biochips [108], biosensors [109], transverse architectures [110–114], and ultrasonic applications [115–120]. The scope of chiral nanostructured morphologies is not limited to these applications only, but their range of utilities can also be extended to the desired techno-scientific needs.

Uniaxial materials are the simplest anisotropic materials and a special case of a CTF with $\varepsilon_b = \varepsilon_c$. A uniaxial material has only one crystallographic axis. The projection of its relative permittivity dyadic on that axis is different from the projection of that dyadic in any direction normal to the axis. CTFs made of columns of circular cross-section are uniaxial materials because $\varepsilon_b = \varepsilon_c$. Also, many crystalline materials such as quartz and calcite are uniaxial. The permittivity dyadic of a uniaxial metamaterial is represented by

$$\underline{\underline{\varepsilon}} = \varepsilon_0 \left[\varepsilon_b (\hat{u}_x \hat{u}_x + \hat{u}_y \hat{u}_y) + \varepsilon_a \hat{u}_z \hat{u}_z \right], \quad (1.3.3)$$

where $\sqrt{\varepsilon_a}$ and $\sqrt{\varepsilon_b}$ are the refractive indices parallel and perpendicular to the optic axis, respectively.

Uniaxial materials show birefringence that is used to control light in a wide range of applications. For example, it is widely used in making optical components like beam splitters, optical interleavers, circulators, and optical isolators [121]. Uniaxial materials are also used as brightness enhancers in illumination systems [121]. The Raman scattering is also observed by phonon polariton phenomenon that takes place in uniaxial crystals [122, 123].

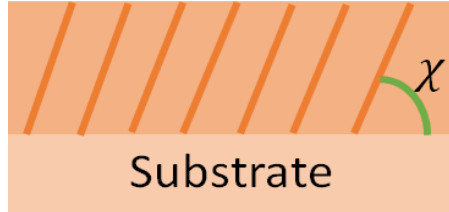


Figure 1.2: The schematic of a CTF is shown.

The SPP-waves excitation at the interface of a plasmonic material and a CTF has been studied for designing plasmonic optical sensors [124, 125]. The CTFs are the porous anisotropic films and have advantage over isotropic dielectric partnering material when it comes to optical sensing. The sensitivity can be enhanced significantly

by infiltrating the porous anisotropic partnering material with metallic particles [126] or by making the anisotropic partnering material as a hyperbolic medium [127].

1.4 Uniaxially Chiral, Bianisotropic Materials

The uniaxially chiral, bianisotropic materials are explored for SPP-wave propagation in Chaps. 4 and 5. The uniaxially chiral bianisotropic material [41, 42, 128] can be realized as an assembly of parallel circular nano helixes, as shown in Fig. 1.3, in the host dielectric medium where the period and thickness of these helixes should be smaller than one-tenth of the operating wavelength of the electromagnetic wave inside the material [41, 42, 129–131]. Such a material is a special case of linear bianisotropic material and can be easily fabricated using PVD techniques [87]. Uniaxial chiral material is the simplest of chiral bianisotropic material combining the periodicity and the anisotropy in a special fashion.

The Tellegen constitutive relations in the frequency-domain [11] of homogeneous, uniaxially chiral, bianisotropic material are given as

$$\left. \begin{aligned} \underline{D}(\underline{r}, \omega) &= \underline{\underline{\varepsilon}} \cdot \underline{E}(\underline{r}, \omega) + \underline{\underline{\xi}} \cdot \underline{H}(\underline{r}, \omega) \\ \underline{B}(\underline{r}, \omega) &= \underline{\underline{\mu}} \cdot \underline{H}(\underline{r}, \omega) - \underline{\underline{\xi}}^T \cdot \underline{E}(\underline{r}, \omega) \end{aligned} \right\}. \quad (1.4.1)$$

The permittivity dyadic of the uniaxially chiral bianisotropic medium [130, 131] is specified as

$$\underline{\underline{\varepsilon}} = \varepsilon_0 \underline{\underline{S}}_y \cdot [\varepsilon_a \hat{u}_z \hat{u}_z + \varepsilon_b \hat{u}_x \hat{u}_x + \varepsilon_b \hat{u}_y \hat{u}_y] \cdot \underline{\underline{S}}_y^{-1}, \quad (1.4.2)$$

the permeability dyadic [130, 131] is given as

$$\underline{\underline{\mu}} = \mu_0 \underline{\underline{S}}_y \cdot [\mu_a \hat{u}_z \hat{u}_z + \mu_b \hat{u}_x \hat{u}_x + \mu_b \hat{u}_y \hat{u}_y] \cdot \underline{\underline{S}}_y^{-1}, \quad (1.4.3)$$

and the dyadic modeling magnetoelectric properties [130, 131] is given as

$$\underline{\underline{\xi}} = \xi_0 \underline{\underline{S}}_y \cdot [\xi_a \hat{u}_z \hat{u}_z + \xi_b \hat{u}_x \hat{u}_x + \xi_b \hat{u}_y \hat{u}_y] \cdot \underline{\underline{S}}_y^{-1}, \quad (1.4.4)$$

where the rotation dyadic

$$\underline{\underline{S}}_y = \begin{bmatrix} \cos \chi & 0 & -\sin \chi \\ 0 & 1 & 0 \\ \sin \chi & 0 & \cos \chi \end{bmatrix}, \quad (1.4.5)$$

incorporates the tilt χ of the optic axis of the medium with respect to the xz plane, as shown in Fig. 1.4. Whereas ε_a and ε_b represent the relative permittivity scalars of the uniaxial medium, μ_a and μ_b represent the relative permeability scalars, and the relative magnetoelectric properties of the medium are modeled by ξ_a and ξ_b . These parameters are complex-valued and frequency dependent per the causality principle represented by the Kramers–Kronig relations [74]. If the medium is assumed to be non-magnetic then $\underline{\underline{\mu}} = \mu_0 \underline{\underline{I}}$, as I have taken in Chap. 4.

These materials have potential applications in the microwave regime [132, 133] as reciprocal phase shifter [134], non-reflecting shields and antenna radomes [135]. They show optical activity [136], polarization transformation [137–139], circular birefringence and dichroism [140], and absorption [141]. The helicoidal periodicity and structural handedness of these materials can be exploited in a number of realistic applications. For example, these materials can be used in the production of wave plates.

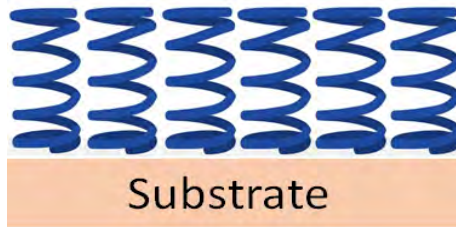


Figure 1.3: The schematic of the uniaxial chiral bianisotropic material when the circular nano helices are assembled perpendicular to the substrate.

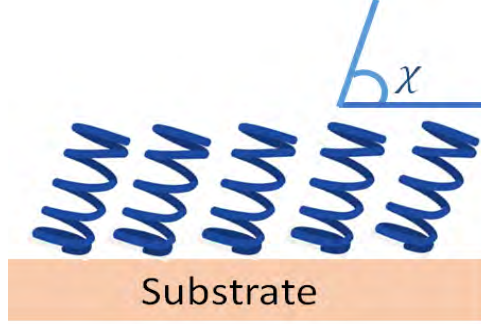


Figure 1.4: The schematic of the uniaxial chiral bianisotropic material when the circular nano helices are assembled at some angle χ to the substrate.

1.5 Canonical Problem

The propagation of electromagnetic surface waves can be unambiguously delineated using the canonical problem of wave propagation by the planar interface formed by the semi-infinitely thick partnering materials. The geometry for the canonical problem of surface-wave propagation is set up by the interface $z = 0$ plane, while the two partnering materials, filling each of half-space on both sides as depicted in Fig. 1.5 for SPP waves.

With the geometry being set up, the next stage is to write expressions for the fields in both half-spaces. Therefore, the fields can be represented in terms of two planewaves of orthogonal polarization states. Since isotropic chiral material supports circularly polarized modes of planewaves, the general field in isotropic chiral material can be written as sum of two circularly polarized modes. However in isotropic dielectric material, such as a metal the two modes can be either linear or circularly polarized. The surface waves must have their tangential electric and magnetic fields continuous across the planar interface $z = 0$. The dispersion relation is then obtained and solved using the boundary conditions and the expressions for field phasors satisfying Maxwell postulates. A condition on the fields is also imposed to make sure the

fields decay perpendicular to the interface. The solution of the dispersion relation determines the wavenumber of the surface wave. The wavenumber of a surface wave is used to determine other quantities that give a deep understanding of the properties of the surface wave. For example, the two quantities describing the surface-wave propagation related to the wavenumber are the phase speed and the propagation length. I present the formulation in Chap. 2.

The solution of the canonical problem obtained as a result of the mathematical manipulation of the dispersion relation can serve as a guide, either for the elucidation of both experimental and theoretical results or to guide the implementation in the prism-coupled configurations.

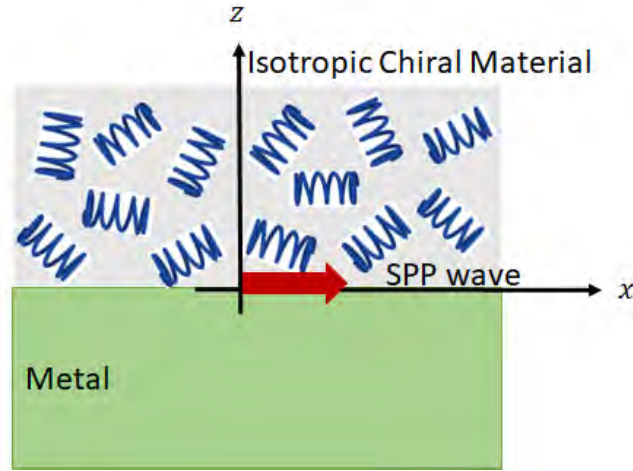


Figure 1.5: The SPP-wave propagation along the interface of an isotropic chiral half-space and a metallic half-space is shown schematically in the canonical problem.

1.6 Prism-Coupled Configurations

The realization of half spaces used in canonical problem is not possible. So, practical setups using finite thickness of materials are used in actual excitation of surface wave. These setups include (i) the most commonly used Turbadar—Kreschmann—Raether (TKR) prism-coupled configuration, (ii) Turbadar—Otto prism-coupled configuration, (iii) Grating-coupled configuration, and (iv) Waveguide-coupled configuration. The choice of experimental setup depends upon the type of application according to the feasibility of the fabrication of the configuration. I have investigated both types of experimental setups of prism-coupled configurations in this thesis. The prism-coupled configurations are the simplest types of configurations to excite the SPP waves. The prism in prism coupling is used for matching the wavenumber of the SPP wave and that of the incident light at the interface of the partnering materials. This matching is a required condition in the excitation of the SPP waves. Furthermore, the solution of the canonical problem helps in the authentic interpretation of the experimental or calculated results obtained in the experimental setups of prism couplings because it provides the wavenumbers of possible surface waves that can exist at the chosen interface. The prism-coupled configurations essentially use evanescent waves to excite the SPP waves. The two types of prism-coupled configurations (i) the Turbadar—Kretschmann—Raether (TKR) configuration [142, 143], and (ii) the Turbadar—Otto configuration [142, 144] are explained in the following subsections.

1.6.1 TKR configuration

The easiest method for the excitation of surface waves is using evanescent wave. It is usually implemented with the TKR configuration. This setup consists of a prism coupled with the isotropic chiral/uniaxially chiral bianisotropic material via a thin metallic layer. A collimated planewave is made incident on one of the two tilted planes of the prism. The metal film should be thin enough so the amplitude of the light emerging from the other side of the metallic film is not too small to excite the surface wave. The θ_{inc} has to be greater than the critical angle inside the prism at

the prism-metal interface for total internal reflection to occur so that the incident wave enters the coupled isotropic chiral/uniaxially chiral bianisotropic material as an evanescent wave. Also, the refractive index of the prism should be greater than the ratio of the $\text{Re}(q)$ of the SPP wave to the free-space wavenumber k_0 . The SPP-wave excitation occurs at that incidence angle where the magnitude of \underline{k} parallel to the interface matches the wavenumber of the possible SPP wave at that interface. When the SPP wave is excited, the absorptance increases (reflectance decreases) and an absorptance peak appears in the angular spectrum of absorptance. Figure 1.6 shows the geometry of the TKR configuration. The TKR configuration is famous because of its easier adaptation to optical sensing of fluids that replaces the partnering isotropic chiral/uniaxially chiral bianisotropic material or infiltrates it.

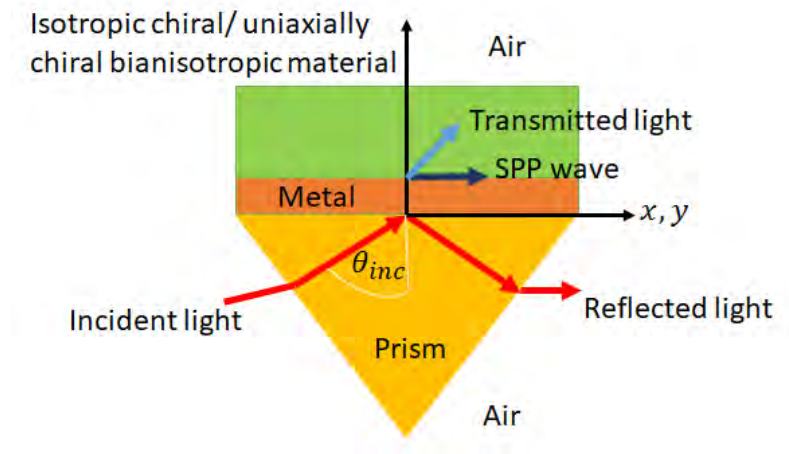


Figure 1.6: The schematic of the Turbadar–Kretschmann–Raether (TKR) configuration.

1.6.2 Turbadar–Otto configuration

An alternative to the TKR configuration is the Turbadar–Otto configuration. In Turbadar–Otto configuration, both the partnering materials are interchanged [11].

The isotropic chiral/uniaxially chiral bianisotropic partnering material is coupled between the metallic film and the prism. The generation of the evanescent waves requires a thinner layer of the isotropic chiral/uniaxially chiral bianisotropic material to appear at the metal with adequate amplitude. Typically, this thickness is of a few hundred nanometers in the optical regime. This configuration offers a clearer and easier identification of the reflectance dips than the TKR prism coupling for the excitation of the SPP waves for an isotropic chiral/uniaxially chiral bianisotropic material. The Turbadar–Otto configuration is more amenable to implementation for the sensing of gases than the liquids. The Turbadar–Otto configuration is shown schematically in Fig. 1.7.

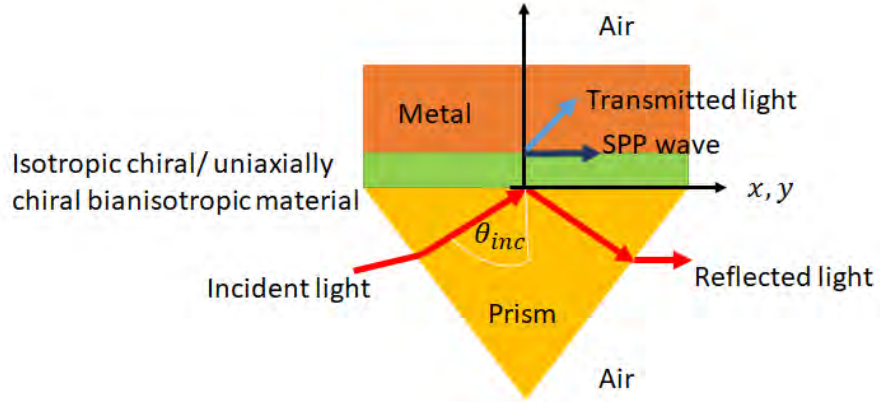


Figure 1.7: The schematic of the Turbadar–Otto configuration.

1.7 Objectives of the Thesis

The objectives of the research conducted for this thesis were to:

1. find the fundamental properties of the partnering chiral materials that are responsible for the propagation and excitation of surface waves;

2. to identify the parametric range of chirality of these partnering chiral materials that support the excitation of surface waves;
3. study the SPP-waves excitation in both the prism-coupled experimental setups with partnering isotropic chiral and bianisotropic chiral materials;
4. the effects of morphology of the partnering uniaxially chiral bianisotropic materials on the characteristics of the SPP waves; and
5. to find out the parametric conditions for the hybrid polarized SPP waves supported by these chiral materials.

1.8 Overview of the Thesis

To achieve objectives (1) and (2), the canonical problem of the electromagnetic surface-wave propagation along the planar interface of two different homogeneous isotropic chiral half-spaces is formulated and solved in Chap. 2. A dispersion relation is obtained and solved to find the complex-valued wavenumbers for surface waves which can propagate along the chiral/chiral interface. The power profiles are also given to validate the existence of the SPP waves.

In Chap. 3, the canonical and prism-coupled configurations are formulated and solved to find the wavenumbers of the possible SPP waves, which can be supported by the metal/isotropic chiral material interface. The reflectances plots and power profiles are also given for objectives (2) and (3).

For objectives, (2), (3), and (5), the SPP-wave excitation at the planar interface of a non-magnetic uniaxially chiral, bianisotropic/plasmonic material is considered in Chap. 4 when the circular nano helixes are assembled perpendicular to the interface and assumed non-magnetic. The SPP waves propagating along the interface are assumed perpendicular to the direction of the chirality and uniaxiality. The effects of variation of the complex-valued chirality parameter on the excitation and nature of the SPP waves are also studied with both the prism-coupled configurations. The power profiles are also given. This chapter lays the foundation for Chap. 5.

The investigation of the excitation and propagation of the SPP wave that can exist at the planar interface of an an obliquely mounted, magnetic uniaxially chiral, bianisotropic and plasmonic material is conducted in Chap. 5 to achieve objectives (2), (3), (4), and (5) when the circular nano helixes are assembled at an angle with the interface. The canonical problem is formulated and numerically solved to find the characteristics of the possible SPP waves for various values of the tilt angle χ of the nano helixes with the substrate for several values of the chirality parameter and a threshold value is found to exist for all tilt angles. The prism-coupled boundary-valued problems are also formulated and solved. The direction of propagation of the SPP waves is restricted to be in the morphologically significant plane of the bianisotropic material that contained tilted helixes. The power profiles are also given. Finally, the summary of the thesis and some suggestions for future work are presented in Chap. 6.

Also, the prism-coupled configurations are investigated and presented in Appendix A of this thesis for the SPP-waves excitation at the interface of a CTF and a plasmonic material as a preliminary context for investigation with uniaxially chiral bianisotropic materials.

References

- [1] M. Faryad and A. Lakhtakia, “On surface plasmon-polariton waves guided by the interface of a metal and a rugate filter with a sinusoidal refractive-index profile,” *J. Opt. Soc. Am. B* **27**, 2218–2223 (2010).
- [2] K. Uller, *Beiträge zur Theorie der Elektromagnetischen, Strahlung*, Ph.D. thesis, Universität Rostock, Chap. XIV (1903).
- [3] J. Zenneck, “Über die fortpflanzung ebener elektromagnetischer wellen längs einer ebenen lieterfläche und ihre beziehung zur drahtlosen telegraphie,” *Ann. Phys. Lpz* **328**, 846–866 (1907).
- [4] A. Sommerfeld, “Über die ausbreitung der wellen in derdrahtlosen telegraphie,” *Ann. Phys. Lpz.* **333**, 665–736 (1909).
- [5] C. J. Bouwkamp, “On Sommerfeld’s surface wave,” *Phys. Rev.* **80**, 294–294 (1950).
- [6] D. A. Hill and J.-R. Wait, “On the excitation of the Zenneck surface wave over the ground at 10MHz,” *Ann. Telecommun.* **35**, 179–182 (1980).
- [7] M. Faryad and A. Lakhtakia, “Grating-coupled excitation of the Uller–Zenneck surface wave in the optical regime,” *J. Opt. Soc. Am. B* **31**, 1706–1711 (2014).
- [8] A. V. Kabashin, P. Evans, S. Pastkovsky, W. Hendren, G. A. Wurtz, and R. Atkinson, “Plasmonic nanorod metamaterials for biosensing,” *Nat. Mater.* **08**, 867–871 (2009).

- [9] S. A. Maier, *Plasmonics: Fundamentals and Applications*, Springer (2007).
- [10] J. Homola (Ed.), *Surface Plasmon Resonance Based Sensors*, Springer (2006).
- [11] J. A. Polo Jr., T. G. Mackay, and A. Lakhtakia, *Electromagnetic Surface Waves: A Modern Perspective*, Elsevier (2013).
- [12] C. Zhou, T. G. Mackay, and A. Lakhtakia, “Surface-plasmon-polariton wave propagation supported by anisotropic materials: Multiple modes and mixed exponential and linear localization characteristics,” *Phys. Rev. A* **100**, 033809 (2019).
- [13] M. Rasheed and M. Faryad, “Rigorous formulation of surface plasmon-polariton waves propagation along the direction of periodicity of one-dimensional photonic crystal,” *J. Opt. Soc. Am. B* **35**, 2957–2962 (2018). Erratum: **36**, 1396 (2019).
- [14] J. A. Polo Jr. and A. Lakhtakia, “On the surface plasmon polariton wave at the planar interface of a metal and a chiral sculptured thin film,” *Proc. R. Soc. A* **465**, 87–107 (2009).
- [15] M. Faryad, J. A. Polo Jr., and A. Lakhtakia, “Multiple trains of same-color surface plasmon-polaritons guided by the planar interface of a metal and a sculptured nematic thin film. Part IV: Canonical problem,” *J. Nanophotonics* **4**, 043505 (2010).
- [16] F. Abbas, Q. A. Naqvi, and M. Faryad, “Multiple surface plasmon–polariton waves guided by the interface of a metal and a periodically nonhomogeneous magnetic material,” *Opt. Commun.* **332**, 109–113 (2014).
- [17] M. Faryad, A. S. Hall, G. D. Barber, T. E. Mallouk, and A. Lakhtakia, “Excitation of multiple surface-plasmon-polariton waves guided by the periodically corrugated interface of a metal and a periodic multilayered isotropic dielectric material,” *J. Opt. Soc. Am. B* **29**, 704–713 (2012).

- [18] F. Chiadini, V. Fiumara, A. Scaglione, and A. Lakhtakia, “Composite surface-plasmon-polariton waves guided by a thin metal layer sandwiched between a homogeneous isotropic dielectric material and a periodically multilayered isotropic dielectric material,” *J. Nanophotonics* **9**, 1–15 (2015).
- [19] F. Abbas and M. Faryad, “A highly sensitive multiplasmonic sensor using hyperbolic chiral sculptured thin films,” *J. Appl. Phys.* **122**, 173104 (2017).
- [20] J. M. Pitarke, V. M. Silkin, E. V. Chulkov, and P. M. Echenique, “Theory of surface plasmons and surface-plasmon polaritons,” *Rep. Prog. Phys.* **70**, 1–87 (2007).
- [21] E. Hendry, T. Carpy, J. Johnston, M. Popland, R. V. Mikhaylovskiy, A. J. Lapthorn, S. M. Kelly, L. D. Barron, N. Gadegaard, and M. Kadodwala, “Ultrasensitive detection and characterization of biomolecules using superchiral fields,” *Nat. Nanotechnol.* **5**, 783–787 (2010).
- [22] A. O. Govorov and Z. Fan, “Theory of chiral plasmonic nanostructures comprising metal nanocrystals and chiral molecular media,” *Chemphyschem* **13**, 2551–2560 (2012).
- [23] B. D. Gupta and R. Kant, “Recent advances in surface plasmon resonance based fiber optic chemical and biosensors utilizing bulk and nanostructures,” *Opt. Laser Technol.* **101**, 144–161 (2018).
- [24] M. Schäferling, X. Yin, and H. Giessen, “Formation of chiral fields in a symmetric environment,” *Opt. Express* **20**, 26326–26336 (2012).
- [25] M. Schäferling, X. Yin, N. Engheta, and H. Giessen, “Helical plasmonic nanostructures as prototypical chiral near-field sources,” *ACS Photonics* **1**, 530–537 (2014).

- [26] M. L. Nesterov, X. Yin, M. Schäferling, H. Giessen, and T. Weiss, “The role of plasmon-generated near fields for enhanced circular dichroism spectroscopy,” *ACS Photonics* **3**, 578–583 (2016).
- [27] N. A. Abdulrahman, Z. Fan, T. Tonooka, S. M. Kelly, N. Gadegaard, E. Hendry, A. O. Govorov, and M. Kadodwala, “Induced chirality through electromagnetic coupling between chiral molecular layers and plasmonic nanostructures,” *Nano Lett.* **12**, 977–983 (2012).
- [28] A. O. Govorov, Z. Fan, P. Hernandez, J. M. Slocik, and R. R. Naik, “Theory of circular dichroism of nanomaterials comprising chiral molecules and nanocrystals: plasmon enhancement, dipole interactions, and dielectric effects,” *Nano Lett.* **10**, 1374–1382 (2010).
- [29] W. M. Mukhtar, S. Shaari, A. A. Ehsan, and P. S. Menon, “Electro-optics interaction imaging in active plasmonic devices,” *Opt. Mater. Express* **4**, 424–433 (2014).
- [30] R. H. Ritchie, “Plasma losses by fast electrons in thin films,” *Phys. Rev.* **106**, 874–881 (1957).
- [31] G. Borstel, H. J. Falge, and A. Otto, *Surface and bulk phonon-polaritons observed by attenuated total reflection*, in: Solid-State Physics. Springer Tracts in Modern Physics, G. Höhler and E. A. Niekisch, Springer-Verlag **74**, 107–148 (1974).
- [32] S. J. Elston and J. R. Sambles, “Surface plasmon-polaritons on an anisotropic substrate,” *J. Mod. Opt.* **37**, 1895–1902 (1990).
- [33] H. Wang, “Excitation of surface plasmon oscillations at an interface between anisotropic dielectric and metallic media,” *Opt. Mater.* **4**, 651–656 (1995).
- [34] I. Abdulhalim, “Surface plasmon TE and TM waves at the anisotropic film-metal interface,” *J. Opt. A: Pure Appl. Opt.* **11**, 015002 (2008).

- [35] R. A. Depine and M. L. Gigli, “Resonant excitation of surface modes at a single flat uniaxial-metal interface,” *J. Opt. Soc. Am. A* **14**, 510–519 (1997).
- [36] D. B. Walker, E. N. Glytsis, and T. K. Gaylord, “Surface mode at isotropic-uniaxial and isotropic-biaxial interfaces,” *J. Opt. Soc. Am. A* **15**, 248–260 (1998).
- [37] J. Noonan and T. G. Mackay, “On electromagnetic surface waves supported by an isotropic chiral material,” *Opt. Commun.* **434**, 224–229 (2019).
- [38] S. He, “Electromagnetic surface waves for some artificial bianisotropic media,” *J. Electromagn. Waves Appl.* **12**, 449–466 (1998).
- [39] A. N. Furs and L. M. Barkovsky, “A new type of surface polaritons at the interface of the magnetic gyrotropic media,” *J. Phys. A: Math. Theor.* **40**, 309–328 (2007).
- [40] R. H. Tarkhanyan and D. G. Niarchos, “Nonradiative surface electromagnetic waves at the interface of uniaxially bianisotropic enantiomeric media,” *Phys. Status Solidi B* **248**, 1499–1504 (2011).
- [41] I. V. Lindell and A. J. Viitanen, “Plane wave propagation in uniaxial bianisotropic medium,” *Electron. Lett.* **29**, 150–152 (1993).
- [42] A. J. Viitanen and I. V. Lindell, “Plane wave propagation in a uniaxial bianisotropic medium with application to a polarization transformer,” *Int. J. Infrared Millim. Waves* **14**, 1993–2010 (1993).
- [43] G. Pellegrini, M. Finazzi, M. Celebrano, L. Duò, and P. Biagioni, “Chiral surface waves for enhanced circular dichroism,” *Phys. Rev. B* **95**, 241402 (2017).
- [44] M. Z. Yaqoob, A. Ghaffar, M. Alkanhal, S.-ur-.Rehman, and F. Razzaz, “Hybrid surface plasmon polariton wave generation and modulation by chiral-graphene-metal (CGM) structure,” *Sci. Rep.* **8**, 18029 (2018).
- [45] A. D. Boardman (Ed.), *Electromagnetic Surface Modes*, Wiley (1982).

- [46] M. Dragoman and D. Dragoman, “Plasmonics: Applications to nanoscale terahertz and optical devices,” *Prog. Quantum Electron.* **32**, 1–41 (2008).
- [47] P. R. West, S. Ishii, G. V. Naik, N. K. Emani, V. M. Shalaev, and A. Boltasseva, “Searching for better plasmonic materials,” *Laser Photon. Rev.* **4**, 795–808 (2010).
- [48] J. A. Polo Jr. and A. Lakhtakia, “Surface electromagnetic waves: A review,” *Laser Photon. Rev.* **5**, 234–246 (2011).
- [49] R. H. Ritchie and H. B. Eldridge, “Optical emission from irradiated foils. I,” *Phys. Rev.* **126**, 1935–1947 (1962).
- [50] F. Abbas, Q. A. Naqvi, and M. Faryad, “Dyakonov–Tamm waves-based optical sensing using sculptured nematic thin film,” *Opt. Eng.* **54**, 067109 (2015).
- [51] F. Abbas, A. Lakhtakia, Q. A. Naqvi, and M. Faryad, “An optical-sensing modality that exploits Dyakonov–Tamm waves,” *Photonics Res.* **03**, 5–8 (2015).
- [52] F. Abbas, M. Faryad, S. E. Swiontek, and A. Lakhtakia, “Enhancement of dynamic sensitivity of multiple surface-plasmonic-polaritonic sensor using silver nanoparticles,” *Plasmonics* **11**, 987–994 (2016).
- [53] S. Erten, M. Faryad, and A. Lakhtakia, “Multiple surface-plasmon-polariton waves guided by a chiral sculptured thin film grown on a metallic grating,” *J. Opt. Soc. Am. B* **34**, 1937–1945 (2017).
- [54] F. Abbas, Q. A. Naqvi, and M. Faryad, “Multiplasmonic optical sensor using sculptured nematic thin films,” *Plasmonics* **10**, 1269–1273 (2015).
- [55] D. Angela and A. K. Alexei, “Principles of nanoparticle imaging using surface plasmons,” *New J. Phys.* **17**, 013041 (2015).
- [56] J. Homola, S. S. Yee, and G. Gauglitz, “Surface plasmon resonance sensors: review,” *Sens. Actuators B Chem.* **54**, 3–15 (1999).

- [57] G. Serafino, A. Malacarne, C. Porzi, P. Ghelfi, M. Presi, and A. D’Errico, “Simultaneous beam steering of multiple signals based on optical wavelength-selective switch,” *Int. J. Microw. Wirel. Technol.* **07**, 391–398 (2015).
- [58] I. De Leon and P. Berini, “Amplification of long-range surface plasmons by a dipolar gain medium,” *Nat. Photonics* **04**, 382–387 (2010).
- [59] I. Abdulhalim, M. Zourob, and A. Lakhtakia, “Surface plasmon resonance for biosensing: A mini-review,” *Electromagnetics* **28**, 214–242 (2008).
- [60] V. Kanda, P. Kitov, D. R. Budle, and M. T. McDermott, “Surface plasmon resonance imaging measurements of the inhibition of Shiga-like toxin by synthetic multivalent inhibitors,” *Anal. Chem.* **77**, 7497–7504 (2005).
- [61] A. Lakhtakia and M. Faryad, “Theory of optical sensing with Dyakonov–Tamm waves,” *J. Nanophotonics* **08**, 083072 (2014).
- [62] I. Abdulhalim, M. Zourob, and A. Lakhtakia, *Handbook of Biosensors and Biochips*, R. Marks, D. Cullen, I. Karube, C. R. Lowe, and H. H. Weetall, eds., Wiley 413–446 (2007).
- [63] K. U.-Aoki, K. Shimada, M. Nagano, M. Kawai, and H. Koga, “A novel approach to protein expression profiling using antibody microarrays combined with surface plasmon resonance technology,” *Proteomics* **5**, 2396–2401 (2005).
- [64] P. G. Kik, S. A. Maier, and H. A. Atwater, “Plasmon printing—A new approach to near-field lithography,” *MRS Symp. Proc.* **705**, 36 (2001).
- [65] S. A. Maier, M. L. Brongersma, P. G. Kik, S. Meltzer, A. A. G. Requicha, and H. A. Atwater, “Plasmonics—A route to nanoscale optical devices,” *Adv. Mater.* **13**, 1501–1505 (2001).
- [66] P. Berini, “Long-range surface plasmon polaritons,” *Adv. Opt. Photon.* **1**, 484–588 (2009).

- [67] M. L. Juan, M. Righini, and R. Quidant, “Plasmon nano-optical tweezers,” *Nat. Photonics* **5**, 349–356 (2011).
- [68] A. V. Zayats and I. I. Smolyaninov, “Near-field photonics: surface plasmon polaritons and localized surface plasmons,” *J. Opt. A: Pure Appl. Opt.* **5**, S16–S50 (2003).
- [69] V. V. Varadan, R. Ro, and V. K. Varadan, “Measurement of the electromagnetic properties of chiral composite materials in the 8-40 GHz range,” *Radio Sci.* **29**, 9–22 (1994).
- [70] C. Train, R. Gheorghe, V. Krstic, L.-M. Chamoreau, N. S. Ovanesyan, G. L. J. A. Rikken, M. Gruselle, and M. Verdaguer “Strong magneto-chiral dichroism in enantiopure chiral ferromagnets,” *Nat. Mater.* **7**, 729–734 (2008).
- [71] D. Bradshaw, J. B. Claridge, E. J. Cussen, T. J. Prior, and M. J. Rosseinsky “Design, chirality, and flexibility in nanoporous molecule-based materials,” *Acc. Chem. Res.* **38**, 273–282 (2005).
- [72] A. J. G-Collado, G. J. M-Cuberos, J. Margineda, M. J. Núñez, and E. Martín, “Isotropic and homogeneous behavior of chiral media based on periodical inclusions of cranks,” *IEEE Microw. Wirel. Compon. Lett.* **20**, 175–177 (2010).
- [73] A. Lakhtakia, *Beltrami Fields in Chiral Media*, World Scientific (1994).
- [74] B. Y.-K. Hu, “Kramers–Kronig in two lines,” *Am. J. Phys.* **57**, 821 (1989).
- [75] D. N. Pattanayak and J. L. Birman, “Wave propagation in optically active and magnetoelectric media of arbitrary geometry,” *Phys. Rev. B* **24**, 4271–4278 (1981).
- [76] M. Chien, Y. Kim, and H. Grebel, “Mode conversion in optically active and isotropic waveguides,” *Opt. Lett.* **14**, 826–828 (1989).

- [77] L. D. Barron, *Molecular Light Scattering and Optical Activity*, Cambridge University Press (1982).
- [78] I. V. Lindell, A. H. Sihvola, S. Tretyakov, and A. J. Viitanen, *Electromagnetic Waves in Chiral and Bi-Isotropic Media*, Artech House (1994).
- [79] N. Engheta and P. Pelet, “Surface waves in chiral layers,” *Opt. Lett.* **16**, 723–725 (1991).
- [80] A. N. Fantino, “Planar interface between a chiral medium and a metal: surface wave excitation,” *J. Mod. Opt.* **43**, 2581–2593 (1996).
- [81] P. Pelet and N. Engheta, “Coupled-mode theory for chirowaveguides,” *J. Appl. Phys.* **67**, 2742 (1990).
- [82] N. Engheta and P. Pelet, “Modes in chirowaveguides,” *Opt. Lett.* **14**, 593–595 (1989).
- [83] D. L. Jaggard and X. Sun, “Theory of chiral multilayers,” *J. Opt. Soc. Am. A* **9**, 804–813 (1992).
- [84] P. Pelet and N. Engheta, “Chirostrip antenna: line source problem,” *J. Electromagn. Waves Appl.* **6**, 771–793 (1992).
- [85] D. L. Jaggard and N. Engheta, “Chirosorb as an invisible medium,” *Electron. Lett.* **25**, 173–174 (1989).
- [86] S. E. Swiontek and A. Lakhtakia, “Vacuum-metal-deposition and columnar-thin-film techniques implemented in the same apparatus,” *Mater. Lett.* **142**, 291–293 (2015).
- [87] A. Lakhtakia and R. Messier, *Sculptured Thin Films: Nanoengineered Morphology and Optics*, SPIE. Press (2005).
- [88] N. O. Young and J. Kowal, “Optically active fluorite films,” *Nature* **183**, 104–105 (1959).

- [89] E. F. Dawson and N. O. Young, “Helical Kerr cell,” *J. Opt. Soc. Am.* **50**, 170–171 (1960).
- [90] Q. Wu, I. J. Hodgkinson, and A. Lakhtakia, “Circular polarization filters made of chiral sculptured thin films: experimental and simulation results,” *Opt. Engg.* **39**, 1863–1868 (2000).
- [91] A. Lakhtakia and V. C. Venugopal, “Dielectric thin-film helicoidal bianisotropic medium bilayers as tunable polarization-independent laser mirrors and notch filters,” *Microw. Opt. Technol. Lett.* **17**, 135–140 (1998).
- [92] A. Lakhtakia and I. J. Hodgkinson, “Spectral response of dielectric thin-film helicoidal bianisotropic medium bilayer,” *Opt. Commun.* **167**, 191–202 (1999).
- [93] A. Lakhtakia, “Stepwise chirping of chiral sculptured thin films for Bragg bandwidth enhancement,” *Microw. Opt. Technol. Lett.* **28**, 323–326 (2001).
- [94] F. Chiadini and A. Lakhtakia, “Design of wideband circular-polarization filters made of chiral sculptured thin films,” *Microw. Opt. Technol. Lett.* **42**, 135–138 (2004).
- [95] A. Lakhtakia, “Axial excitation of tightly interlaced chiral sculptured thin films: “averaged” circular Bragg phenomenon,” *Optik* **112**, 119–124 (2001).
- [96] M. Suzuki, S. Tokito, and Y. Taga, “Review of thin film technology in automobile industry,” *Mater. Sci. Engg. B* **51**, 66–71 (1998).
- [97] Y. Taga, “Review of plasma thin-film technology in automobile industry,” *Surf. Coat. Technol.* **112**, 339–346 (1999).
- [98] A. Lakhtakia, M. W. McCall, J. A. Sherwin, Q. H. Wu, and I. J. Hodgkinson, “Sculptured-thin-film spectral holes for optical sensing of fluids,” *Opt. Commun.* **194**, 33–46 (2001).

- [99] M. W. McCall and A. Lakhtakia, “Polarization-dependent narrowband spectral filtering by chiral sculptured thin films,” *J. Mod. Opt.* **47**, 743–755 (2000).
- [100] A. Lakhtakia, “On determining gas concentrations using thin-film helicoidal bianisotropic medium bilayers,” *Sens. Actuat. B: Chem.* **52**, 243–250 (1998).
- [101] E. Ertekin and A. Lakhtakia, “Sculptured thin film Šolc filters for optical sensing of gas concentration,” *Eur. Phys. J. Appl. Phys.* **5**, 45–50 (1999).
- [102] I. J. Hodgkinson, Q. Wu, and K. M. McGrath, “Moisture adsorption effects in biaxial and chiral optical thin film coatings,” in: Engineered Nanostructural Films and Materials, A. Lakhtakia and R. F. Messier, eds., *Proc. SPIE*. **3790**, 184–194 (1999).
- [103] J. C. Sit, D. J. Broer, and M. J. Brett, “Liquid crystal alignment and switching in porous chiral thin films,” *Adv. Mater.* **12**, 371–373 (2000).
- [104] A. Lakhtakia, “Towards sculptured thin films (STFs) as optical interconnects,” *Optik* **110**, 289–293 (1999).
- [105] E. Ertekin and A. Lakhtakia, “Optical interconnects realizable with thin-film helicoidal bianisotropic mediums,” *Proc. Roy. Soc. Lond. A* **457**, 817–836 (2001).
- [106] J. B. Geddes III and A. Lakhtakia, “Reflection and transmission of optical narrow-extent pulses by axially excited chiral sculptured thin films,” *Eur. Phys. J. Appl. Phys.* **13**, 3–14 (2001). Corrections: **16**, 247 (2001).
- [107] J. B. Geddes III and A. Lakhtakia, “Pulse-coded information transmission across an axially excited chiral sculptured thin film in the Bragg regime,” *Microw. Opt. Technol. Lett.* **28**, 59–62 (2001).
- [108] A. Lakhtakia, “On bioluminescent emission from chiral sculptured thin films,” *Opt. Commun.* **188**, 313–320 (2001).

- [109] A. Lakhtakia and M. W. Horn, “Bragg-regime engineering by columnar thinning of chiral sculptured thin films,” *Optik* **114**, 556–560 (2003).
- [110] R. Messier, V. C. Venugopal, and P. D. Sunal, “Origin and evolution of sculptured thin films,” *J. Vac. Sci. Technol. A* **18**, 1538–1545 (2000).
- [111] M. Malac and R. F. Egerton, “Observations of the microscopic growth mechanism of pillars and helices formed by glancing-angle thin-film deposition,” *J. Vac. Sci. Technol. A* **19**, 158–166 (2001).
- [112] M. Malac and R. F. Egerton, “Thin-film regular-array structures with 10-100 nm repeat distance,” *Nanotechnology* **12**, 11–13 (2001).
- [113] D. Felbacq and F. Zolla, “Scattering theory of photonic crystals,” in: Introduction to Complex Mediums for Optics and Electromagnetics, W. S. Weiglhofer and A. Lakhtakia, eds., *Proc. SPIE.*, (2003).
- [114] J. W. Haus, “Photonic band gap structures,” in: Nanometer structures: Theory, modeling, and simulation, A. Lakhtakia, ed., *Proc. SPIE.*, (2004).
- [115] A. Lakhtakia, “Wave propagation in a piezoelectric, continuously twisted, structurally chiral medium along the axis of spirality,” *Appl. Acoust.* **44**, 25–37 (1995). Corrections: **44**, 385 (1995).
- [116] A. Lakhtakia, “Exact analytic solution for oblique propagation in a piezoelectric, continuously twisted, structurally chiral medium,” *Appl. Acoust.* **49**, 225–236 (1996).
- [117] C. Oldano and S. Ponti, “Acoustic wave propagation in structurally helical media,” *Phys. Rev. E* **63**, 011703 (2000).
- [118] A. Lakhtakia and M. W. Meredith, “Shear axial modes in a PCTSCM. Part IV: bandstop and notch filters,” *Sens. Actuat. A: Phys.* **73**, 193–200 (1999).

- [119] A. Lakhtakia, “Shear axial modes in a PCTSCM. Part VI: simpler transmission spectral holes,” *Sens. Actuat. A: Phys.* **87**, 78–80 (2000).
- [120] A. Lakhtakia, K. Robbie, and M.J. Brett, “Spectral Green’s function for wave excitation and propagation in a piezoelectric, continuously twisted, structurally chiral medium,” *J. Acoust. Soc. Am.* **101**, 2052–2059 (1997).
- [121] R. A. Hassler, G. G. Gregory, and E. R. Freniere, “Modeling birefringence in optomechanical design and analysis software,” in: Optical Design and Analysis Software II, R. C. Juergens, ed., *Proc. SPIE.* **4769**, 43–54 (2002).
- [122] W. S. Otaguro, E. W.-Avnear, S. P. S. Porto, and J. Smith, “Oblique Polaritons in Uniaxial Crystals: Application to LiIO_3 ,” *Phys. Rev. B* **6**, 3100–3104 (1972).
- [123] G. Irmer, C. Röder, C. Himcinschi, and J. Kortus, “Phonon polaritons in uniaxial crystals: A Raman scattering study of polaritons in $\alpha\text{-GaN}$,” *Phys. Rev. B* **88**, 104303 (2013).
- [124] T. G. Mackay and A. Lakhtakia, “Modeling columnar thin films as platforms for surface plasmonic-polaritonic optical sensing,” *Photonics Nanostruct. Fund. Appl.* **8**, 140–149 (2010).
- [125] S. E. Swiontek, M. Faryad, and A. Lakhtakia, “Surface plasmonic polaritonic sensor using a dielectric columnar thin film,” *J. Nanophotonics* **8**, 083986 (2014).
- [126] S. E. Swiontek and A. Lakhtakia, “Influence of silver-nanoparticle layer in a chiral sculptured thin film for surface-multiplasmonic sensing of analytes in aqueous solution,” *J. Nanophotonics* **10**, 033008 (2016).
- [127] K. V. Sreekanth, Y. Alapan, M. ElKabbash, E. Ilker, M. Hinczewski, U. A. Gurkan, A. D. Luca, and G. Strangi, “Extreme sensitivity biosensing platform based on hyperbolic metamaterials,” *Nat. Mater.* **15**, 621–627 (2016).

- [128] M. Faryad, “Surface plasmon-polariton waves guided by reciprocal, uniaxially chiral, bianisotropic material,” in: Plasmonics: Design, Materials, Fabrication, Characterization, and Applications XVII, D. P. Tsai and T. Tanaka, eds., *Proc. SPIE*. **11082**, 60–66 (2019).
- [129] I. V. Lindell, A. J. Viitanen, and P. K. Koivisto, “Plane-wave propagation in a transversely bianisotropic uniaxial medium,” *Microwave Opt. Technol. Lett.* **6**, 478–481 (1993).
- [130] C. Y. Chung and K. W. Whites, “Effective constitutive parameters for an artificial uniaxial bianisotropic chiral medium,” *J. Electromagn. Waves Appl.* **10**, 1363–1388 (1996).
- [131] K. W. Whites and C. Y. Chung, “Composite uniaxial bianisotropic chiral materials characterization: comparison of predicted and measured scattering,” *J. Electromagn. Waves Appl.* **11**, 371–394 (1997).
- [132] S. A. Tretyakov and A. A. Sochava, “Novel uniaxial bianisotropic materials: reflection and transmission in planar structures,” *Prog. Electromagn. Res.* **9**, 157–179 (1994).
- [133] I. P. Theron and J. H. Cloete, “The optical activity of an artificial non-magnetic uniaxial chiral crystal at microwave frequencies,” *J. Electromagn. Waves Appl.* **10**, 539–561 (1996).
- [134] M. M. I. Saadoun and N. Engheta, “A reciprocal phase shifter using novel pseudo-chiral or Ω medium,” *Microwave and Opt. Technol. Lett.* **5**, 184–188 (1992).
- [135] S. A. Tretyakov and A. A. Sochava, “Proposed composite material for nonreflecting shields and antenna radomes,” *Electron. Lett.* **29**, 1048–1049 (1993).
- [136] I. Tinoco Jr. and M. P. Freeman, “The optical activity of oriented copper helices. I. Experimental,” *J. Phys. Chem.* **61**, 1196–1200 (1957).

- [137] P. Koivisto, “Polarization properties of plane waves in transversely bianisotropic uniaxial medium,” *Microwave Opt. Technol. Lett.* **6**, 858–862 (1993).
- [138] A. J. Viitanen and I. V. Lindell, “Uniaxial chiral quarter-wave polarisation transformer,” *Electron. Lett.* **29**, 1074–1075 (1993).
- [139] I. V. Lindell and A. H. Sihvola, “Plane-wave reflection from uniaxial chiral interface and its application to polarization transformation,” *IEEE Trans. Antennas Propagat.* **43**, 1397–1404 (1995).
- [140] R. E. Raab and J. H. Cloete, “An eigenvalue theory of circular birefringence and dichroism in a non-magnetic chiral medium,” *J. Electromagn. Waves Appl.* **8**, 1073–1089 (1994).
- [141] C. R. B.-Taylor, “Modelling of helix-loaded chiral radar-absorbing layers,” *Proc. of Chiral’94*, 83–88 (1994).
- [142] T. Turbadar, “Complete absorption of light by thin metal films,” *Proc. Phys. Soc.* **73**, 40–44 (1959).
- [143] E. Kretschmann and H. Raether, “Radiative decay of non radiative surface plasmons excited by light,” *Z. Naturforsch* **23**, 2135–2136 (1968).
- [144] A. Otto, “Excitation of nonradiative surface plasma waves in silver by the method of frustrated total reflection,” *Z. Phys.* **216**, 398–410 (1968).

Chapter 2

Two Isotropic Chiral Materials

This thesis is concerned with electromagnetic surface waves propagating along the interfaces of isotropic chiral and uniaxially bianisotropic chiral materials. Therefore, I start with the simple case of the surface-wave propagation by an interface of two isotropic chiral materials. The characteristics of surface waves propagating along the planar interface of isotropic chiral materials \mathcal{A} and \mathcal{B} is studied using the setting of the canonical boundary-value problem. The material \mathcal{B} is taken to be a homogenized composite material made by the homogenization of an isotropic achiral, nonmagnetic component material and isotropic chiral material. The achiral material is specified by $\varepsilon_a^{\mathcal{B}}$ as the relative permittivity. The properties of the surface waves are then investigated to elucidate the effect of the volume fraction.

Chapter 2 is planned as follows: Introduction and related literature review is given in Sec. 2.1 and the formulation for the canonical problem is provided in Sec. 2.2. The illustrative numerical results are presented and discussed in Sec. 2.3. Conclusions are given in Sec. 2.4.

2.1 Introduction

The planar interface of two different materials can support the surface-waves propagation. Since the early 1900s, several different surface waves have been discovered.

The work reported in this chapter is published in: *J. Opt. Soc. Am. B* **36**, F1-F8 (2019).

The type assigned to a given surface wave depends upon whether the materials are dissipative or nondissipative, isotropic or anisotropic, homogeneous or nonhomogeneous, etc. [1]. The interface of a dielectric material and a plasmonic material guides the SPP wave [2, 3], which is the most well-known type of surface electromagnetic waves. The partnering materials for SPP waves may be isotropic or anisotropic [4]. Uses for these waves are found in optical sensing [5, 6]. Another well-known type of surface electromagnetic waves is the Dyakonov wave [7, 8], which is guided by the isotropic dielectric-anisotropic dielectric interface [9, 10]. Dyakonov waves are generally associated with small angular existence domains [11] but larger angular existence domains can be supported if the partnering materials are dissipative [12–15]. Surface waves that are intermediate in properties, in part alike to SPP waves and in part alike to Dyakonov waves, can be supported by hyperbolic materials [4, 16, 17].

Owing to their inherent magneto-electric coupling, chiral materials [18] allow broader possibilities for surface-wave propagation than achiral materials. To date, surface-wave propagation guided by chiral materials has not been widely studied [19–22], in comparison to achiral materials. Most of these studies have concentrated on interfaces of non-dissipative chiral materials and isotropic plasmonic materials. The surface waves in these studies are essentially SPP waves. Recently, surface waves propagating along the planar interfaces of anisotropic achiral materials and chiral materials were explored numerically [23]. In Ref. [23], surface waves alike to Dyakonov waves were found to be supported when the achiral material was a dielectric material while surface waves alike to SPP waves were found to be supported when the achiral material was taken as a metal.

In this chapter, I consider the previously unexplored case of surface-wave propagation along the interface of two isotropic chiral materials. The dispersion relation corresponding to the canonical problem [1] is derived and solutions are extracted numerically. To allow greater flexibility for numerical investigations, both isotropic chiral partnering materials are modeled as homogenized composite materials (HCMs) [24].

Furthermore, a new type of chiral material that can support amplification and attenuation of planewaves is utilized. The amplification or attenuation depends upon the polarization state of the planewaves [25].

2.2 Canonical Problem

Let me consider the canonical problem for surface electromagnetic waves [1] propagating along the interface of two different chiral materials as shown in Fig. 2.1. Both materials are taken as homogeneous. An isotropic chiral material, named as \mathcal{A} ,

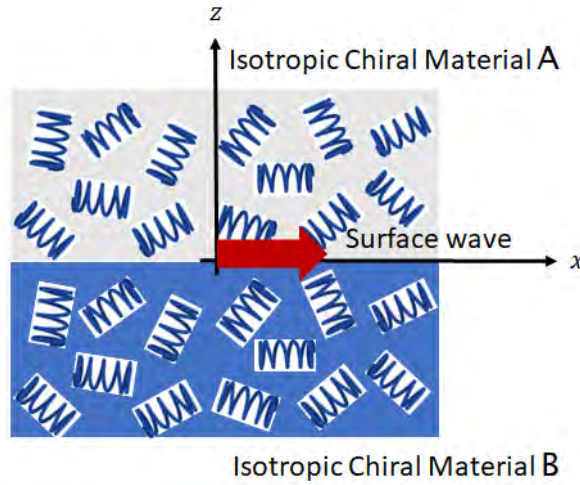


Figure 2.1: The interface of two isotropic chiral materials \mathcal{A} and \mathcal{B} is shown schematically as a canonical problem. Since material \mathcal{A} occupies half space $z > 0$.

occupies the half-space $z > 0$ and is specified by Tellegen constitutive relations in the frequency-domain [18]

$$\left. \begin{aligned} \underline{D}(\underline{r}, \omega) &= \varepsilon_0 \varepsilon^{\mathcal{A}} \underline{E}(\underline{r}, \omega) + i\sqrt{\varepsilon_0 \mu_0} \xi^{\mathcal{A}} \underline{H}(\underline{r}, \omega) \\ \underline{B}(\underline{r}, \omega) &= -i\sqrt{\varepsilon_0 \mu_0} \xi^{\mathcal{A}} \underline{E}(\underline{r}, \omega) + \mu_0 \mu^{\mathcal{A}} \underline{H}(\underline{r}, \omega) \end{aligned} \right\}, \quad z > 0, \quad (2.2.1)$$

while an isotropic chiral material, named as \mathcal{B} , occupies the half-space $z < 0$ and is specified by Tellegen constitutive relations in the frequency-domain [18]

$$\left. \begin{aligned} \underline{D}(\underline{r}, \omega) &= \varepsilon_0 \varepsilon^{\mathcal{B}} \underline{E}(\underline{r}, \omega) + i\sqrt{\varepsilon_0 \mu_0} \xi^{\mathcal{B}} \underline{H}(\underline{r}, \omega) \\ \underline{B}(\underline{r}, \omega) &= -i\sqrt{\varepsilon_0 \mu_0} \xi^{\mathcal{B}} \underline{E}(\underline{r}, \omega) + \mu_0 \mu^{\mathcal{B}} \underline{H}(\underline{r}, \omega) \end{aligned} \right\}, \quad z < 0. \quad (2.2.2)$$

The relative permittivity scalars $\varepsilon^{\mathcal{A}, \mathcal{B}}$, the relative permeability scalars $\mu^{\mathcal{A}, \mathcal{B}}$, and the relative chirality pseudoscalars $\xi^{\mathcal{A}, \mathcal{B}}$ are generally complex-valued and frequency dependent, per the causality principle represented by the Kramers–Kronig relations [26].

The field phasors of the electromagnetic wave in the materials \mathcal{A} and \mathcal{B} are represented by

$$\left. \begin{aligned} \underline{E}_\ell(\underline{r}) &= \underline{\mathcal{E}}_\ell \exp(i\mathbf{k}_\ell \cdot \underline{r}) \\ \underline{H}_\ell(\underline{r}) &= \underline{\mathcal{H}}_\ell \exp(i\mathbf{k}_\ell \cdot \underline{r}) \end{aligned} \right\}, \quad \ell \in \{\mathcal{A}, \mathcal{B}\}. \quad (2.2.3)$$

The amplitude vectors $\underline{\mathcal{E}}_\ell$, $\underline{\mathcal{H}}_\ell$ and wave vector \mathbf{k}_ℓ are complex-valued, in general. Let me assume that the surface wave propagates parallel to $\hat{\underline{u}}_x$ in the xy plane.

The Maxwell curl postulates yield

$$\left. \begin{aligned} \mathbf{k}_\ell \times \underline{\mathcal{E}}_\ell - \omega (-i\sqrt{\varepsilon_0 \mu_0} \xi^\ell \underline{\mathcal{E}}_\ell + \mu_0 \mu^\ell \underline{\mathcal{H}}_\ell) &= \underline{0} \\ \mathbf{k}_\ell \times \underline{\mathcal{H}}_\ell + \omega (\varepsilon_0 \varepsilon^\ell \underline{\mathcal{E}}_\ell + i\sqrt{\varepsilon_0 \mu_0} \xi^\ell \underline{\mathcal{H}}_\ell) &= \underline{0} \end{aligned} \right\}, \quad (2.2.4)$$

with $\ell = \mathcal{A}$ for half-space $z > 0$ and $\ell = \mathcal{B}$ for half-space $z < 0$. The wave vector

$$\underline{\mathbf{k}}_\ell \equiv \begin{cases} \underline{\mathbf{k}}_{\mathcal{A}} = k_0 (q \hat{\underline{u}}_x + i\alpha_{\mathcal{A}} \hat{\underline{u}}_z), & z > 0 \\ \underline{\mathbf{k}}_{\mathcal{B}} = k_0 (q \hat{\underline{u}}_x - i\alpha_{\mathcal{B}} \hat{\underline{u}}_z), & z < 0 \end{cases}, \quad (2.2.5)$$

with $\text{Re}\{\alpha_\ell\} > 0$ ($\ell \in \{\mathcal{A}, \mathcal{B}\}$) for surface-wave propagation. On merging Eq. (2.2.4) and Eq. (2.2.5), a dispersion relation arises for α_ℓ ($\ell \in \{\mathcal{A}, \mathcal{B}\}$). The two α_ℓ roots with non-negative real parts are classified as

$$\left. \begin{aligned} \alpha_{\ell 2} &= \sqrt{q^2 - \kappa_{\ell L}^2} \\ \alpha_{\ell 1} &= \sqrt{q^2 - \kappa_{\ell R}^2} \end{aligned} \right\}, \quad (2.2.6)$$

with the complex-valued scalars

$$\left. \begin{aligned} \kappa_{\ell L} &= \sqrt{\varepsilon^\ell \mu^\ell} - \xi^\ell \\ \kappa_{\ell R} &= \sqrt{\varepsilon^\ell \mu^\ell} + \xi^\ell \end{aligned} \right\} \quad (2.2.7)$$

being correlated with the relative wavenumbers for left and right circularly-polarized light, respectively, in an unbounded chiral medium [18]. Accordingly, the amplitudes of the electromagnetic field-phasor are represented as

$$\left. \begin{aligned} \underline{\mathcal{E}}_\ell &= C_{\ell 1} \underline{\mathcal{E}}_{\ell 1} + C_{\ell 2} \underline{\mathcal{E}}_{\ell 2} \\ \underline{\mathcal{H}}_\ell &= \sqrt{\frac{\varepsilon_0}{\mu_0}} \sqrt{\frac{\varepsilon^\ell}{\mu^\ell}} (C_{\ell 1} \underline{\mathcal{H}}_{\ell 1} + C_{\ell 2} \underline{\mathcal{H}}_{\ell 2}) \end{aligned} \right\}, \quad \ell \in \{\mathcal{A}, \mathcal{B}\}, \quad (2.2.8)$$

where the vectors

$$\left. \begin{aligned} \underline{\mathcal{E}}_{\mathcal{A}1} &= \alpha_{\mathcal{A}1} \hat{u}_x + \kappa_{\mathcal{A}R} \hat{u}_y + iq \hat{u}_z \\ \underline{\mathcal{E}}_{\mathcal{A}2} &= -\alpha_{\mathcal{A}2} \hat{u}_x + \kappa_{\mathcal{A}L} \hat{u}_y - iq \hat{u}_z \\ \underline{\mathcal{H}}_{\mathcal{A}1} &= -i\alpha_{\mathcal{A}1} \hat{u}_x - i\kappa_{\mathcal{A}R} \hat{u}_y + q \hat{u}_z \\ \underline{\mathcal{H}}_{\mathcal{A}2} &= -i\alpha_{\mathcal{A}2} \hat{u}_x + i\kappa_{\mathcal{A}L} \hat{u}_y + q \hat{u}_z \end{aligned} \right\}, \quad (2.2.9)$$

and

$$\left. \begin{aligned} \underline{\mathcal{E}}_{\mathcal{B}1} &= -\alpha_{\mathcal{B}1} \hat{u}_x + \kappa_{\mathcal{B}R} \hat{u}_y + iq \hat{u}_z \\ \underline{\mathcal{E}}_{\mathcal{B}2} &= \alpha_{\mathcal{B}2} \hat{u}_x + \kappa_{\mathcal{B}L} \hat{u}_y - iq \hat{u}_z \\ \underline{\mathcal{H}}_{\mathcal{B}1} &= i\alpha_{\mathcal{B}1} \hat{u}_x - i\kappa_{\mathcal{B}R} \hat{u}_y + q \hat{u}_z \\ \underline{\mathcal{H}}_{\mathcal{B}2} &= i\alpha_{\mathcal{B}2} \hat{u}_x + i\kappa_{\mathcal{B}L} \hat{u}_y + q \hat{u}_z \end{aligned} \right\}. \quad (2.2.10)$$

The four scalars $C_{\mathcal{A}1,2}$ and $C_{\mathcal{B}1,2}$ introduced in Eq. (2.2.8), as well as the relative wavenumber q/k_0 , are found by using boundary conditions across the $z = 0$ planar interface, as follows. Standard boundary conditions on the electromagnetic field phasors impose four conditions. These four boundary conditions result from equating the tangential components of the electromagnetic field phasors across the planar interface

$z = 0$, which are,

$$\left. \begin{aligned} \underline{u}_x \cdot \underline{\mathcal{E}}(z = 0-) &= \underline{u}_x \cdot \underline{\mathcal{E}}(z = 0+) \\ \underline{u}_y \cdot \underline{\mathcal{E}}(z = 0-) &= \underline{u}_y \cdot \underline{\mathcal{E}}(z = 0+) \\ \underline{u}_x \cdot \underline{\mathcal{H}}(z = 0-) &= \underline{u}_x \cdot \underline{\mathcal{H}}(z = 0+) \\ \underline{u}_y \cdot \underline{\mathcal{H}}(z = 0-) &= \underline{u}_y \cdot \underline{\mathcal{H}}(z = 0+) \end{aligned} \right\}. \quad (2.2.11)$$

These result in

$$\left. \begin{aligned} \hat{\underline{u}}_x \cdot (\underline{\mathcal{E}}_{\mathcal{B}1} + \underline{\mathcal{E}}_{\mathcal{B}2}) &= \hat{\underline{u}}_x \cdot (\underline{\mathcal{E}}_{\mathcal{A}1} + \underline{\mathcal{E}}_{\mathcal{A}2}) \\ \hat{\underline{u}}_y \cdot (\underline{\mathcal{E}}_{\mathcal{B}1} + \underline{\mathcal{E}}_{\mathcal{B}2}) &= \hat{\underline{u}}_y \cdot (\underline{\mathcal{E}}_{\mathcal{A}1} + \underline{\mathcal{E}}_{\mathcal{A}2}) \\ \hat{\underline{u}}_x \cdot (\underline{\mathcal{H}}_{\mathcal{B}1} + \underline{\mathcal{H}}_{\mathcal{B}2}) &= \hat{\underline{u}}_x \cdot (\underline{\mathcal{H}}_{\mathcal{A}1} + \underline{\mathcal{H}}_{\mathcal{A}2}) \\ \hat{\underline{u}}_y \cdot (\underline{\mathcal{H}}_{\mathcal{B}1} + \underline{\mathcal{H}}_{\mathcal{B}2}) &= \hat{\underline{u}}_y \cdot (\underline{\mathcal{H}}_{\mathcal{A}1} + \underline{\mathcal{H}}_{\mathcal{A}2}) \end{aligned} \right\}, \quad (2.2.12)$$

which may be expressed compactly as

$$[\underline{\underline{Y}}] \cdot \begin{bmatrix} C_{\mathcal{A}1} \\ C_{\mathcal{A}2} \\ C_{\mathcal{B}1} \\ C_{\mathcal{B}2} \end{bmatrix} = \begin{bmatrix} 0 \\ 0 \\ 0 \\ 0 \end{bmatrix}, \quad (2.2.13)$$

wherein the 4×4 matrix

$$[\underline{\underline{Y}}] = \begin{bmatrix} \alpha_{\mathcal{A}1} & -\alpha_{\mathcal{A}2} & \alpha_{\mathcal{B}1} & -\alpha_{\mathcal{B}2} \\ \kappa_{\mathcal{A}R} & \kappa_{\mathcal{A}L} & -\kappa_{\mathcal{B}R} & -\kappa_{\mathcal{B}L} \\ \alpha_{\mathcal{A}1} \sqrt{\frac{\varepsilon_{\mathcal{A}}}{\mu_{\mathcal{A}}}} & \alpha_{\mathcal{A}2} \sqrt{\frac{\varepsilon_{\mathcal{A}}}{\mu_{\mathcal{A}}}} & \alpha_{\mathcal{B}1} \sqrt{\frac{\varepsilon_{\mathcal{B}}}{\mu_{\mathcal{B}}}} & \alpha_{\mathcal{B}2} \sqrt{\frac{\varepsilon_{\mathcal{B}}}{\mu_{\mathcal{B}}}} \\ -\kappa_{\mathcal{A}R} \sqrt{\frac{\varepsilon_{\mathcal{A}}}{\mu_{\mathcal{A}}}} & \kappa_{\mathcal{A}L} \sqrt{\frac{\varepsilon_{\mathcal{A}}}{\mu_{\mathcal{A}}}} & \kappa_{\mathcal{B}R} \sqrt{\frac{\varepsilon_{\mathcal{B}}}{\mu_{\mathcal{B}}}} & -\kappa_{\mathcal{B}L} \sqrt{\frac{\varepsilon_{\mathcal{B}}}{\mu_{\mathcal{B}}}} \end{bmatrix}. \quad (2.2.14)$$

The matrix $[\underline{\underline{Y}}]$ must be singular for a nontrivial solution to Eq. (2.2.13). Hence the dispersion equation

$$\det[\underline{\underline{Y}}] = 0 \quad (2.2.15)$$

arises, from which q/k_0 can be derived by numerical methods [28]. After q/k_0 is found, relative values of the four scalars $C_{\mathcal{A}1,2}$ and $C_{\mathcal{B}1,2}$ can be obtained from Eq. (2.2.13) by straightforward algebraic manipulations.

2.3 Numerical Studies

The materials \mathcal{A} and \mathcal{B} are both isotropic chiral materials [18], per the Tellegen constitutive relations (2.2.1). To allow flexibility in specifying the constitutive parameters for these materials, both materials \mathcal{A} and \mathcal{B} are modeled as HCMs. Specifically, material $\ell \in \{\mathcal{A}, \mathcal{B}\}$ arises from the homogenization of two component materials, namely component material ℓ_a which is an achiral, nonmagnetic, isotropic material characterized by the relative permittivity ε_a^ℓ and component material ℓ_b which is an isotropic chiral material characterized by the relative constitutive parameters ε_b^ℓ , μ_b^ℓ , and ξ_b^ℓ per the Tellegen constitutive relations (2.2.1). Both component materials in each half-space $z \lesseqgtr 0$ are assumed to be randomly distributed as electrically small spheres, with the volume fraction of component material ℓ_a being f_a^ℓ and that of component material ℓ_b being $f_b^\ell = 1 - f_a^\ell$.

Estimates of the constitutive parameters of the materials \mathcal{A} and \mathcal{B} , namely ε^ℓ , μ^ℓ , and ξ^ℓ ($\ell \in \{\mathcal{A}, \mathcal{B}\}$), are provided by the Bruggeman homogenization formalism [24, 29]. This process involves numerically solving the following nonlinear matrix equation:

$$\begin{aligned} f_a^\ell \left(\left[\underline{\underline{K}}_a^\ell \right] - \left[\underline{\underline{K}}^\ell \right] \right) \cdot \left\{ \left[\underline{\underline{I}} \right] + \left[\underline{\underline{D}}^\ell \right] \cdot \left(\left[\underline{\underline{K}}_a^\ell \right] - \left[\underline{\underline{K}}^\ell \right] \right) \right\}^{-1} = \\ f_b^\ell \left(\left[\underline{\underline{K}}^\ell \right] - \left[\underline{\underline{K}}_b^\ell \right] \right) \cdot \left\{ \left[\underline{\underline{I}} \right] + \left[\underline{\underline{D}}^\ell \right] \cdot \left(\left[\underline{\underline{K}}_b^\ell \right] - \left[\underline{\underline{K}}^\ell \right] \right) \right\}^{-1}, \end{aligned} \quad (2.3.1)$$

wherein the constitutive 2×2 matrices

$$\left. \begin{aligned} \left[\underline{\underline{K}}_a^\ell \right] &= \begin{bmatrix} \varepsilon_a^\ell & 0 \\ 0 & 1 \end{bmatrix} \\ \left[\underline{\underline{K}}_b^\ell \right] &= \begin{bmatrix} \varepsilon_b^\ell & i\xi_b^\ell \\ -i\xi_b^\ell & \mu_b^\ell \end{bmatrix} \\ \left[\underline{\underline{K}}^\ell \right] &= \begin{bmatrix} \varepsilon^\ell & i\xi^\ell \\ -i\xi^\ell & \mu^\ell \end{bmatrix} \end{aligned} \right\}, \quad (2.3.2)$$

the depolarization 2×2 matrix

$$\left[\underline{\underline{D}}^\ell \right] = \frac{1}{3 \left[\varepsilon^\ell \mu^\ell + (\xi^\ell)^2 \right]} \begin{bmatrix} \mu^\ell & -\xi^\ell \\ \xi^\ell & \varepsilon^\ell \end{bmatrix}, \quad (2.3.3)$$

and $\left[\underline{\underline{I}} \right]$ represents the 2×2 identity matrix.

For the isotropic chiral component material, for both materials \mathcal{A} and \mathcal{B} , the relative constitutive parameters $\varepsilon_b^{\mathcal{A}} = \varepsilon_b^{\mathcal{B}} = 3 + 0.01i$, $\mu_b^{\mathcal{A}} = \mu_b^{\mathcal{B}} = 0.95 + 0.0002i$, and $\xi_b^{\mathcal{A}} = \xi_b^{\mathcal{B}} = 0.1 + 0.001i$ were fixed. These values are consistent with certain mildly dissipative, isotropic chiral metamaterials [30]. For the isotropic achiral component material for partnering material \mathcal{A} , I fixed $\varepsilon_a^{\mathcal{A}} = 2 - 0.02i$. Thus, the component material \mathcal{A}_a is an active material. The selected value of $\varepsilon_a^{\mathcal{A}}$ falls within the range commonly used for active components of metamaterials in the visible regime. For example, a mixture of Rhodamine 800 and Rhodamine 6G, yields a relative permittivity with the real part in the range (1.8, 2.3) and the imaginary part in the range $(-0.15, -0.02)$ for the frequency range 440 – 500 THz, depending upon the relative concentrations and the external pumping rate [31]. The volume fraction of component material \mathcal{A}_a was fixed at $f_a^{\mathcal{A}} = 0.3$. Consequently, the Bruggeman equation (2.3.1) delivers the constitutive parameter estimates $\varepsilon^{\mathcal{A}} = 2.6721 - 0.0007i$, $\mu^{\mathcal{A}} = 0.9645 + 0.0001i$, and $\xi^{\mathcal{A}} = 0.0675 + 0.0006i$. Hence, material \mathcal{A} is an isotropic chiral material that simultaneously supports amplification and attenuation of planewave, depending upon the state of circular polarization [25]. Several manifestations of simultaneous amplification and attenuation of planewave have been reported recently [32], including within

the context of surface waves [33, 34].

Let the presentation of numerical results begin with the case where the achiral component material \mathcal{B}_a is specified by the relative permittivity $\varepsilon_a^{\mathcal{B}} = 2 - 0.02di$. Considering $d \in \{-0.2, -0.5, -1\}$ for which component material \mathcal{B}_a is a weakly dissipative dielectric material and $d \in \{0.2, 0.5, 1\}$ for which component material \mathcal{B}_a is an active dielectric material. Estimates of the relative constitutive parameters of material \mathcal{B} , as provided by the Bruggeman equation (2.3.1), are plotted against the volume fraction $f_a^{\mathcal{B}}$ in Fig. 2.2. The $\text{Re}\{\varepsilon^{\mathcal{B}}\}$, $\text{Re}\{\mu^{\mathcal{B}}\}$, and $\text{Re}\{\xi^{\mathcal{B}}\}$ are almost independent of the parameter d ; they vary in an approximately linear manner as $f_a^{\mathcal{B}}$ varies. The $\text{Im}\{\varepsilon^{\mathcal{B}}\}$ is negative-valued for $d > 0$ and positive-valued for $d < 0$. The magnitude $|\text{Im}\{\varepsilon^{\mathcal{B}}\}|$ is larger when the magnitude of d is larger. The imaginary parts of $\mu^{\mathcal{B}}$ and $\xi^{\mathcal{B}}$ are both much less sensitive to d than is $\text{Im}\{\varepsilon^{\mathcal{B}}\}$; both are positive-valued for all values of d and both decay to zero in the limit $f_a^{\mathcal{B}} \rightarrow 1$.

For the canonical problem under consideration, if the dispersion equation (2.2.15) yields a solution then a surface wave is found. Specifically, for $d \in \{-1, -0.5, -0.2, 0.2, 0.5, 1\}$, a surface wave is supported for certain ranges of volume fraction $f_a^{\mathcal{B}}$. The $\text{Re}\{q/k_0\}$ and $\text{Im}\{q/k_0\}$ for these surface waves are plotted against $f_a^{\mathcal{B}}$ in Fig. 2.3. The volume fraction ranges that support surface waves are as follows: $f_a^{\mathcal{B}} \in (0.75, 1]$ for $d = -1$, $f_a^{\mathcal{B}} \in (0.78, 1]$ for $d = -0.5$, $f_a^{\mathcal{B}} \in (0.83, 1]$ for $d = -0.2$, $f_a^{\mathcal{B}} \in (0.90, 1]$ for $d = 0.2$, $f_a^{\mathcal{B}} \in (0.73, 1]$ for $d = 0.5$, and $f_a^{\mathcal{B}} \in (0.70, 1]$ for $d = 1$. Notably, surface waves are not supported at all for small values of $f_a^{\mathcal{B}}$. The real parts of q/k_0 decrease approximately linearly as $f_a^{\mathcal{B}}$ increases, and these values are almost independent of d . The imaginary parts of q/k_0 decrease slightly as $f_a^{\mathcal{B}}$ increases, with the magnitude $|\text{Im}\{q/k_0\}|$ being greater when the magnitude of d is greater. Also $\text{Im}\{q/k_0\} > 0$ when $d < 0$ and $\text{Im}\{q/k_0\} < 0$ when $d > 0$; that is, the surface wave attenuates in the direction of propagation when the component material \mathcal{B}_a is dissipative and the surface wave is amplified in the direction of propagation when the component material \mathcal{B}_a is active.

Further illumination on the nature of these surface waves is offered in Fig. 2.4

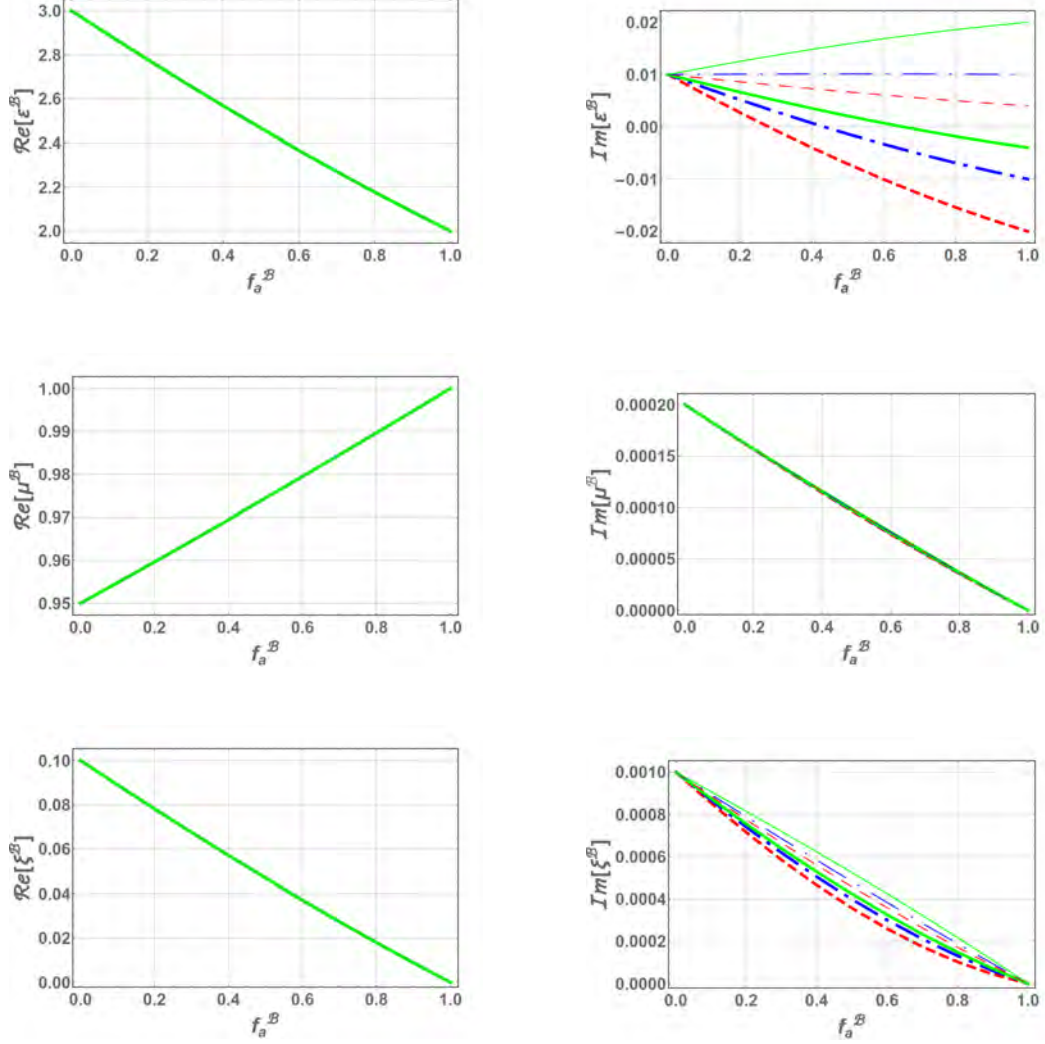


Figure 2.2: Bruggeman estimates of the $\text{Re}\{\cdot\}$ and $\text{Im}\{\cdot\}$ parts of the relative constitutive parameters ε^B , μ^B , and ξ^B plotted against volume fraction f_a^B for $\varepsilon_a^B = 2 - 0.02di$. Key: $d = 1.0$ (thick dashed red curve), 0.5 (thick broken dashed blue curve), 0.2 (thick solid green curve), -0.2 (thin dashed red curve), -0.5 (thin broken dashed blue curve), and -1.0 (thin solid green curve).

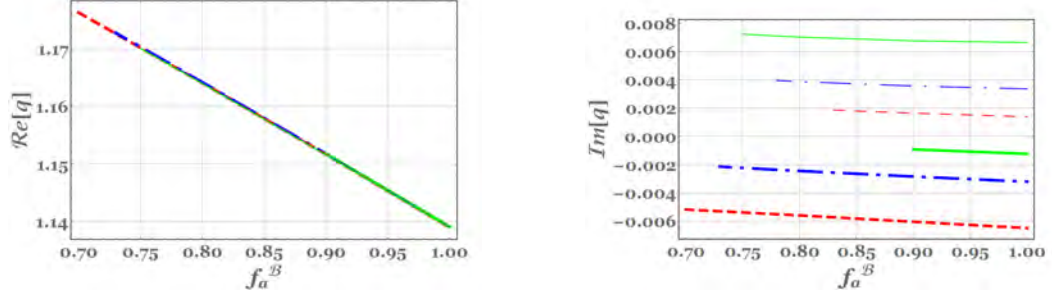


Figure 2.3: $\text{Re}\{\cdot\}$ and $\text{Im}\{\cdot\}$ parts of the relative wavenumber q/k_0 plotted versus volume fraction f_a^B for $\varepsilon_a^B = 2 - 0.02di$. Key: $d = 1.0$ (thick dashed red curve), 0.5 (thick broken dashed blue curve), 0.2 (thick solid green curve), -0.2 (thin dashed red curve), -0.5 (thin broken dashed blue curve), and -1.0 (thin solid green curve).

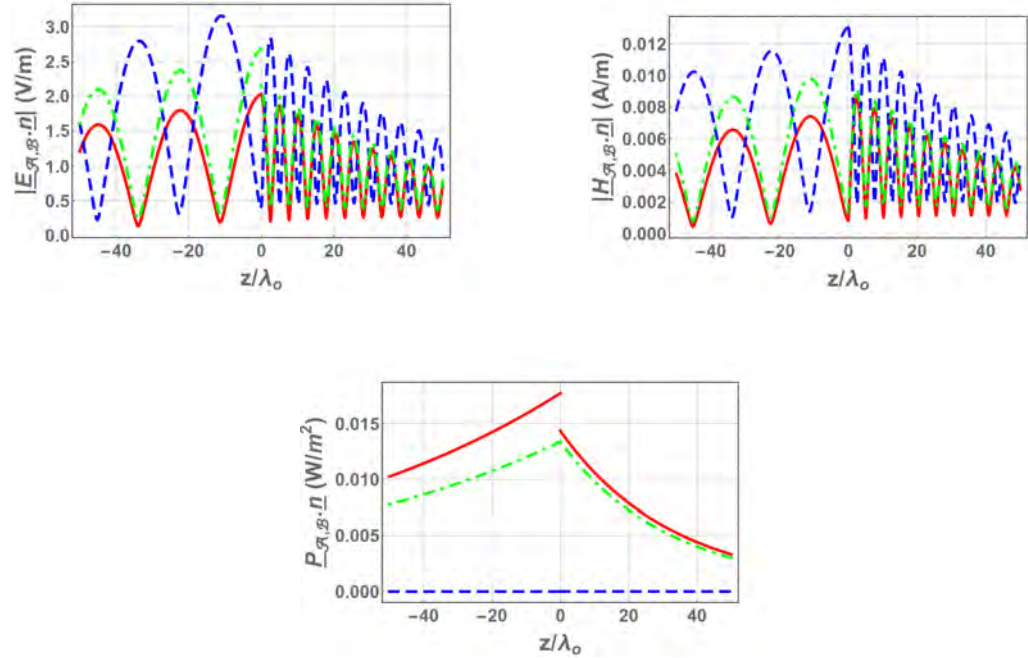


Figure 2.4: Magnitudes of $\underline{E}_{\mathcal{A},\mathcal{B}}(z\hat{u}_z) \cdot \underline{n}$, and $\underline{H}_{\mathcal{A},\mathcal{B}}(z\hat{u}_z) \cdot \underline{n}$, along with $\underline{P}_{\mathcal{A},\mathcal{B}}(z\hat{u}_z) \cdot \underline{n}$, plotted against z/λ_0 , when $\varepsilon_a^B = 2 - 0.02di$, $f_a^B = 0.85$, $d = 0.5$, and $C_{A1} = 1 \text{ Vm}^{-1}$. Key: $\underline{n} = \hat{u}_x$ (solid red curves); $\underline{n} = \hat{u}_y$ (dashed blue curves); $\underline{n} = \hat{u}_z$ (broken dashed green curves).

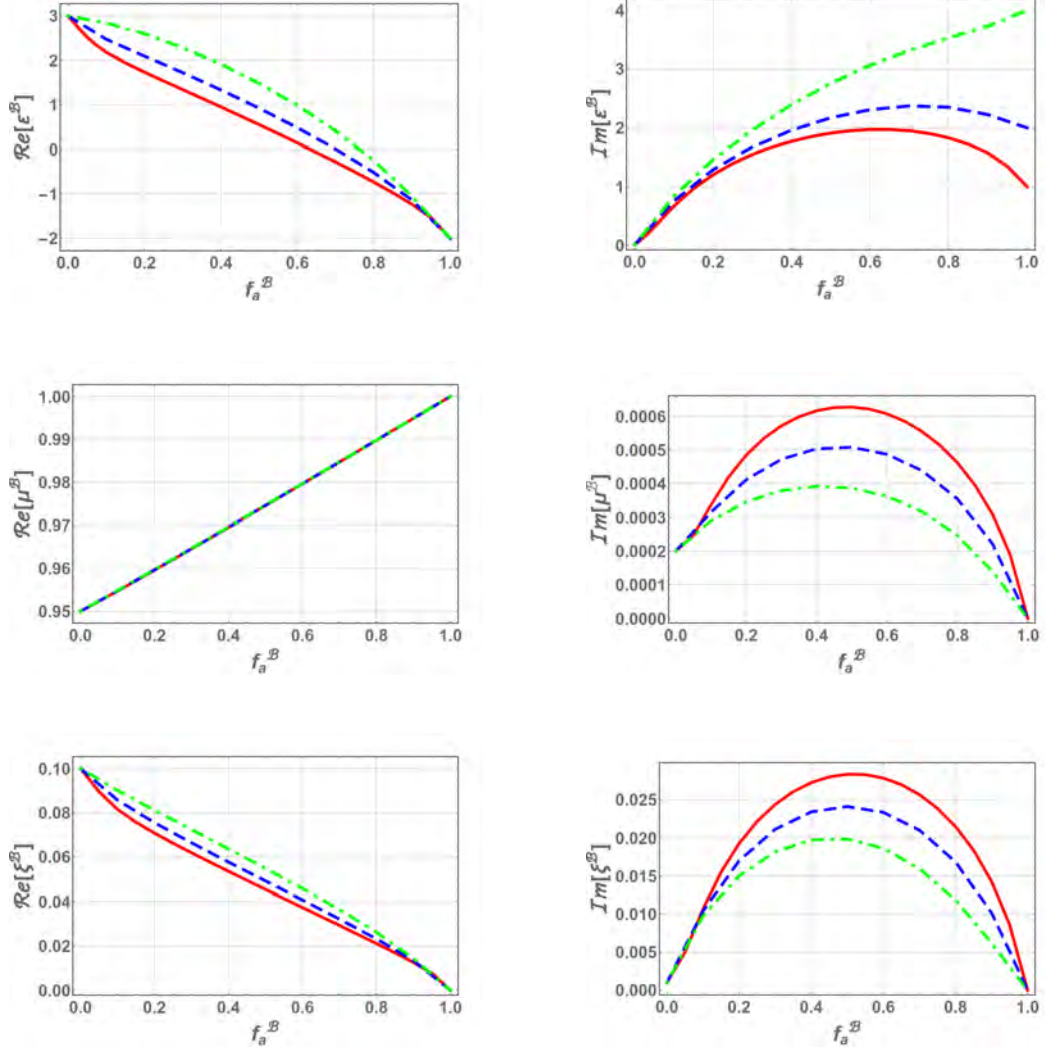


Figure 2.5: Bruggeman estimates of the $\text{Re}\{\cdot\}$ and $\text{Im}\{\cdot\}$ parts of the relative constitutive parameters ε^B , μ^B , and ξ^B plotted against volume fraction f_a^B for $\varepsilon_a^B = -2 + 0.02di$. Key: $d = 50$ (solid red curve), 100 (dashed blue curve), and 200 (broken dashed green curve).

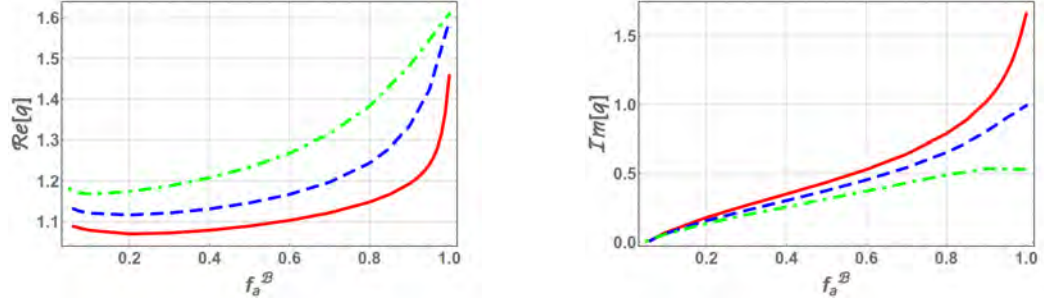


Figure 2.6: $\text{Re}\{\cdot\}$ and $\text{Im}\{\cdot\}$ parts of the relative wavenumber q/k_0 plotted versus volume fraction f_a^B for $\varepsilon_a^B = -2 + 0.02di$. Key: $d = 50$ (solid red curve), 100 (dashed blue curve), and 200 (broken dashed green curve).

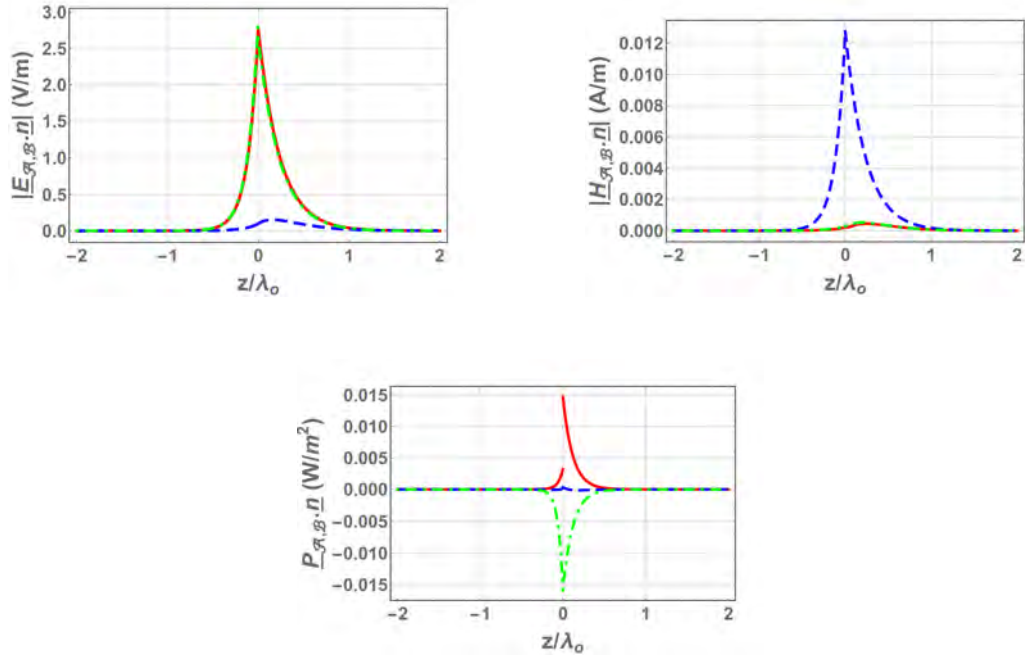


Figure 2.7: Magnitudes of $\underline{E}_{A,B}(z\hat{u}_z) \cdot \underline{n}$, and $\underline{H}_{A,B}(z\hat{u}_z) \cdot \underline{n}$, along with $\underline{P}_{A,B}(z\hat{u}_z) \cdot \underline{n}$, plotted against z/λ_0 , when $\varepsilon_a^B = -2 + 0.02di$, $f_a^B = 0.85$, $d = 100$, and $C_{A1} = 1 \text{ Vm}^{-1}$. Key: $\underline{n} = \hat{u}_x$ (solid red curves); $\underline{n} = \hat{u}_y$ (dashed blue curves); $\underline{n} = \hat{u}_z$ (broken dashed green curves).

wherein variation of the spatial profiles of the electromagnetic field phasors are provided. Specifically, plotted are $|\underline{E}_\ell(z\hat{u}_z) \cdot \underline{n}|$ and $|\underline{H}_\ell(z\hat{u}_z) \cdot \underline{n}|$, $\ell \in \{\mathcal{A}, \mathcal{B}\}$, against z/λ_0 for $\underline{n} \in \{\hat{u}_x, \hat{u}_y, \hat{u}_z\}$, when $d = 0.5$ and $f_a^{\mathcal{B}} = 0.85$, with $C_{\mathcal{A}1} = 1 \text{ V m}^{-1}$. The corresponding variation of the three Cartesian components $\underline{P}_\ell(z\hat{u}_z) \cdot \underline{n}$, $\ell \in \{\mathcal{A}, \mathcal{B}\}$ and $\underline{n} \in \{\hat{u}_x, \hat{u}_y, \hat{u}_z\}$, of the power density (time-averaged Poynting vector) [27] are also plotted using

$$\underline{P}_\ell(\underline{r}) = \frac{1}{2} \text{Re} [\underline{E}_\ell(\underline{r}) \times \underline{H}_\ell^*(\underline{r})], \quad \ell \in \{\mathcal{A}, \mathcal{B}\}, \quad (2.3.4)$$

where the asterisk signifies the complex conjugate. The surface electromagnetic wave is rather loosely confined to the $z = 0$ planar interface, with prominent spreading of the fields into both the half-spaces $z > 0$ and $z < 0$ even at $z = \pm 40\lambda_0$. The surface electromagnetic wave is a little more tightly bound to the planar interface $z = 0$ in the half-space $z > 0$ than in the half-space $z < 0$. Profiles of the field phasors are qualitatively similar for the other values of d considered here.

Next, let me consider the case when the achiral component material \mathcal{B}_a is a plasmonic material. To this end, the relative permittivity $\varepsilon_a^{\mathcal{B}} = -2 + 0.02di$ with $d \in \{50, 100, 200\}$ is selected. In Fig. 2.5, estimates of the relative constitutive parameters of partnering material \mathcal{B} , as provided by the Bruggeman equation (2.3.1), are plotted as functions of volume fraction $f_a^{\mathcal{B}}$. The real parts of $\varepsilon^{\mathcal{B}}$ and $\xi^{\mathcal{B}}$ are generally larger when the parameter d is larger, especially for mid-range values of $f_a^{\mathcal{B}}$, whereas $\text{Re}\{\mu^{\mathcal{B}}\}$ is almost independent of d . The $\text{Im}\{\varepsilon^{\mathcal{B}}\}$ is larger for larger values of d . In contrast, the imaginary parts of $\mu^{\mathcal{B}}$ and $\xi^{\mathcal{B}}$ are larger for smaller values of d and these quantities both decay to zero in the limit $f_a^{\mathcal{B}} \rightarrow 1$.

With the plasmonic component material \mathcal{B}_a and $d \in \{50, 100, 200\}$, a surface wave is supported for wide ranges of volume fraction $f_a^{\mathcal{B}}$, but not for all values of $f_a^{\mathcal{B}}$. The $\text{Re}\{q/k_0\}$ and $\text{Im}\{q/k_0\}$ for these surface waves are plotted against $f_a^{\mathcal{B}}$ in Fig. 2.6. Surface waves are supported for the following ranges of volume fraction: $f_a^{\mathcal{B}} \in (0.06, 1]$ for $d = 50$, $f_a^{\mathcal{B}} \in (0.06, 1]$ for $d = 100$, and $f_a^{\mathcal{B}} \in (0.05, 1]$ for $d = 200$. Notably, surface waves are not supported in the limit $f_a^{\mathcal{B}} \rightarrow 0$. The $\text{Re}\{q/k_0\}$ increases quite sharply as $f_a^{\mathcal{B}}$ increases, depending upon the value d . Likewise, the imaginary parts

of q/k_0 increase as $f_a^{\mathcal{B}}$ increases, with the largest values of $\text{Im}\{q/k_0\}$ arising when the magnitude of d is smallest. Also, for all values of d , $\text{Im}\{q/k_0\} > 0$ which indicates that the surface waves are attenuated in the direction of propagation.

Profiles of the electromagnetic field phasors are presented in Fig. 2.7 for the case where component material \mathcal{B}_a is a plasmonic material, shedding further light on the nature of these surface waves. For these computations, $d = 100$ and $f_a^{\mathcal{B}} = 0.85$, with $C_{A1} = 1 \text{ V m}^{-1}$. The corresponding variation of the three Cartesian components of the power density are also plotted. The surface electromagnetic wave is quite tightly localized to the $z = 0$ planar interface, much more so than the corresponding surface electromagnetic wave represented in Fig. 2.4, with the surface electromagnetic wave being essentially confined to the region $-\lambda_0 < z < \lambda_0$. The surface electromagnetic wave is rather more tightly bound to the $z = 0$ planar interface in the half-space $z < 0$ than in the half-space $z > 0$. Profiles of the field phasors are qualitatively similar for the other values of d considered here.

2.4 Conclusions

The interface of two isotropic chiral materials is shown to support surface-wave propagation for specific constitutive parameter ranges. Surface waves were found only for specific ranges of $f_a^{\mathcal{B}}$. Within these ranges, only one surface wave, identified by its relative wavenumber q/k_0 was supported at each value of $f_a^{\mathcal{B}}$. For $\text{Re}\{\varepsilon_a^{\mathcal{B}}\} > 0$, as $|\text{Im}\{\varepsilon_a^{\mathcal{B}}\}|$ increased, surface waves were found for larger ranges of $f_a^{\mathcal{B}}$, and $|\text{Im}\{q/k_0\}|$ for these surface waves increased. For $\text{Re}\{\varepsilon_a^{\mathcal{B}}\} < 0$, as $\text{Im}\{\varepsilon_a^{\mathcal{B}}\}$ increased, the ranges of $f_a^{\mathcal{B}}$ that supported surface-wave propagation were almost unchanged, but $\text{Im}\{q/k_0\}$ for these surface waves decreased. The surface waves found when $\text{Re}\{\varepsilon_a^{\mathcal{B}}\} < 0$ may be regarded as alike to surface plasmon-polariton (SPP) waves, but those found for when $\text{Re}\{\varepsilon_a^{\mathcal{B}}\} > 0$ may not. When the component material \mathcal{B}_a was a plasmonic material, the surface wave was similar to SPP wave subject to constrain $\text{Re}\{\varepsilon^{\mathcal{A}}\} \times \text{Re}\{\varepsilon^{\mathcal{B}}\} < 0$. But, when the component material \mathcal{B}_a was a dielectric material, the surface wave was not similar to the SPP wave, since $\text{Re}\{\varepsilon^{\mathcal{A}}\} > 0$ and $\text{Re}\{\varepsilon^{\mathcal{B}}\} > 0$. Furthermore, when

the component material \mathcal{B}_a was a dielectric material, the surface wave was not similar to a Dyakonov wave, since both partnering materials were isotropic. These surface waves were not akin to any of the well-established types of surface waves [1]. Moreover, when the component material \mathcal{B}_a was taken as a dissipative dielectric material, the surface waves could be considered similar to the Uller–Zenneck waves.

Slightly magnetic chiral materials were selected for the numerical studies presented in Sec. 2.3. Qualitatively similar results may be obtained when the chiral materials are non-magnetic.

Notably, for all surface-wave solutions reported herein, the constitutive parameters of the materials \mathcal{A} and \mathcal{B} were complex-valued with non-zero imaginary parts. The surface-wave propagation was not found possible for the case in which the constitutive parameters of the materials \mathcal{A} and \mathcal{B} were positive real numbers. This is in line with the fact that the interface of two non-dissipative dielectric materials cannot support surface wave [1].

Parenthetically, the choice of complex-valued constitutive parameters (with non-zero imaginary parts) for the chiral partnering materials was not a matter of convenience. Since optical rotation and circular dichroism were related via the Kramers–Kronig relations [35, 36], complex-valued constitutive parameters were essential for the sake of realism.

References

- [1] J. A. Polo Jr., T. G. Mackay, and A. Lakhtakia, *Electromagnetic Surface Waves: A Modern Perspective*, Elsevier (2013).
- [2] J. M. Pitarke, V. M. Silkin, E. V. Chulkov, and P. M. Echenique, “Theory of surface plasmon and surface-plasmon polaritons,” *Rep. Prog. Phys.* **70**, 1–87 (2007).
- [3] S. A. Maier, *Plasmonics: Fundamentals and Applications*, Springer (2007).
- [4] Z. Jacob and E. E. Narimanov, “Optical hyperspace for plasmons: Dyakonov states in metamaterials,” *Appl. Phys. Lett.* **93**, 221109 (2008).
- [5] J. Homola (Ed.), *Surface Plasmon Resonance Based Sensors*, Springer (2006).
- [6] I. Abdulhalim, M. Zourob, and A. Lakhtakia, “Surface plasmon resonance for biosensing: A mini-review,” *Electromagnetics* **28**, 214–242 (2008).
- [7] F. N. Marchevskii, V. L. Strizhevskii, and S. V. Strizhevskii, “Singular electromagnetic waves in bounded anisotropic media,” *Sov. Phys. Solid State* **26**, 911–912 (1984).
- [8] M. I. D’yakonov, “New type of electromagnetic wave propagating at an interface,” *Sov. Phys. JETP* **67**, 714–716 (1988).
- [9] D. B. Walker, E. N. Glytsis, and T. K. Gaylord, “Surface mode at isotropic-uniaxial and isotropic-biaxial interfaces,” *J. Opt. Soc. Am. A* **15**, 248–260 (1998).

- [10] O. Takayama, L.-C. Crasovan, D. Artigas, and L. Torner, “Observation of Dyakonov surface waves,” *Phys. Rev. Lett.* **102**, 043903 (2009).
- [11] O. Takayama, L.-C. Crasovan, S. K. Johansen, D. Mihalache, D. Artigas, and L. Torner, “Dyakonov surface waves: A review,” *Electromagnetics* **28**, 126–145 (2008).
- [12] T. G. Mackay and A. Lakhtakia, “Temperature-mediated transition from Dyakonov surface waves to surface-plasmon-polariton waves,” *IEEE Photon. J.* **8**, 4802813 (2016).
- [13] M. Faryad and F. Abbas, “On the Dyakonov waves guided by the interface with a columnar thin film,” in: 12th International Congress on Artificial Materials for Novel Wave Phenomena (Metamaterials), *Proc. IEEE.*, (2018).
- [14] L.-C. Crasovan, D. Artigas, D. Mihalache, and L. Torner, “Optical Dyakonov surface waves at magnetic interfaces,” *Opt. Lett.* **30**, 3075–3077 (2005).
- [15] L.-C. Crasovan, O. Takayama, D. Artigas, S. K. Johansen, D. Mihalache, and L. Torner, “Enhanced localization of Dyakonov-like surface waves in left-handed materials,” *Phys. Rev. B* **74**, 155120 (2006).
- [16] O. Takayama, E. Shkondin, A. Bodganov, M. E. A. Panah, K. Golenitskii, P. Dmitriev, T. Repan, R. Malureanu, P. Belov, F. Jensen, and A. V. Lavrinenko, “Midinfrared surface waves on a high aspect ratio nanotrench platform,” *ACS Photonics* **4**, 2899–2907 (2017).
- [17] P. Li, I. Dolado, F. J. Alfaro-Mozaz, F. Casanova, L. E. Hueso, S. Liu, J. H. Edgar, A. Y. Nikitin, S. Vélez, and R. Hillenbrand, “Infrared hyperbolic metasurface based on nanostructured van der Waals materials,” *Science* **359**, 892–896 (2018).
- [18] A. Lakhtakia, *Beltrami Fields in Chiral Media*, World Scientific (1994).

- [19] D. N. Pattanayak and J. L. Birman, “Wave propagation in optically active and magnetoelectric media of arbitrary geometry,” *Phys. Rev. B* **24**, 4271–4278 (1981).
- [20] N. Engheta and P. Pelet, “Surface waves in chiral layers,” *Opt. Lett.* **16**, 723–725 (1991).
- [21] A. N. Fantino, “Planar interface between a chiral medium and a metal: surface wave excitation,” *J. Mod. Opt.* **43**, 2581–2593 (1996).
- [22] G. Pellegrini, M. Finazzi, M. Celebrano, L. Duò, and P. Biagioni, “Chiral surface waves for enhanced circular dichroism,” *Phys. Rev. B* **95**, 241402 (2017).
- [23] J. Noonan and T. G. Mackay, “On electromagnetic surface waves supported by an isotropic chiral material,” *Opt. Commun.* **434**, 224–229 (2019).
- [24] T. G. Mackay and A. Lakhtakia, *Modern Analytical Electromagnetic Homogenization*, Morgan & Claypool (2015).
- [25] T. G. Mackay and A. Lakhtakia, “Simultaneous amplification and attenuation in isotropic chiral materials,” *J. Opt. (UK)* **18**, 055104 (2016).
- [26] B. Y.-K. Hu, “Kramers–Kronig in two lines,” *Am. J. Phys.* **57**, 821 (1989).
- [27] H. C. Chen, *Theory of Electromagnetic Waves*, McGraw–Hill (1983).
- [28] Y. Jaluria, *Computer Methods for Engineering*, Taylor & Francis (1996).
- [29] R. D. Kampia and A. Lakhtakia, “Bruggeman model for chiral particulate composites,” *J. Phys. D: Appl. Phys.* **25**, 1390–1394 (1992).
- [30] D.-H. Kwon, D. H. Werner, A. V. Kildishev, and V. M. Shalaev, “Material parameter retrieval procedure for general bi-isotropic metamaterials and its application to optical chiral negative-index metamaterial design,” *Opt. Exp.* **16**, 11822–11829 (2008).

- [31] L. Sun, X. Yang, and J. Gao, “Loss-compensated broadband epsilon-near-zero metamaterials with gain media,” *Appl. Phys. Lett.* **103**, 201109 (2013).
- [32] T. G. Mackay and A. Lakhtakia, “Dynamically controllable anisotropic metamaterials with simultaneous attenuation and amplification,” *Phys. Rev. A* **92**, 053847 (2015).
- [33] T. G. Mackay and A. Lakhtakia, “Simultaneous existence of amplified and attenuated surface-plasmon-polariton waves,” *J. Opt. (India)* **47**, 527–533 (2018).
- [34] T. G. Mackay and A. Lakhtakia, “Simultaneous existence of amplified and attenuated Dyakonov surface waves,” *Opt. Commun.* **427**, 175–179 (2018).
- [35] C. A. Emeis, L. J. Oosterhoff, and G. de Vries, “Numerical evaluation of Kramers-Kronig relations,” *Proc. Royal Soc. Lond. A* **297**, 54–65 (1967).
- [36] A. Lakhtakia, “Comment on ‘Accelerated particle radiation in chiral media’,” *J. Appl. Phys.* **71**, 3059–3060 (1992).

Chapter 3

Metal and Isotropic Chiral Medium

In this chapter, the SPP-waves excitation at the interface of an isotropic chiral material and a plasmonic material is investigated in the practical setups of prism couplings. The characteristics of the SPP waves in both the TKR and the Turbadar–Otto configurations are studied. The associated canonical problem is also solved numerically for the confirmation of the findings of the prism-coupled configurations.

Chapter 3 is planned as follows: The introduction and related literature review is given in Sec. 3.1. The theoretical formulation of the canonical problem is presented in Sec. 3.3. The theoretical formulation of the prism coupling technique is presented in Sec. 3.2. The numerical results of the canonical problem and the prism couplings for the SPP-waves excitation are presented and discussed in Sec. 3.4. The conclusions are given in Sec. 3.5.

3.1 Introduction

Most of the applications of the SPP waves use isotropic dielectric material as partnering material with a plasmonic material. However, the scope for the applications of the SPP waves can be increased by using complex chiral materials [1]. Hence, the SPP waves have also been investigated with partnering material taken as isotropic

The work reported in this chapter is published in: *Eur. Phys. J. Plus* **135**, 724 (2020).

chiral materials [2] or isotropic homogenized composite chiral materials [3–6]. The isotropic chiral materials are made by randomly suspending nano helixes in a host dielectric material where the period of the suspended nano helixes should be smaller than one-tenth of the operating wavelength of the electromagnetic wave [7, 8]. For example, isotropic chiral materials, such as glucose and aspartame, can be made by mixing chiral molecules in an isotropic host medium, such as water. These isotropic chiral materials can be used to design other metamaterials also [9].

The chiral materials offer phenomenologically richer characteristics for surface-wave propagation than achiral materials due to their intrinsic magneto-electric coupling. The isotropic chiral materials are known as optically active materials because of their gyrotropic properties owing to the magneto-electric coupling [10–12]. Therefore, they have potential applications in coupling devices [11, 13] and have potential usage in directional couplers, switches, chirostrip antennas [14], chirowaveguides [11, 12, 15], integrated optical devices and advanced radar technology [16]. Zhang and Li investigated the properties of the SPP-waves-based waveguiding structure using asymmetric chiral-metal-chiral layers that are exploited for stronger confinement and enhanced propagation of light. Thus, these materials open up new possibilities in the development of cutoff-based mode-selective waveguides. The cutoffs that exist for the chiral-metal-chiral structures enable the possibility of new features for nanophotonic devices [17]. Similar work on the exploration of the properties of the SPP waves for enhanced propagation and better cutoff frequency but based on metal-chiral-metal plasmonic waveguide is presented in [18]. These materials also support hybrid modes. [1, 11]. Recently, hybrid surface-wave propagation has been studied using chiral metamaterials [19, 20]. Gyrotropic effects such as the circular dichroism, the optical rotation, and the circular birefringence are exhibited by isotropic chiral medium [21]. The characteristics of the SPP waves, such as the propagation length and the dependence on the cutoff frequency and chirality parameter at a chiral-metal surface, are studied in [22] for enantiomeric detection and on-chip chiral sensing. Another interesting application of plasmonics is reported in [23, 24] for the separation

of chiral enantiomers and biomolecules and their manipulation using lateral optical force and torque induced by the quantum spin Hall effect of light.

The propagation of surface waves along the interface of a chiral medium and a plasmonic material has already been investigated theoretically in the canonical problem by Fantino in 1996 [25]. However, the canonical problem can not be implemented experimentally since the partnering materials fill up the half spaces. For experimental implementation, the prism coupling is the simple technique to couple the incident light with the SPP waves. Since there are two types of prism coupling techniques, I have investigated both types of prism-coupled configurations to see if the SPP waves can be excited using isotropic chiral materials.

3.2 Theory of Prism-Coupled Configurations

Consider the geometry of the problem as presented in Fig. 3.1. The half-space $z \leq 0$ is the incidence half-space filled up by an unbounded isotropic homogeneous dielectric material (prism) with refractive index n_p . The region $0 \leq z \leq L_A$ is occupied by the isotropic homogeneous material \mathcal{A} . The region $L_A \leq z \leq L_\Sigma = L_A + L_B$ is occupied by another isotropic homogeneous material \mathcal{B} and the half-space $z \geq L_\Sigma$ is the transmission half-space filled up by an unbounded isotropic homogeneous dielectric material with refractive index n_t .

The isotropic homogeneous chiral material is characterized by Tellegen constitutive relations in the frequency-domain [8],

$$\left. \begin{aligned} \underline{D}(\underline{r}, \omega) &= \varepsilon_0 \varepsilon(z) \underline{E}(\underline{r}, \omega) + i \sqrt{\varepsilon_0 \mu_0} \xi(z) \underline{H}(\underline{r}, \omega) \\ \underline{B}(\underline{r}, \omega) &= -i \sqrt{\varepsilon_0 \mu_0} \xi(z) \underline{E}(\underline{r}, \omega) + \mu_0 \mu(z) \underline{H}(\underline{r}, \omega) \end{aligned} \right\}, \quad (3.2.1)$$

where

$$\varepsilon(z) = \begin{cases} \varepsilon^{\mathcal{A}}, & 0 \leq z \leq L_A \\ \varepsilon^{\mathcal{B}}, & L_A \leq z \leq L_A + L_B \end{cases}, \quad (3.2.2)$$

is the relative permittivity,

$$\mu(z) = \begin{cases} \mu^A, & 0 \leq z \leq L_A \\ \mu^B, & L_A \leq z \leq L_A + L_B \end{cases}, \quad (3.2.3)$$

is the relative permeability, and

$$\xi(z) = \begin{cases} \xi^A, & 0 \leq z \leq L_A \\ \xi^B, & L_A \leq z \leq L_A + L_B \end{cases}, \quad (3.2.4)$$

is the relative chirality pseudoscalar. The relative constitutive parameters $\varepsilon(z)$,

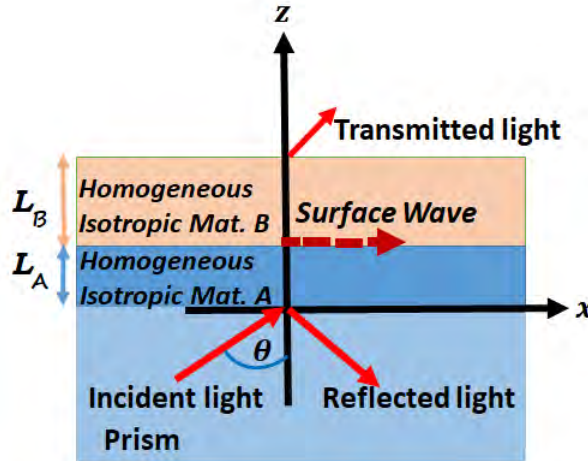


Figure 3.1: A general schematic for the SPP-waves excitation at the interface of two different homogeneous isotropic media is shown representing the prism coupling.

$\mu(z)$, and $\xi(z)$ are complex-valued. Also, these parameters are frequency dependent per the causality principle represented by the Kramers–Kronig relations [26–28]. The isotropic homogeneous chiral material is characterized by these constitutive parameters. However, when the homogeneous isotropic material is considered as a non-magnetic plasmonic material, it is specified only by its complex-valued relative permittivity with negative real-valued part, and the constitutive relations assume the

following form in the frequency-domain,

$$\left. \begin{aligned} \underline{D}(\underline{r}, \omega) &= \varepsilon_0 \varepsilon_{met}(z) \underline{E}(\underline{r}, \omega) \\ \underline{B}(\underline{r}, \omega) &= \mu_0 \underline{H}(\underline{r}, \omega) \end{aligned} \right\}, \quad (3.2.5)$$

where $\varepsilon_{met}(z)$ is the relative permittivity characterizing the non-magnetic plasmonic medium.

In the TKR configuration, material \mathcal{A} is a plasmonic material, and material \mathcal{B} is an isotropic chiral material. In the Turbadar–Otto configuration, the role of these materials is interchanged. Therefore, the formulation provided in this section can be used for both prism coupling techniques by appropriately selecting the materials.

Let me consider an electromagnetic wave propagating in the half-space $z \leq 0$ and making an angle $\theta \in [0, \pi/2)$ with the z axis in the xz plane, be incident at the interface $z = 0$. This will excite the SPP wave propagating parallel to \hat{u}_x in the xy plane. The incident, reflected, and the transmitted electric field phasors of the electromagnetic waves can be written as

$$\left. \begin{aligned} \underline{E}_{inc}(\underline{r}) &= \left(a_s \hat{u}_y + a_p \underline{p}_+ \right) \exp[i(x\kappa + zk_0 n_p \cos \theta)], z \leq 0 \\ \underline{E}_{ref}(\underline{r}) &= \left(r_s \hat{u}_y + r_p \underline{p}_- \right) \exp[i(x\kappa - zk_0 n_p \cos \theta)], z \leq 0 \\ \underline{E}_{tr}(\underline{r}) &= \left(t_s \hat{u}_y + t_p \underline{p}_t \right) \exp[i(x\kappa + k_0 n_t \cos \theta_t(z - L_\Sigma))], z \geq L_\Sigma \end{aligned} \right\}, \quad (3.2.6)$$

where $\kappa = k_0 n_p \sin \theta$, $L_\Sigma = L_{\mathcal{A}} + L_{\mathcal{B}}$, $\underline{p}_+ = -\hat{u}_x \cos \theta + \hat{u}_z \sin \theta$, $\underline{p}_- = \hat{u}_x \cos \theta + \hat{u}_z \sin \theta$, $\underline{p}_t = -\hat{u}_x \cos \theta_t + \hat{u}_z \sin \theta_t$, where

$$\theta_t = \sin^{-1}\left(\frac{n_p}{n_t} \sin \theta\right) \quad (3.2.7)$$

is the transmission angle; a_s and a_p represent the scalar amplitudes of the s - and p -polarized electromagnetic waves, respectively. Similarly, r_s and r_p are the reflection coefficients and the transmission coefficients are denoted by t_s and t_p . The corresponding incident, reflected, and the transmitted magnetic field phasors of a planewave are

derived from Maxwell's curl postulates as follows

$$\left. \begin{aligned} \underline{H}_{inc}(\underline{r}) &= \frac{n_p}{\eta_0} \left(a_s \underline{p}_+ - a_p \hat{u}_y \right) \exp[i(x\kappa + zk_0 n_p \cos \theta)], z \leq 0 \\ \underline{H}_{ref}(\underline{r}) &= \frac{n_p}{\eta_0} \left(r_s \underline{p}_- - r_p \hat{u}_y \right) \exp[i(x\kappa - zk_0 n_p \cos \theta)], z \leq 0 \\ \underline{H}_{tr}(\underline{r}) &= \frac{n_t}{\eta_0} \left(t_s \underline{p}_t - t_p \hat{u}_y \right) \exp[i(x\kappa + k_0 n_t \cos \theta_t(z - L_\Sigma))], z \geq L_\Sigma \end{aligned} \right\}. \quad (3.2.8)$$

The electromagnetic field phasors in both materials can be written as

$$\left. \begin{aligned} \underline{E}(\underline{r}) &= [e_x(z)\hat{u}_x + e_y(z)\hat{u}_y + e_z(z)\hat{u}_z] \exp(i\kappa x) \\ \underline{H}(\underline{r}) &= [h_x(z)\hat{u}_x + h_y(z)\hat{u}_y + h_z(z)\hat{u}_z] \exp(i\kappa x) \end{aligned} \right\}. \quad (3.2.9)$$

Substitution of Eqs. (3.2.5) and (3.2.9) in Maxwell curl postulates, i.e.,

$$\left. \begin{aligned} \nabla \times \underline{E}(\underline{r}, \omega) &= i\omega \underline{B}(\underline{r}, \omega) \\ \nabla \times \underline{H}(\underline{r}, \omega) &= -i\omega \underline{D}(\underline{r}, \omega) \end{aligned} \right\}, \quad (3.2.10)$$

results in the two algebraic equations for a plasmonic medium as follows,

$$\left. \begin{aligned} e_{zm}(z) &= -\frac{\kappa}{\omega \varepsilon_0 \varepsilon_{met}} h_y(z) \\ h_{zm}(z) &= \frac{\kappa}{\omega \mu_0} e_y(z) \end{aligned} \right\}, \quad (3.2.11)$$

and four partial differential equations are also obtained, which can be re-arranged as the matrix ordinary differential equation

$$\frac{d}{dz} [\underline{f}(z)] = i[\underline{P}_{met}] \cdot [\underline{f}(z)], \quad (3.2.12)$$

where

$$[\underline{f}(z)] = \begin{bmatrix} e_x(z) \\ e_y(z) \\ h_x(z) \\ h_y(z) \end{bmatrix} \quad (3.2.13)$$

and

$$\begin{aligned}
 [\underline{\underline{P}}_{met}] &= \omega \begin{bmatrix} 0 & 0 & 0 & \mu_0 \\ 0 & 0 & -\mu_0 & 0 \\ 0 & -\varepsilon_0 \varepsilon_{met} & 0 & 0 \\ \varepsilon_0 \varepsilon_{met} & 0 & 0 & 0 \end{bmatrix} \\
 &+ \frac{\kappa^2}{\omega \mu_0 \varepsilon_0 \varepsilon_{met}} \begin{bmatrix} 0 & 0 & 0 & -\mu_0 \\ 0 & 0 & 0 & 0 \\ 0 & \varepsilon_0 \varepsilon_{met} & 0 & 0 \\ 0 & 0 & 0 & 0 \end{bmatrix}. \tag{3.2.14}
 \end{aligned}$$

Substitution of Eqs. (3.2.1) and (3.2.9) in Maxwell curl postulates, for a homogeneous isotropic chiral medium gives

$$\frac{d}{dz}[\underline{f}(z)] = i[\underline{\underline{P}}_{ch}] \cdot [\underline{f}(z)], \tag{3.2.15}$$

with

$$\begin{aligned}
[\underline{P}_{ch}] &= k_0 \begin{bmatrix} 0 & -i\xi & 0 & 0 \\ i\xi & 0 & 0 & 0 \\ 0 & 0 & 0 & -i\xi \\ 0 & 0 & i\xi & 0 \end{bmatrix} \\
&+ \omega \begin{bmatrix} 0 & 0 & 0 & \mu_0\mu \\ 0 & 0 & -\mu_0\mu & 0 \\ 0 & -\varepsilon_0\varepsilon & 0 & 0 \\ \varepsilon_0\varepsilon & 0 & 0 & 0 \end{bmatrix} \\
&+ \frac{\kappa^2}{\omega\sqrt{\mu_0\varepsilon_0}[\varepsilon\mu - \xi^2]} \begin{bmatrix} 0 & -i\xi & 0 & 0 \\ 0 & 0 & 0 & 0 \\ 0 & 0 & 0 & -i\xi \\ 0 & 0 & 0 & 0 \end{bmatrix} \\
&+ \frac{\kappa^2}{\omega\mu_0\varepsilon_0[\varepsilon\mu - \xi^2]} \begin{bmatrix} 0 & 0 & 0 & -\mu_0\mu \\ 0 & 0 & 0 & 0 \\ 0 & \varepsilon_0\varepsilon & 0 & 0 \\ 0 & 0 & 0 & 0 \end{bmatrix}, \tag{3.2.16}
\end{aligned}$$

and the two algebraic equations are obtained as follows,

$$\left. \begin{aligned} e_z(z) &= \frac{\mu\kappa}{\omega\varepsilon_0[\xi^2 - \varepsilon\mu]} h_y(z) + \frac{i\kappa\xi}{k_0[\xi^2 - \varepsilon\mu]} e_y(z) \\ h_z(z) &= -\frac{\varepsilon\kappa}{\omega\mu_0[\xi^2 - \varepsilon\mu]} e_y(z) + \frac{i\kappa\xi}{k_0[\xi^2 - \varepsilon\mu]} h_y(z) \end{aligned} \right\}. \tag{3.2.17}$$

The incident and reflected electric field phasors (3.2.6) and the corresponding

magnetic field phasors (3.2.8) give $[f(0-)] = [\underline{K}_{inc}] \cdot [a_s \ a_p \ r_s \ r_p]^T$, where

$$[\underline{K}_{inc}] = \begin{bmatrix} 0 & -\cos \theta & 0 & \cos \theta \\ 1 & 0 & 1 & 0 \\ -\frac{n_p}{\eta_0} \cos \theta & 0 & \frac{n_p}{\eta_0} \cos \theta & 0 \\ 0 & -\frac{n_p}{\eta_0} & 0 & -\frac{n_p}{\eta_0} \end{bmatrix}. \quad (3.2.18)$$

Similarly, the transmitted electric and magnetic field phasors give $[f(L_\Sigma+)] = [\underline{K}_{tr}] \cdot [t_s \ t_p \ 0 \ 0]^T$, where

$$[\underline{K}_{tr}] = \begin{bmatrix} 0 & -\cos \theta_t & 0 & \cos \theta_t \\ 1 & 0 & 1 & 0 \\ -\frac{n_t}{\eta_0} \cos \theta_t & 0 & \frac{n_t}{\eta_0} \cos \theta_t & 0 \\ 0 & -\frac{n_t}{\eta_0} & 0 & -\frac{n_t}{\eta_0} \end{bmatrix}. \quad (3.2.19)$$

At the same time, the solution of the MODE (3.2.12) gives,

$$[f(L_\Sigma-)] = e^{i[\underline{P}_{\mathcal{B}}]L_{\mathcal{B}}} \cdot e^{i[\underline{P}_{\mathcal{A}}]L_{\mathcal{A}}} \cdot [f(0+)] \quad (3.2.20)$$

where $[\underline{P}_{\mathcal{A}}]$ is the $[\underline{P}(z)]$ matrix for material \mathcal{A} and $[\underline{P}_{\mathcal{B}}]$ is the $[\underline{P}(z)]$ matrix for material \mathcal{B} .

Using the standard boundary conditions [29]

$$\left. \begin{aligned} [f(0-)] &= [f(0+)] \\ [f(L_{\mathcal{A}}-)] &= [f(L_{\mathcal{A}}+)] \\ [f(L_\Sigma-)] &= [f(L_\Sigma+)] \end{aligned} \right\} \quad (3.2.21)$$

gives

$$\begin{bmatrix} t_s \\ t_p \\ 0 \\ 0 \end{bmatrix} = [\underline{K}_{tr}]^{-1} \cdot e^{i[\underline{P}_{\mathcal{B}}]L_{\mathcal{B}}} \cdot e^{i[\underline{P}_{\mathcal{A}}]L_{\mathcal{A}}} \cdot [\underline{K}_{inc}] \cdot \begin{bmatrix} a_s \\ a_p \\ r_s \\ r_p \end{bmatrix}. \quad (3.2.22)$$

To find the reflection and transmission coefficients, Eq. (3.2.22) can be written as

$$\begin{bmatrix} t_s \\ t_p \\ 0 \\ 0 \end{bmatrix} = [\underline{\underline{M}}] \cdot \begin{bmatrix} a_s \\ a_p \\ r_s \\ r_p \end{bmatrix}, \quad (3.2.23)$$

where

$$\begin{aligned} [\underline{\underline{M}}] &= [\underline{\underline{K}}_{tr}]^{-1} \cdot e^{i[\underline{\underline{P}}_B]L_B} \cdot e^{i[\underline{\underline{P}}_A]L_A} \cdot [\underline{\underline{K}}_{inc}] \\ &= \begin{bmatrix} m_{11} & m_{12} & m_{13} & m_{14} \\ m_{21} & m_{22} & m_{23} & m_{24} \\ m_{31} & m_{32} & m_{33} & m_{34} \\ m_{41} & m_{42} & m_{43} & m_{44} \end{bmatrix}. \end{aligned} \quad (3.2.24)$$

Therefore, using the bottom two rows of Eq. (3.2.23), I get

$$\begin{bmatrix} r_s \\ r_p \end{bmatrix} = - \begin{bmatrix} m_{33} & m_{34} \\ m_{43} & m_{44} \end{bmatrix}^{-1} \cdot \begin{bmatrix} m_{31} & m_{32} \\ m_{41} & m_{42} \end{bmatrix} \cdot \begin{bmatrix} a_s \\ a_p \end{bmatrix}. \quad (3.2.25)$$

After finding the reflection amplitudes from Eq. (3.2.25), the transmission amplitudes can be obtained from the top two rows of Eq. (3.2.22).

The absorptances can then be determined with the help of the reflection and transmission amplitudes by using [30]

$$A_s = 1 - \frac{|r_s|^2 + |r_p|^2 + (|t_s|^2 + |t_p|^2)F}{|a_s|^2}, a_p = 0, \quad (3.2.26)$$

for s -polarized incident light, and

$$A_p = 1 - \frac{|r_s|^2 + |r_p|^2 + (|t_s|^2 + |t_p|^2)F}{|a_p|^2}, a_s = 0, \quad (3.2.27)$$

for p -polarized incident light, where

$$F = \frac{\text{Re}[n_t \cos \theta_t]}{n_p \cos \theta}. \quad (3.2.28)$$

3.3 Theory of Canonical Problem

In Chap. 2, the formulation of the canonical problem was presented for the two homogeneous isotropic chiral half-spaces. However, in this section, the formulation of the canonical problem is presented for two isotropic homogeneous materials, of which one is a plasmonic material and the other is an isotropic chiral material. Figure 3.2 shows the schematic of the canonical problem. Let the half-space $z \leq 0$ be filled up by the isotropic and homogeneous plasmonic material characterized by the relative permittivity ε_{met} which is complex-valued. The half-space $z \geq 0$ is filled up by the isotropic homogeneous chiral material. Without loss of generality, the SPP-wave

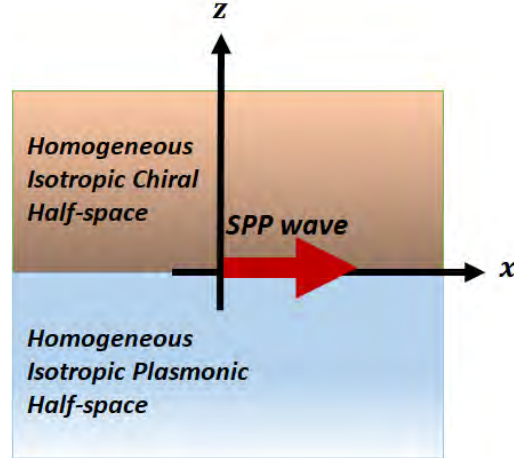


Figure 3.2: A general schematic for the SPP-waves propagation along the interface of two different isotropic homogeneous half-spaces is shown.

propagation is along the x -axis propagating along the planar interface $z = 0$, and

attenuates as $z \rightarrow \pm\infty$. Therefore, in the region $z \leq 0$, the wave vector can be written as

$$\underline{k}_{met} = q\hat{u}_x - \alpha_{met}\hat{u}_z \quad (3.3.1)$$

where $q^2 + \alpha_{met}^2 = k_0^2 \varepsilon_{met}$, q is complex-valued, and $\text{Im}(\alpha_{met}) > 0$ for attenuation as $z \rightarrow -\infty$. Correspondingly, the field phasors in the plasmonic half-space can be represented as,

$$\underline{E}(\underline{r}) = \left[a_p \left(\frac{\alpha_{met}}{k_0} \hat{u}_x + \frac{q}{k_0} \hat{u}_z \right) + a_s \hat{u}_y \right] \exp(i \underline{k}_{met} \cdot \underline{r}), \quad z \leq 0, \quad (3.3.2)$$

and

$$\underline{H}(\underline{r}) = \eta_0^{-1} \left[a_s \left(\frac{\alpha_{met}}{k_0} \hat{u}_x + \frac{q}{k_0} \hat{u}_z \right) - a_p \varepsilon_{met} \hat{u}_y \right] \exp(i \underline{k}_{met} \cdot \underline{r}), \quad z \leq 0, \quad (3.3.3)$$

where the subscripts s and p represent the s - (perpendicular-) and p - (parallel-) polarization states with respect to the xz plane, respectively. Here a_s and a_p are unknown scalars.

The electromagnetic field phasors in the half-space $z > 0$ is given as $\underline{E}(\underline{r}) = \underline{e}(z) \exp(i \kappa x)$ and $\underline{H}(\underline{r}) = \underline{h}(z) \exp(i \kappa x)$ where $\underline{e}(z) = e_x(z)\hat{u}_x + e_y(z)\hat{u}_y + e_z(z)\hat{u}_z$ and $\underline{h}(z) = h_x(z)\hat{u}_x + h_y(z)\hat{u}_y + h_z(z)\hat{u}_z$. The components $e_z(z)$ and $h_z(z)$ of the electromagnetic field phasors can be obtained in terms of the other two components as follows,

$$\left. \begin{aligned} e_z(z) &= \frac{\mu^B \kappa}{\omega \varepsilon_0 [(\xi^B)^2 - \varepsilon^B \mu^B]} h_y(z) + \frac{i \kappa \xi^B}{k_0 [(\xi^B)^2 - \varepsilon^B \mu^B]} e_y(z), & z > 0 \\ h_z(z) &= -\frac{\varepsilon^B \kappa}{\omega \mu_0 [(\xi^B)^2 - \varepsilon^B \mu^B]} e_y(z) + \frac{i \kappa \xi^B}{k_0 [(\xi^B)^2 - \varepsilon^B \mu^B]} h_y(z), & z > 0 \end{aligned} \right\}, \quad (3.3.4)$$

where ε^B is the relative permittivity, μ^B is the relative permeability, and ξ^B represents the relative chirality pseudoscalar of the isotropic chiral material. The other two components of electromagnetic field phasors can be expressed in vector form as,

$$[\underline{f}(z)] = \begin{bmatrix} e_x(z) \\ e_y(z) \\ h_x(z) \\ h_y(z) \end{bmatrix} \quad (3.3.5)$$

which satisfies the matrix ordinary differential equation as,

$$\frac{d}{dz}[\underline{f}(z)] = i[\underline{P}_{\underline{\underline{B}}}] \cdot [\underline{f}(z)], \quad z > 0, \quad (3.3.6)$$

where 4×4 matrix

$$\begin{aligned} [\underline{P}_{\underline{\underline{B}}}] &= k_0 \begin{bmatrix} 0 & -i\xi^{\mathcal{B}} & 0 & 0 \\ i\xi^{\mathcal{B}} & 0 & 0 & 0 \\ 0 & 0 & 0 & -i\xi^{\mathcal{B}} \\ 0 & 0 & i\xi^{\mathcal{B}} & 0 \end{bmatrix} \\ &+ \omega \begin{bmatrix} 0 & 0 & 0 & \mu_0 \mu^{\mathcal{B}} \\ 0 & 0 & -\mu_0 \mu^{\mathcal{B}} & 0 \\ 0 & -\varepsilon_0 \varepsilon^{\mathcal{B}} & 0 & 0 \\ \varepsilon_0 \varepsilon^{\mathcal{B}} & 0 & 0 & 0 \end{bmatrix} \\ &+ \frac{\kappa^2}{\omega \sqrt{\mu_0 \varepsilon_0} [\varepsilon^{\mathcal{B}} \mu^{\mathcal{B}} - (\xi^{\mathcal{B}})^2]} \begin{bmatrix} 0 & -i\xi^{\mathcal{B}} & 0 & 0 \\ 0 & 0 & 0 & 0 \\ 0 & 0 & 0 & -i\xi^{\mathcal{B}} \\ 0 & 0 & 0 & 0 \end{bmatrix} \\ &+ \frac{\kappa^2}{\omega \mu_0 \varepsilon_0 [\varepsilon^{\mathcal{B}} \mu^{\mathcal{B}} - (\xi^{\mathcal{B}})^2]} \begin{bmatrix} 0 & 0 & 0 & -\mu_0 \mu^{\mathcal{B}} \\ 0 & 0 & 0 & 0 \\ 0 & \varepsilon_0 \varepsilon^{\mathcal{B}} & 0 & 0 \\ 0 & 0 & 0 & 0 \end{bmatrix}. \end{aligned} \quad (3.3.7)$$

Let the eigenvector corresponding to the n th eigenvalue α_n of $[\underline{P}_{\underline{\underline{B}}}]$, be $[\underline{t}]^{(n)}$, $n \in [1, 4]$. After labeling the eigenvalues of $[\underline{P}_{\underline{\underline{B}}}]$ constrained to the condition $\text{Im}(\alpha_{1,2}) > 0$, the corresponding two eigenvectors can be used to write,

$$[\underline{f}(0+)] = \begin{bmatrix} [\underline{t}^{(1)}] & [\underline{t}^{(2)}] \end{bmatrix} \cdot \begin{bmatrix} c_1 \\ c_2 \end{bmatrix}. \quad (3.3.8)$$

for the propagation of the SPP wave, where c_1 and c_2 are unknown scalars (dimensionless). The other two eigenvalues of $[\underline{P}_{\underline{\underline{B}}}]$ pertain to the amplified wave as $z \rightarrow \infty$

and therefore, have no contribution to the existence of the SPP wave. At the same time, $[f(0-)]$ can be found from Eqs. (3.3.2) and (3.3.3), as given in matrix form

$$[f(0-)] = \begin{bmatrix} 0 & \frac{\alpha_{met}}{k_0} \\ 1 & 0 \\ \frac{\alpha_{met}}{k_0\eta_0} & 0 \\ 0 & -\frac{\varepsilon_{met}}{k_0\eta_0} \end{bmatrix} \cdot \begin{bmatrix} a_s \\ a_p \end{bmatrix}. \quad (3.3.9)$$

The SPP waves must have their tangential electric and magnetic fields continuous across the planar interface $z = 0$, requires that $[f(0-)] = [f(0+)]$, which can be re-arranged as the matrix equation

$$[\underline{Y}] \cdot \begin{bmatrix} a_s \\ a_p \\ c_1 \\ c_2 \end{bmatrix} = \begin{bmatrix} 0 \\ 0 \\ 0 \\ 0 \end{bmatrix}. \quad (3.3.10)$$

The 4×4 $[\underline{Y}]$ matrix must be singular to get the nontrivial solution, so that

$$\det[\underline{Y}] = 0 \quad (3.3.11)$$

is the dispersion relation for the SPP wave. This equation is solved to find out the solution for the SPP wave.

3.4 Results and Discussion

Representative numerical results are illustrated here to show the SPP-waves excitation at the interface of isotropic chiral material with the permittivity of that of water at $\lambda_0 = 633$ nm and an aluminum (relative permittivity $= -56 + 21i$). Both materials are taken to be non-magnetic with $\mu_A = \mu_B = 1$. Let me begin with the canonical problem and then follow up with two prism-coupled configurations.

3.4.1 Canonical problem

Before presenting the findings of the prism coupling techniques, let me consider the solution to the underlying canonical problem. As stated earlier, in the canonical

problem, the propagation of the SPP wave along the interface of a metallic half-space and the half-space filled up by a homogeneous isotropic chiral medium is considered. The solution of the dispersion relation found for the canonical problem is shown in Fig. 3.3 as a function of the real part of the chirality pseudoscalar. The metal (material \mathcal{A}) was taken to be aluminum and the chiral material was chosen with $\varepsilon^{\mathcal{B}} = 1.77 + 0.01i$ and $\text{Im}(\xi^{\mathcal{B}})$ was fixed at 0.0001. The figure shows that

- the SPP wave exists only when $\text{Re}(\xi^{\mathcal{B}}) \leq 0.04$, and
- the $\text{Re}(q/k_0)$ almost remains the same but the imaginary part approaches zero as $\text{Re}(\xi^{\mathcal{B}}) \rightarrow 0.04$.

The threshold value of $\text{Re}(\xi^{\mathcal{B}}) = 0.04$, shown in Fig. 3.3, depends upon the partnering metal and the permittivity of the chiral medium. As found in Fantino's paper [25], the surface waves cannot be observed along with the interface of two lossless media. Also, the threshold value of the $\text{Im}(\xi^{\mathcal{B}})$ of the chiral medium up to which the excitation of the SPP waves is possible was strongly dependent upon the permittivity of the chiral medium.

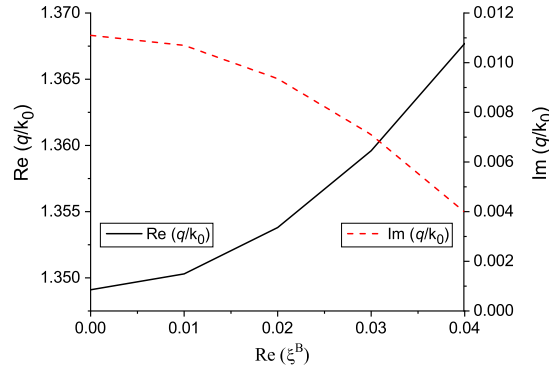


Figure 3.3: The $\text{Re}\{\cdot\}$ and $\text{Im}\{\cdot\}$ parts of the relative wavenumber of the SPP wave versus real part of $\xi^{\mathcal{B}}$ in the canonical problem. The imaginary part of $\xi^{\mathcal{B}}$ was fixed at 0.0001. Furthermore, $\varepsilon^{\mathcal{B}} = 1.77 + 0.01i$, $\mu^{\mathcal{A}} = \mu^{\mathcal{B}} = 1$, $\xi^{\mathcal{A}} = 0$, $\varepsilon^{\mathcal{A}} = \varepsilon_{met}^{\mathcal{A}} = -56 + 21i$, and $\lambda_0 = 633$ nm.

3.4.2 Conditions for the excitation of the SPP waves

The SPP waves cannot be excited by mere incidence of a planewave on an interface. To excite these waves, a material of refractive index higher than the ratio of the $\text{Re}(q)$ of the SPP wave to free-space wavenumber is required. This material is usually referred to as the prism. At a particular angle of incidence, the component of wave vector of the incident planewave along the interface matches that of the possible SPP wave and the SPP wave is launched. At this angle of incidence, a peak in the absorptance spectrum appears signifying the coupling of the incident energy to this SPP wave. The absorptance spectrum refers to the plots of absorptance as a function of the incidence angle, as given in Fig. 3.4. However, since the waveguide modes can also be excited in the finitely thick layers of the partnering materials, following three conditions [31, 32] have to be met by the absorptance peak to signify the SPP-wave excitation and to eliminate the waveguide modes:

- (i) The wavenumber along the interface, κ in this case, must match the $\text{Re}(q)$ obtained from the canonical problem.
- (ii) The angular location of the peak should also not change when the thickness of the partnering materials is changed because the SPP wave is highly confined to the interface and does not care if thicker partnering materials are present as long as the thickness is large enough to contain the SPP wave in the transverse direction.
- (iii) The spatial profiles of the three Cartesian components of the Poynting vector should indicate the localization of the power of the SPP wave to the interface.

In the following two sections, these three tests are adopted to verify the excitation of the SPP waves.

3.4.3 TKR prism coupling

Turbadar–Kretschmann–Raether (TKR) configuration [33, 34] is a commonly used experimental setup to excite the SPP wave in which a metal (material \mathcal{A}) is sandwiched between a sufficiently thick isotropic and homogeneous high-refractive-index dielectric material (prism) and a finitely-thick material (isotropic chiral medium \mathcal{B}).

This can be experimentally implemented by depositing a thin metallic film on top of a glass slide. The chiral medium can either be deposited on top of the metallic film or can be placed as a liquid. The other side of the glass slide is affixed to a prism with an index matching oil in between to avoid air film. I chose a prism with high refractive index $n_p = 2.6$ and the transmission medium is taken as air with refractive index $n_{tr} = 1$.

For representative numerical results, material \mathcal{A} is chosen as aluminum and material \mathcal{B} as an isotropic chiral medium (relative permittivity $= 1.77 + 0.01i$). The absorptance A_p against the incidence angle was computed and presented in Fig. 3.4 for fixed $L_{\mathcal{A}} = 15$ nm and $L_{\mathcal{B}} = 500$ nm for various values of the chirality pseudoscalar. When $\text{Re}(\xi^{\mathcal{B}}) \leq 0.04$, the absorptance peak at $\theta \sim 31.6^\circ$ in Fig. 3.4 represents the SPP waves since $\kappa/k_0 \sim 1.36$ at $\theta = 31.5^\circ$ is nearly the same as $\text{Re}(q/k_0) \sim 1.35$ and this peak was discerned to be independent of the thickness of the chiral material. The nearly constant angular location of the absorptance peak for various values of the chirality pseudoscalar is in line with Fig. 3.3, demonstrating the near-constant $\text{Re}(q/k_0)$ of the SPP waves in the canonical problem. The other peak with significant amplitude at almost $\theta = 25.3^\circ$ in the absorptance spectra for $\text{Re}(\xi^{\mathcal{B}}) \leq 0.04$ represents the waveguide mode because it changed its angular location when the thickness of the chiral material was changed. When $\text{Re}(\xi^{\mathcal{B}}) > 0.04$, the absorptance peak begins to drop and eventually vanish indicating the presence of a threshold value of the chirality parameter. The absence of any significant discernible peak in the spectra of absorptance for the s -polarized incidence in Fig. 3.5 shows that the SPP waves are not being excited by the s -polarized incident electromagnetic wave.

The SPP waves must be confined to the metal/chiral-medium interface. To see this, the absorptance A_p in Fig. 3.6 is plotted vs. the incidence angle for a fixed $\xi^{\mathcal{B}} = 0.03 + 0.0001i$ and $L_{\mathcal{A}} = 15$ nm but different thicknesses of the chiral medium for the p -polarized incidence. Figure 3.6 shows that the angular location of the absorptance peak does not change with the change in the thickness of the chiral medium. This fixed angular position of the absorptance peak at $\theta = 31.5^\circ$ shows the

confinement of the SPP wave to the interface in the chiral medium. Whereas, the other absorptance peak changes its angular location, indicating that it represents the waveguide modes. The fixed angular position can also be seen in the plot of total reflectance

$$R_p = \frac{|r_s|^2 + |r_p|^2}{|a_p|^2} \bigg|_{a_s=0}, \quad (3.4.1)$$

for p -polarized incidence as shown in Fig. 3.7 showing a reflectance dip. The reflectance dip representing the SPP-wave excitation is generally referred to as the attenuated total reflectance (ATR).

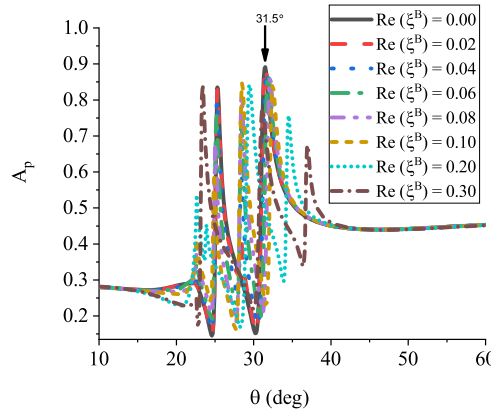


Figure 3.4: The absorptance A_p plotted versus the incidence angle θ for p -polarized incident electromagnetic wave in the TKR configuration when $n_p = 2.6$, $n_t = 1$, $L_A = 15$ nm, $L_B = 500$ nm, $\varepsilon^A = \varepsilon_{met}^A = -56 + 21i$, $\varepsilon^B = 1.77 + 0.01i$, $\xi^A = 0$, and $\text{Im}(\xi^B) = 0.0001$. The downward arrow pinpoints the absorptance peak that signifies the SPP-wave excitation.

To further confirm the SPP-waves excitation and the localization to the interface, the spatial variation of the three Cartesian components of power density

$$\underline{P}(\underline{r}) = \frac{1}{2} \text{Re} [\underline{E}(\underline{r}) \times \underline{H}^*(\underline{r})] \quad (3.4.2)$$

are shown in Fig. 3.8 for (a) $\xi^B = 0.00 + 0.0001i$ and (b) $\xi^B = 0.02 + 0.0001i$ when $\theta = 31.5^\circ$. The figure shows the strong confinement of the SPP waves to the interface of the plasmonic material and the isotropic chiral medium. The information about

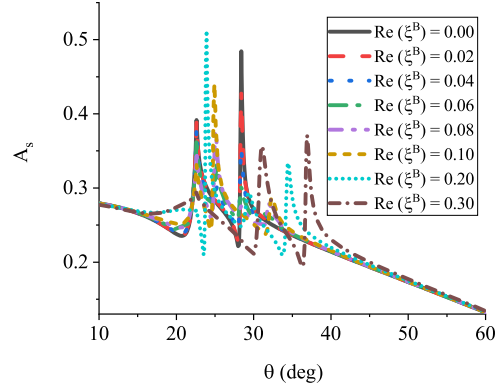


Figure 3.5: Same as Fig. 3.4 except that the absorptance is computed for the s -polarized incident plane wave.

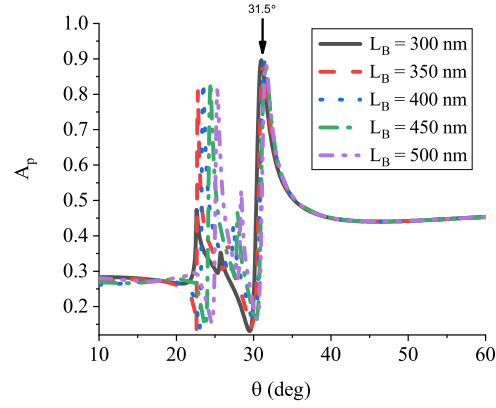


Figure 3.6: Same as Fig. 3.4 except that the absorptance is computed for different thicknesses of the chiral material and for fixed $\xi^B = 0.03 + 0.0001i$ and $L_A = 15$.

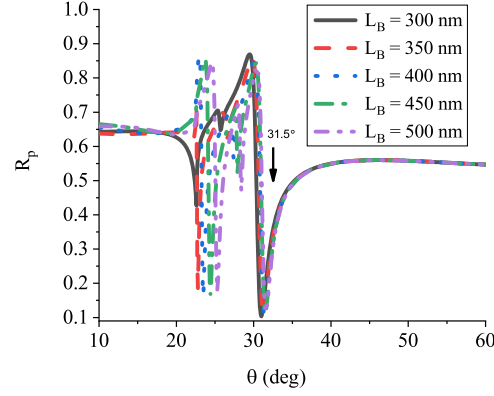


Figure 3.7: The total reflectance R_p plotted versus the incidence angle θ for p -polarized incident electromagnetic wave in the TKR configuration when $n_p = 2.6$, $n_t = 1$, $L_A = 15$ nm, $\varepsilon^A = \varepsilon_{met}^A = -56 + 21i$, $\varepsilon^B = 1.77 + 0.01i$, $\xi^A = 0$, and $\xi^B = 0.03 + 0.0001i$ for different values of L_B . The downward arrow pinpoints the reflectance dip that signifies the SPP-wave excitation.

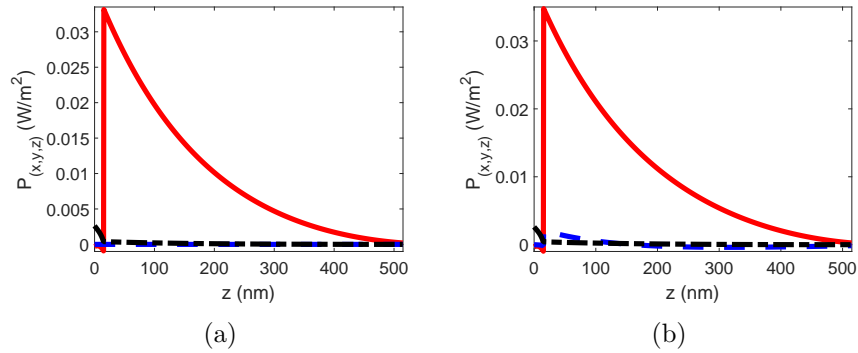


Figure 3.8: Magnitudes of the three Cartesian components of power density $\underline{P}(0, 0, z)$ versus z in the TKR configuration when p -polarized electromagnetic wave is incident at the metal/chiral-medium interface for (a) $\xi^B = 0.00 + 0.0001i$ and (b) $\xi^B = 0.02 + 0.0001i$ when the incidence angle $\theta = 31.5^\circ$. The other parameters are the same as given in Fig. 3.4. The x -, y -, and z -components are denoted, respectively, by a solid red line, a dashed blue line, and a chain-dashed black line.

the polarization states (p - or s -) of the SPP waves can be deduced from the field profiles (not shown here).

3.4.4 Turbadar–Otto prism coupling

The Turbadar–Otto configuration [33,35] is an alternative to the TKR configuration. In this configuration, material \mathcal{A} is the isotropic chiral medium and material \mathcal{B} is the metal. The absorptances A_p for this configuration are presented in Fig. 3.9 for fixed $L_{\mathcal{A}} = 500$ nm and $L_{\mathcal{B}} = 30$ nm for various values of the chirality pseudoscalar. For $\text{Re}(\xi^{\mathcal{A}}) \leq 0.04$, the absorptance peaks at $\theta \sim 31.2^\circ$ with $\kappa/k_0 \sim 1.35$ matches the solution in the canonical problem confirming the excitation of the SPP wave for p -polarized incidence. When $\text{Re}(\xi^{\mathcal{A}}) > 0.04$, the peak begins to diminish, just like in the TKR configuration. However, this figure shows that the absorptance peaks or reflectance dips are easy to identify in the Turbadar–Otto than in the TKR configuration. The angular locations of the absorptance peaks were found to be independent of the thickness of the chiral medium. A representation of this is provided in Fig. 3.10 for fixed $\xi^{\mathcal{A}} = 0.03 + 0.0001i$ and $L_{\mathcal{B}} = 30$ nm but different thicknesses of the chiral medium for the p -polarized incident light. The same angular independence is also indicated by the plots of the total reflectance R_p in Fig. 3.11.

Further confirmation comes from the magnitudes of the three Cartesian components of the power density presented in Fig. 3.12 plotted against distance z perpendicular to the interface for p -polarized incident planewave as shown in Fig. 3.12(a) and Fig. 3.12(b) for $\xi^{\mathcal{A}} = 0.00 + 0.0001i$ and $0.02 + 0.0001i$, respectively, at the incidence angle $\theta = 31.1^\circ$ of the absorptance peak identified earlier. The SPP-waves excitation can be discerned by strong localization of the three Cartesian components of the power density at the chiral-medium/metal interface.

To see if s -polarized incidence could excite the SPP waves in the Turbadar–Otto configuration, the plots of the absorptance for the s -polarized incident planewave were also computed and shown in Fig. 3.13. However, the angular locations of the absorptance peaks in the plots of A_s in Fig. 3.13 were found to depend on the thickness of the

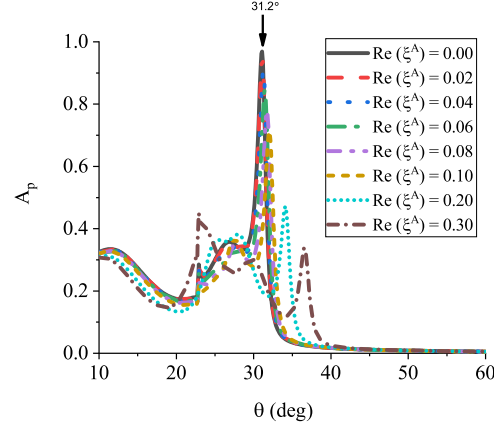


Figure 3.9: The absorbance A_p plotted versus the incidence angle θ for p -polarized electromagnetic wave in the Turbadar–Otto configuration when $n_p = 2.6$, $n_t = 1$, $L_A = 500$ nm, $L_B = 30$ nm, $\varepsilon^A = 1.77 + 0.01i$, $\varepsilon^B = \varepsilon_{met}^B = -56 + 21i$, $\text{Im}(\xi^A) = 0.0001$, and $\xi^B = 0$. The downward arrow pinpoints the absorbance peak that signifies the SPP-wave excitation.

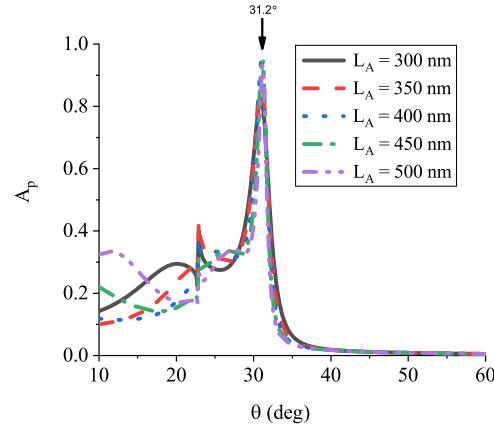


Figure 3.10: Same as Fig. 3.9 except that the absorbance is computed for different values of the thickness of the chiral medium for fixed $\xi^A = 0.03 + 0.0001i$ and $L_B = 30$ nm. The downward arrow pinpoints the absorbance peak that signifies the SPP-wave excitation.

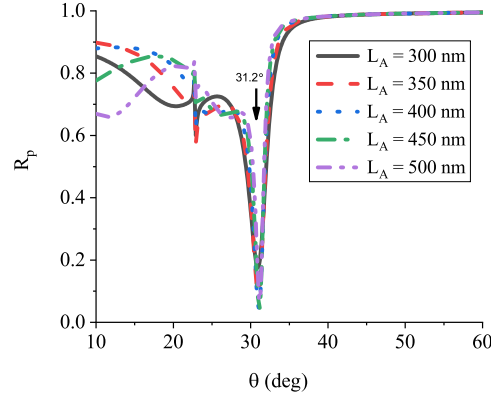


Figure 3.11: The total reflectance R_p plotted versus the incidence angle θ for p -polarized electromagnetic wave in the Turbadar–Otto configuration when $n_p = 2.6$, $n_t = 1$, $L_B = 30$ nm, $\varepsilon^A = 1.77 + 0.01i$, $\varepsilon^B = \varepsilon_{met}^B = -56 + 21i$, $\text{Im}(\xi^A) = 0.0001$, and $\xi^B = 0$. The downward arrow pinpoints the reflectance dip that signifies the SPP-wave excitation.

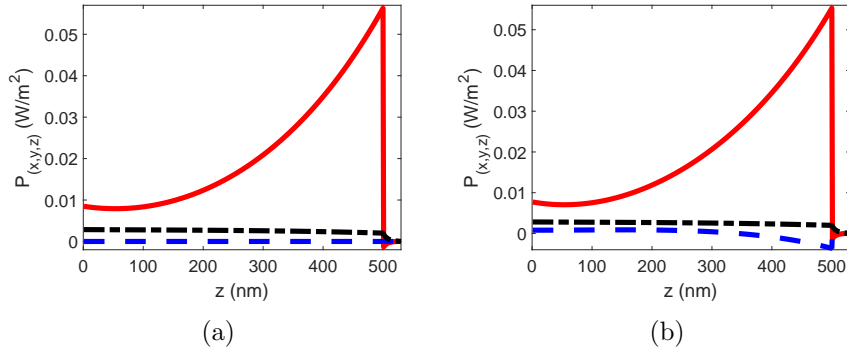


Figure 3.12: Magnitudes of the three Cartesian components of power density $\underline{P}(0, 0, z)$ versus z in the Turbadar–Otto configuration when p -polarized electromagnetic wave is incident at the chiral-medium/metal interface for (a) $\xi^A = 0.00 + 0.0001i$ and (b) $\xi^A = 0.02 + 0.0001i$ when the incidence angle $\theta = 31.1^\circ$. The other parameters are the same as given in Fig. 3.9. The x -, y -, and z -components are denoted, respectively, by a solid red line, a dashed blue line, and a chain-dashed black line.

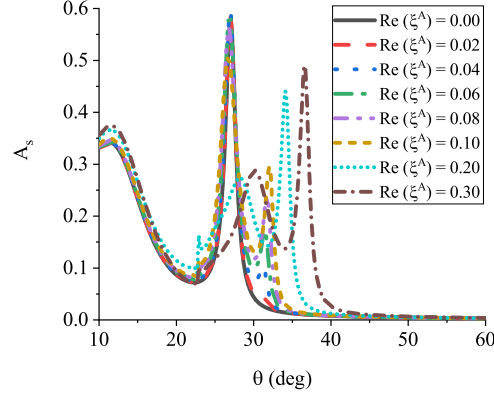


Figure 3.13: Same as Fig. 3.9 except that the absorptance is computed for the s -polarized incident planewave.

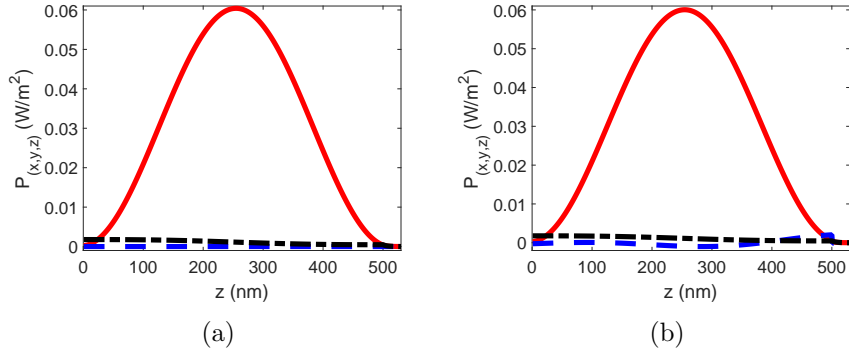


Figure 3.14: Magnitudes of the three Cartesian components of power density $\underline{P}(0, 0, z)$ versus z in the Turbadar–Otto configuration when s -polarized light is incident at the chiral-medium/metal interface for (a) $\xi^A = 0.00 + 0.0001i$ and (b) $\xi^A = 0.02 + 0.0001i$ when the incidence angle $\theta = 27^\circ$. The other parameters are the same as given in Fig. 3.9. The x -, y -, and z -components are denoted, respectively, by a solid red line, a dashed blue line, and a chain-dashed black line.

chiral medium. Therefore, these absorptance peaks symbolize the waveguide modes, as it is also verified from the profiles of the three Cartesian components of the power density given in Fig. 3.14 for two values of the chirality pseudoscalar. The figure clearly shows the propagation of the waveguide modes. Therefore, the s -polarized incident electromagnetic wave cannot excite the SPP waves at the interface of an isotropic homogeneous chiral medium and metal in the Turbadar–Otto configuration.

3.5 Conclusions

In this chapter, the SPP-waves excitation at the interface of a plasmonic material and a homogeneous isotropic chiral medium in the two prism couplings was theoretically established. Both the TKR and the Turbadar–Otto configurations can be used to excite the SPP waves. However, the results for the SPP-wave excitation in later configuration were easily discernible than the former. Moreover, the SPP waves existed only when the chirality pseudoscalar was smaller than a threshold value. The SPP waves could only be excited by the p -polarized planewave and not by the s -polarized incident planewave in both the configurations. The profiles of the three Cartesian components of power density showed that the SPP waves were found strongly localized to the planar interface of the plasmonic material and the chiral medium.

References

- [1] N. Engheta and P. Pelet, “Surface waves in chiral layers,” *Opt. Lett.* **16**, 723–725 (1991).
- [2] T. G. Mackay and A. Lakhtakia, “Simultaneous amplification and attenuation in isotropic chiral materials,” *J. Opt. (UK)* **18**, 055104 (2016).
- [3] R. D. Kampia and A. Lakhtakia, “Bruggeman model for chiral particulate composites,” *J. Phys. D: Appl. Phys.* **25**, 1390–1394 (1992).
- [4] T. G. Mackay and A. Lakhtakia, *Modern Analytical Electromagnetic Homogenization*, Morgan & Claypool (2015).
- [5] J. Noonan and T. G. Mackay, “On electromagnetic surface waves supported by an isotropic chiral material,” *Opt. Commun.* **434**, 224–229 (2019).
- [6] M. Naheed, M. Faryad, and T. G. Mackay, “Electromagnetic surface waves guided by the planar interface of isotropic chiral materials,” *J. Opt. Soc. Am. B* **36**, F1-F8 (2019).
- [7] A. Lakhtakia, V. K. Varadan, and V. V. Varadan, *Time-Harmonic Electromagnetic Fields in Chiral Media*, Springer-Verlag (1989).
- [8] A. Lakhtakia, *Beltrami Fields in Chiral Media*, World Scientific (1994).

- [9] D.-H. Kwon, D. H. Werner, A. V. Kildishev, and V. M. Shalaev, “Material parameter retrieval procedure for general bi-isotropic metamaterials and its application to optical chiral negative-index metamaterial design,” *Opt. Exp.* **16**, 11822–11829 (2008).
- [10] D. N. Pattanayak and J. L. Birman, “Wave propagation in optically active and magnetoelectric media of arbitrary geometry,” *Phys. Rev. B* **24**, 4271–4278 (1981).
- [11] P. Pelet and N. Engheta, “Coupled-mode theory for chirowaveguides,” *J. Appl. Phys.* **67**, 2742 (1990).
- [12] N. Engheta and P. Pelet, “Modes in chirowaveguides,” *Opt. Lett.* **14**, 593–595 (1989).
- [13] M. Chien, Y. Kim, and H. Grebel, “Mode conversion in optically active and isotropic waveguides,” *Opt. Lett.* **14**, 826–828 (1989).
- [14] P. Pelet and N. Engheta, “Chirostrip antenna: line source problem,” *J. Electromagn. Waves Appl.* **6**, 771–793 (1992).
- [15] D. L. Jaggard and X. Sun, “Theory of chiral multilayers,” *J. Opt. Soc. Am. A* **9**, 804–813 (1992).
- [16] D. L. Jaggard and N. Engheta, “Chirosorb as an invisible medium,” *Electron. Lett.* **25**, 173–174 (1989).
- [17] Q. Zhang and J. Li, “Characteristics of surface plasmon polaritons in a dielectrically chiral-metal-chiral waveguiding structure,” *Opt. Lett.* **41**, 3241–3244 (2016).
- [18] Q. Zhang, J. Li, X. Liu, and D. J. Gelmecha, “Dispersion, propagation, and transverse spin of surface plasmon polaritons in a metal-chiral-metal waveguide,” *Appl. Phys. Lett.* **110**, 161114 (2017).

- [19] M. Z. Yaqoob, A. Ghaffar, M. Alkanhal, Sajjad.-ur.-Rehman, and F. Razzaz, “Hybrid surface plasmon polariton wave generation and modulation by chiral-graphene-metal (CGM) structure,” *Sci. Rep.* **8**, 18029 (2018).
- [20] M. Z. Yaqoob, A. Ghaffar, M. A. S. Alkanhal, and Y. T. Aladadi, “Analysis of hybrid surface wave propagation supported by chiral metamaterial–graphene–metamaterial structures,” *Results Phys.* **14**, 102378 (2019).
- [21] L. D. Barron, *Molecular Light Scattering and Optical Activity*, Cambridge University Press (1982).
- [22] G. Mi and V. Van, “Characteristics of surface plasmon polaritons at a chiral-metal interface,” *Opt. Lett.* **39**, 2028–2031 (2014).
- [23] Q. Zhang, J. Li, X. Liu, D. J. Gelmecha, and W. Zhang, “Optical screwdriving induced by the quantum spin Hall effect of surface plasmons near an interface between strongly chiral material and air,” *Phys. Rev. A* **97**, 013822 (2018).
- [24] Q. Zhang, J. Li, and X. Liu, “Optical lateral forces and torques induced by chiral surface-plasmon-polaritons and their potential applications in recognition and separation of chiral enantiomers,” *Phys. Chem. Chem. Phys.* **21**, 1308-1314 (2019).
- [25] A. N. Fantino, “Planar interface between a chiral medium and a metal: Surface wave excitation,” *J. Mod. Opt.* **43**, 2581–2593 (1996).
- [26] C. A. Emeis, L. J. Oosterhoff, and G. D. Vries, “Numerical evaluation of Kramers-Kronig relations,” *Proc. Royal Soc. Lond. A* **297**, 54–65 (1967).
- [27] B. Y.-K. Hu, “Kramers-Kronig in two lines,” *Am. J. Phys.* **57**, 821 (1989).
- [28] A. Lakhtakia, “Comment on ‘Accelerated particle radiation in chiral media’,” *J. Appl. Phys.* **71**, 3059–3060 (1992).
- [29] H. C. Chen, *Theory of Electromagnetic Waves*, McGraw–Hill (1983).

- [30] J. A. Polo Jr., T. G. Mackay, and A. Lakhtakia, *Electromagnetic Surface Waves: A Modern Perspective*, Chapter 3, Elsevier (2013).
- [31] M. A. Motyka and A. Lakhtakia, “Multiple trains of same-color surface plasmon-polaritons guided by the planar interface of a metal and a sculptured nematic thin film,” *J. Nanophotonics* **2**, 021910 (2008).
- [32] M. A. Motyka and A. Lakhtakia, “Multiple trains of same-color surface plasmon-polaritons guided by the planar interface of a metal and a sculptured nematic thin film. Part II: Arbitrary incidence,” *J. Nanophotonics* **3**, 033502 (2009).
- [33] T. Turbadar, “Complete absorption of light by thin metal films,” *Proc. Phys. Soc.* **73**, 40–44 (1959).
- [34] E. Kretschmann and H. Raether, “Radiative decay of non radiative surface plasmons excited by light,” *Z. Naturforsch* **23**, 2135–2136 (1968).
- [35] A. Otto, “Excitation of nonradiative surface plasma waves in silver by the method of frustrated total reflection,” *Z. Phys.* **216**, 398–410 (1968).

Chapter 4

Metal and Non-Magnetic Uniaxially Chiral, Bianisotropic Material

In Chap. 3, I studied the excitation and the SPP-waves propagation along the interface of isotropic chiral material and the plasmonic material in the canonical problem and prism coupling. In this chapter, the excitation and the SPP-waves propagation along the planar interface of a plasmonic material and a non-magnetic, uniaxially chiral, bianisotropic material is investigated. The characteristics of the SPP waves in two prism-coupled configurations are studied and verified by the spatial profiles when the direction of propagation was assumed perpendicular to the direction of the chirality and uniaxiality. The associated canonical problem is also solved numerically for the confirmation of the findings of the prism-coupled configurations.

Chapter 4 is planned as follows: The introduction and related literature review is given in Sec. 4.1. The theoretical formulation of the prism-coupled problem is provided in Sec. 4.2. The illustrative numerical results of the canonical problem and prism coupling for the SPP-waves excitation are discussed and presented in Sec. 4.3. Conclusions are given in Sec. 4.4.

The work reported in this chapter is published in: *Opt. Commun.* **465**, 125611 (2020). Erratum: **465**, 126279 (2020).

4.1 Introduction

The uniaxial bianisotropic medium is a special case of the linear bianisotropic medium [1]. The non-magnetic uniaxially chiral, bianisotropic material [1–3] can be thought of as an assembly of parallel dielectric nano helixes in the host dielectric medium [1,2] when the period and thickness of these helixes are smaller than one-tenth of the operating wavelength of the electromagnetic wave inside the material. Such a medium can be easily fabricated using physical vapor deposition techniques [4]. For this work, the direction of uniaxiality and chirality of the chosen medium is assumed perpendicular to the direction of the propagation of the SPP waves guided by the interface [3]. The SPP-wave propagation supported by the interface of the non-magnetic uniaxially chiral medium and a plasmonic material has already been investigated theoretically in the canonical problem by [3]. Can the SPP-wave excitation be made possible at the interface of the non-magnetic uniaxially chiral, bianisotropic material and a plasmonic material in an experimental setup using two prism-coupled configurations, i.e., Turbadar–Kretschmann–Raether (TKR) [5,6] configuration, and Turbadar–Otto [5,7] configuration for s - and p -polarized incidence light? This chapter presents the results of theoretical investigations to answer this question. In this chapter, I consider a non-magnetic medium since magnetic effects are usually small. I will consider the general case in Chapter 5.

4.2 Theory: Prism-Coupled Configurations

A general formulation of the boundary-value problem of the prism-coupled configuration for two different homogeneous non-magnetic materials, namely, material \mathcal{A} and material \mathcal{B} , is presented. Consider the geometry of the problem as depicted in Fig. 4.1. The half-space $z \leq 0$ is the incidence half-space filled up by an unbounded isotropic homogeneous dielectric material (prism) with n_p as refractive index. The region $0 \leq z \leq L_{\mathcal{A}}$ is occupied by the homogeneous material \mathcal{A} . The region $L_{\mathcal{A}} \leq z \leq L_{\Sigma} = L_{\mathcal{A}} + L_{\mathcal{B}}$ is occupied by another homogeneous material \mathcal{B} and the

half-space $z \geq L_\Sigma$ is the transmission half-space filled up by the unbounded isotropic homogeneous dielectric material with refractive index n_t .

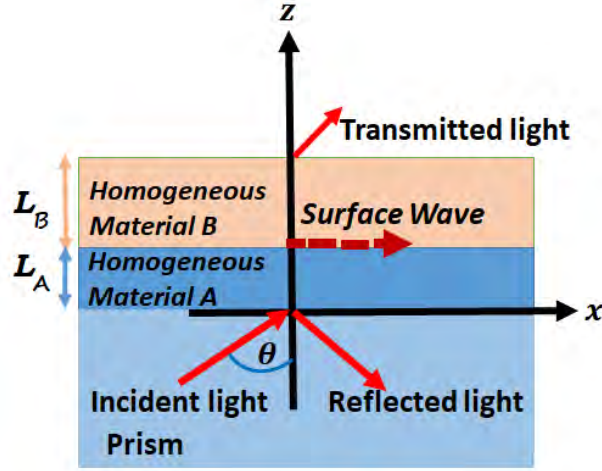


Figure 4.1: A general schematic for the SPP-waves excitation at the interface of two different homogeneous materials is shown in the prism coupling.

The homogeneous non-magnetic, uniaxially chiral, bianisotropic material is characterized by Tellegen constitutive relations in the frequency-domain [8] as

$$\left. \begin{aligned} \underline{D}(\underline{r}, \omega) &= \varepsilon_0 \left\{ \varepsilon_b(z) \underline{E}(\underline{r}, \omega) + [\varepsilon_a(z) - \varepsilon_b(z)] \hat{u}_z E_z(\underline{r}, \omega) \right\} + i\gamma(z) \hat{u}_z H_z(\underline{r}, \omega) \\ \underline{B}(\underline{r}, \omega) &= \mu_0 \mu_b(z) \underline{H}(\underline{r}, \omega) - i\gamma(z) \hat{u}_z E_z(\underline{r}, \omega) \end{aligned} \right\}, \quad (4.2.1)$$

where

$$\tau(z) = \begin{cases} \tau^A, & 0 \leq z \leq L_A \\ \tau^B, & L_A \leq z \leq L_A + L_B \end{cases}, \quad (4.2.2)$$

with $\tau = \{\varepsilon_a, \varepsilon_b, \mu_b, \gamma\}$, where $\varepsilon_a(z)$ and $\varepsilon_b(z)$ represent the relative permittivity scalars of the uniaxial medium, $\mu_b(z)$ represents the relative permeability scalar, and the chirality pseudoscalar of the material is represented by $\gamma(z)$. These parameters

are complex-valued and frequency dependent per the causality principle represented by the Kramers–Kronig relations [9].

The formulation for the prism-coupled configurations is the same as devised in Sec. 3.2. Therefore, these equations are not repeated here except

$$\left. \begin{aligned} e_z(z) &= \frac{i\kappa\gamma(z)e_y(z) + \mu_0\mu_b(z)\kappa h_y(z)}{\omega\{[\gamma(z)]^2 - \varepsilon_0\mu_0\varepsilon_a(z)\mu_b(z)\}} \\ h_z(z) &= \frac{-\varepsilon_0\varepsilon_a(z)\kappa e_y(z) + i\kappa\gamma(z)h_y(z)}{\omega\{[\gamma(z)]^2 - \varepsilon_0\mu_0\varepsilon_a(z)\mu_b(z)\}} \end{aligned} \right\}, \quad (4.2.3)$$

and

$$\begin{aligned} [\underline{\underline{P}}(z)] &= \omega \begin{bmatrix} 0 & 0 & 0 & \mu_0\mu_b(z) \\ 0 & 0 & -\mu_0\mu_b(z) & 0 \\ 0 & -\varepsilon_0\varepsilon_b(z) & 0 & 0 \\ \varepsilon_0\varepsilon_b(z) & 0 & 0 & 0 \end{bmatrix} \\ &+ \frac{\kappa^2}{\omega\{[\gamma(z)]^2 - \varepsilon_0\mu_0\varepsilon_a(z)\mu_b(z)\}} \begin{bmatrix} 0 & i\gamma(z) & 0 & \mu_0\mu_b(z) \\ 0 & 0 & 0 & 0 \\ 0 & -\varepsilon_0\varepsilon_a(z) & 0 & i\gamma(z) \\ 0 & 0 & 0 & 0 \end{bmatrix}, \end{aligned} \quad (4.2.4)$$

which are different from Sec. 3.2.

4.3 Numerical Results and Discussion

Representative numerical results are now presented to show the SPP-wave excitation at the interface of aluminum and a non-magnetic uniaxially chiral, bianisotropic material for correspondence with the underlying canonical problem in Ref. [3]. The materials assumed are non-magnetic and $\lambda_0 = 633$ nm was fixed. I begin with presenting the solution of the canonical boundary-value problem.

4.3.1 Canonical boundary-value problem

In the underlying canonical problem, the propagation of the SPP wave propagating along the interface of a homogeneous isotropic metallic half-space with $\varepsilon^{\mathcal{A}} = \varepsilon_{met}^{\mathcal{A}} = -56 + 21i$ and the homogeneous non-magnetic uniaxially chiral, bianisotropic half-space with $\varepsilon_a^{\mathcal{B}} = 2$, $\varepsilon_b^{\mathcal{B}} = 3$, and $\mu_b^{\mathcal{B}} = 1$ was considered.

To investigate the effect of the complex-valued chirality parameter, the relative wavenumbers q/k_0 of the possible SPP waves were obtained by solving the dispersion relation [3] against the $\text{Re}(\gamma^{\mathcal{B}}c) = \gamma^{\mathcal{B}}/\sqrt{\varepsilon_0\mu_0}$, using the Newton–Raphson technique. The $\text{Re}\{\cdot\}$ and $\text{Im}\{\cdot\}$ parts of q/k_0 of the SPP waves are presented in Fig. 4.2 as a function of the real part of $(\gamma^{\mathcal{B}}c) = \gamma^{\mathcal{B}}/\sqrt{\varepsilon_0\mu_0}$ while the imaginary part was fixed at 0.0001. The solutions for the SPP wave could only be found for $\text{Re}(\gamma^{\mathcal{B}}c) \leq 0.1631$. Moreover, the imaginary part of the solution approaches zero as $\text{Re}(\gamma^{\mathcal{B}}c) \rightarrow 0.1631$.

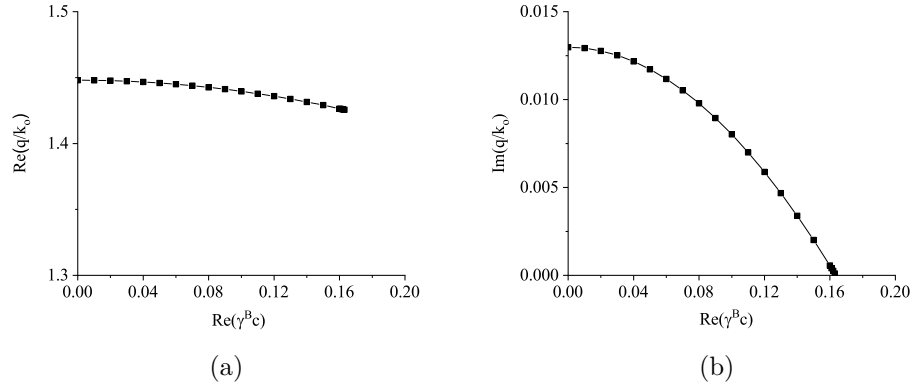


Figure 4.2: The (a) $\text{Re}\{\cdot\}$ and (b) $\text{Im}\{\cdot\}$ parts of the relative wavenumber q/k_0 plotted versus the real part of the relative chirality parameter $(\gamma^{\mathcal{B}}c) = \gamma^{\mathcal{B}}/\sqrt{\varepsilon_0\mu_0}$. The imaginary part of the parameter was fixed at $\text{Im}(\gamma^{\mathcal{B}}c) = 0.0001$.

4.3.2 TKR prism coupling

To excite the SPP waves, the Turbadar–Kretschmann–Raether (TKR) configuration is a commonly used experimental setup in which a thin metallic film (material \mathcal{A}) is placed between a sufficiently thick, homogeneous, isotropic high refractive index

dielectric material (prism) and a finitely-thick dielectric material (material \mathcal{B}). For the calculations in this section, the prism was chosen with refractive index $n_p = 1.73$ and the transmission medium was taken as made up of the same material as that of the prism with refractive index $n_t = n_p$. Furthermore, aluminum was chosen as the partnering metal (material \mathcal{A}) and non-magnetic uniaxially chiral, bianisotropic material was taken as material \mathcal{B} . These materials are specified by the following values of the constitutive parameters:

$$\left. \begin{aligned} \varepsilon_a^{\mathcal{A}} &= \varepsilon_b^{\mathcal{A}} = -56 + 21i, \\ \gamma^{\mathcal{A}} &= 0, \\ \mu_b^{\mathcal{A}} &= 1, \\ \varepsilon_a^{\mathcal{B}} &= 2, \\ \varepsilon_b^{\mathcal{B}} &= 3, \\ \mu_b^{\mathcal{B}} &= 1. \end{aligned} \right\} \quad (4.3.1)$$

The SPP-wave excitation in the prism-coupled configurations is elucidated using the absorptance spectrum and identifying the absorptance peaks that are independent of the thickness of the partnering bianisotropic material. The magnitude of wave vector of the electromagnetic wave along the direction of propagation must also match the $\text{Re}(q)$ found by the underlying canonical problem. The same approach is adopted here.

Before discussing the SPP-waves excitation in the TKR configuration, let me compute the θ_{inc} where the SPP waves are predicted to be excitable by the canonical problem. The incidence angle of excitation of the SPP wave θ_{inc}^{SPP} was computed by

$$\theta_{inc}^{SPP} = \sin^{-1}[\text{Re}(q)/n_p k_0] \quad (4.3.2)$$

and plotted as a function of the real part of the relative chirality parameter in Fig. 4.3 whereas the imaginary part was fixed at 0.0001.

The absorptances against the incidence angle and the chirality parameter were computed for the planewave incidence in the TKR configuration and are presented in

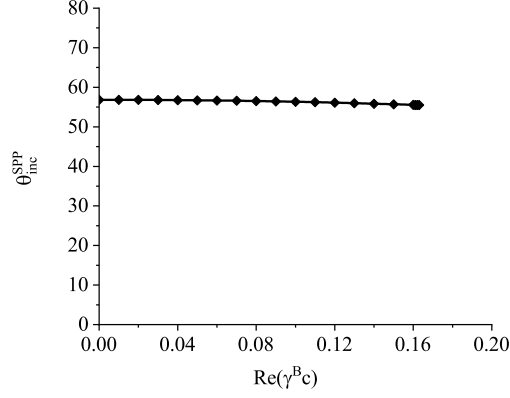


Figure 4.3: The angle of incidence of the SPP-wave excitation plotted versus the real part of the relative chirality parameter $(\gamma^B c) = \gamma^B / \sqrt{\varepsilon_0 \mu_0}$ predicted by canonical problem.

Figs. 4.4(a) and (b) when the electromagnetic wave is *p*- and *s*-polarized, respectively, for $L_A = 15$ nm and $L_B = 400$ nm. The absorptance band at $\theta \sim 58^\circ$ in the plot of A_p represents the excitation of the SPP waves since it did not change its position when $L_B = 500$ nm or $L_B = 600$ nm used (figures not shown). The wavenumber $\kappa = 1.467k_0$ also matches the real part of q obtained in the canonical problem [3]. The angular location of the absorptance band also agrees with Fig. 4.3. It can be noted that the absorptance band is present only when $\text{Re}(\gamma^B c) \lesssim 0.15$. This is in line with the prediction of the canonical problem as it was found there that the solution of the dispersion equation existed only when $\text{Re}(\gamma^B c) \lesssim 0.16$. Furthermore, Fig. 4.4(b) shows that the *s*-polarized incident electromagnetic wave does not excite any SPP wave in the TKR configuration as no evidence of absorptance band is found.

To see the confinement of the SPP waves to the interface, the three Cartesian components of power density

$$\underline{P}(\underline{r}) = \frac{1}{2} \text{Re} [\underline{E}(\underline{r}) \times \underline{H}^*(\underline{r})] \quad (4.3.3)$$

are presented in Fig. 4.5 for $\text{Re}(\gamma^B c) =$ (a) 0 and (b) 0.1. Both the profiles in Fig. 4.5 show strong localization of the SPP waves in the non-magnetic uniaxially chiral, bianisotropic medium. However, the efficiency of the excitation decreases for larger

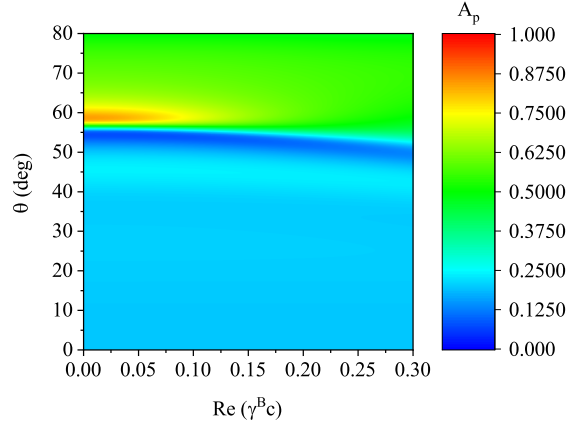
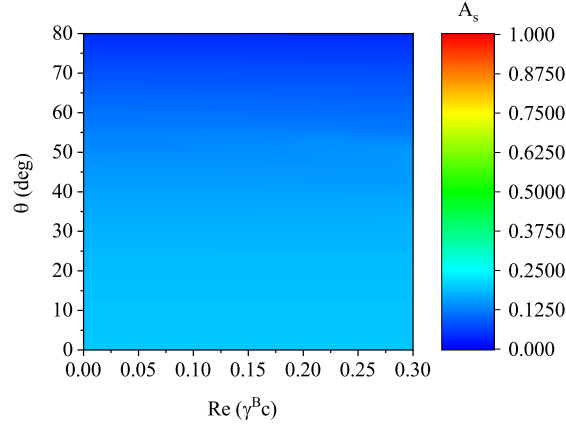
(a) TKR (p -polarized)(b) TKR (s -polarized)

Figure 4.4: Absorptances plotted versus the incidence angle θ and chirality parameter. The absorptances for the TKR configuration are given for (a) p -polarized incident planewave and (b) s -polarized incident planewave when $n_p = n_t = 1.73$, $L_A = 15$ nm, $L_B = 400$ nm, $\varepsilon^A = -56 + 21i$, $\varepsilon_a^B = 2$, $\varepsilon_b^B = 3$, $\gamma^A = 0$, and $\text{Im}(\gamma^B c) = 0.0001$.

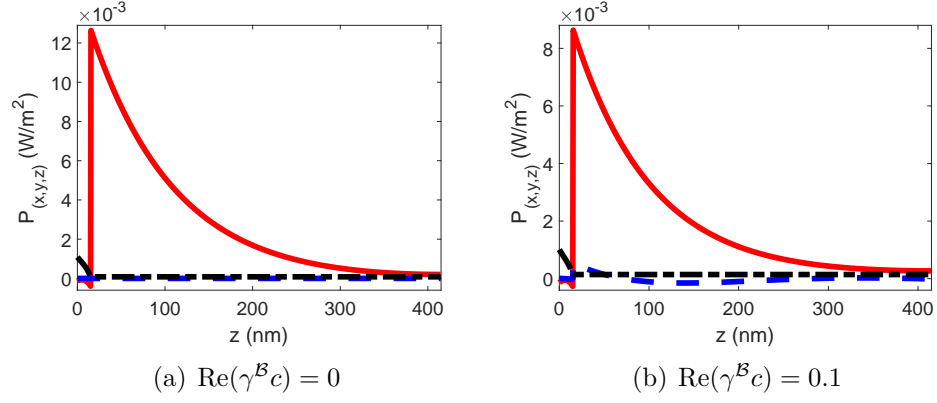


Figure 4.5: Magnitudes of the three Cartesian components of power density in the TKR configuration when (a) $\theta = 58.7^\circ$ and (b) $\theta = 58.9^\circ$. The other parameters are $n_p = n_t = 1.73$, $L_{\mathcal{A}} = 15$ nm, $L_{\mathcal{B}} = 400$ nm, $\varepsilon^{\mathcal{A}} = -56 + 21i$, $\varepsilon_a^{\mathcal{B}} = 2$, $\varepsilon_b^{\mathcal{B}} = 3$, $\gamma^{\mathcal{A}} = 0$, and $\text{Im}(\gamma^{\mathcal{B}}c) = 0.0001$ for p -polarized incidence. The P_x , P_y , and P_z components are shown by a solid red line, a dashed blue line, and a chain-dashed black line, respectively.

values of $\text{Re}(\gamma^{\mathcal{B}}c)$. The p -polarized nature of the SPP wave was deduced from the field profiles (not provided here) when chirality was negligible but, the SPP wave begins to deviate from the p -polarization state as the chirality increases. Furthermore, the figures unveil that the SPP wave is found localized to within 200 nm of the interface.

4.3.3 Turbadar–Otto prism coupling

The Turbadar–Otto configuration is an alternative experimental setup to excite the SPP waves. In this configuration, the material \mathcal{A} is a non-magnetic, uniaxially chiral, bianisotropic material and the material \mathcal{B} was assumed as aluminum metal. These

materials are specified by their constitutive parameters:

$$\left. \begin{aligned} \varepsilon_a^A &= 2, \\ \varepsilon_b^A &= 3, \\ \mu_b^A &= 1, \\ \mu_b^B &= 1, \\ \gamma^B c &= 0, \\ \varepsilon_a^B &= \varepsilon_b^B = -56 + 21i. \end{aligned} \right\} \quad (4.3.4)$$

To analyze the SPP-waves excitation in the Turbadar–Otto prism coupling, the absorptances against the incidence angle and the chirality parameter were computed and presented in Fig. 4.6(a) and (b) for p - and s -polarized planewaves, respectively, for $L_A = 400$ nm and $L_B = 30$ nm. The absorptance band at $\theta \sim 56.4^\circ$ that existed for smaller values of the chirality parameter in the plots of the A_p represent the SPP waves excited by p -polarized incidence light. However, this excitation takes place only when $\text{Re}(\gamma^A c) \lesssim 0.15$. The absorptance band matches Fig. 4.3. The wavenumber $\kappa = 1.441k_0$ also matches $\text{Re}(q)$ obtained in the canonical problem [3].

In the plots of A_s in Fig. 4.6(b); however, another band for larger values of the chirality exists that also signify the SPP waves, in contrast to the TKR configuration where s -polarized incidence did not excite the SPP waves. Therefore, the SPP waves in the Turbadar–Otto prism coupling are excited by both the p - and s -polarized incidence light though only p - excites for the lower values of the chirality parameter and only s - excites for the larger values of the chirality parameter.

The SPP-waves excitation in the Turbadar–Otto configuration is further confirmed by the magnitudes of the three Cartesian components of the power density and presented in Figs. 4.7 and 4.8, respectively, for the p - and the s -polarized incidence. Both the smaller as well as larger values of $\text{Re}(\gamma^A c)$ are considered for both the polarization states. Fig. 4.7 shows that the SPP waves are excited when $\text{Re}(\gamma^A c) = 0$ and 0.1 but no evidence of the SPP-wave excitation when $\text{Re}(\gamma^A c) = 0.2$ and 0.3. However, Fig. 4.8 shows that the s -polarized incident planewave can excite the SPP waves even

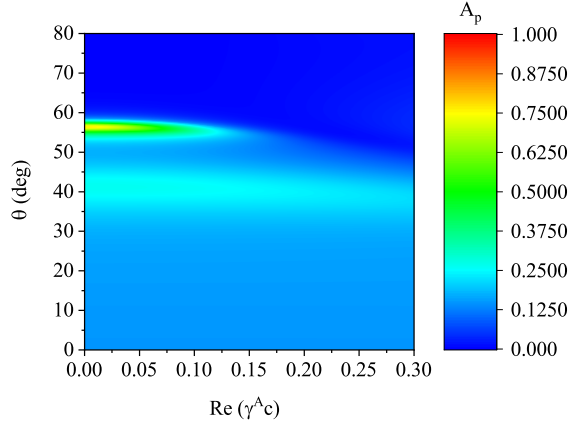
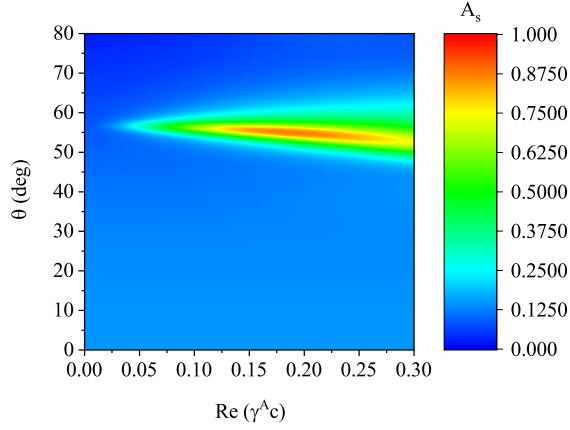
(a) Turbadar–Otto (*p*-polarized)(b) Turbadar–Otto (*s*-polarized)

Figure 4.6: Absorptances plotted versus the incidence angle θ and chirality parameter in the Turbadar–Otto configuration for (a) *p*-polarized incident planewave and (b) *s*-polarized incident planewave when $n_p = n_t = 1.73$, $L_A = 400$ nm, $L_B = 30$ nm, $\varepsilon_a^A = 2$, $\varepsilon_b^A = 3$, $\varepsilon^B = -56 + 21i$, $\text{Im}(\gamma^A c) = 0.0001$, and $\gamma^B = 0$.

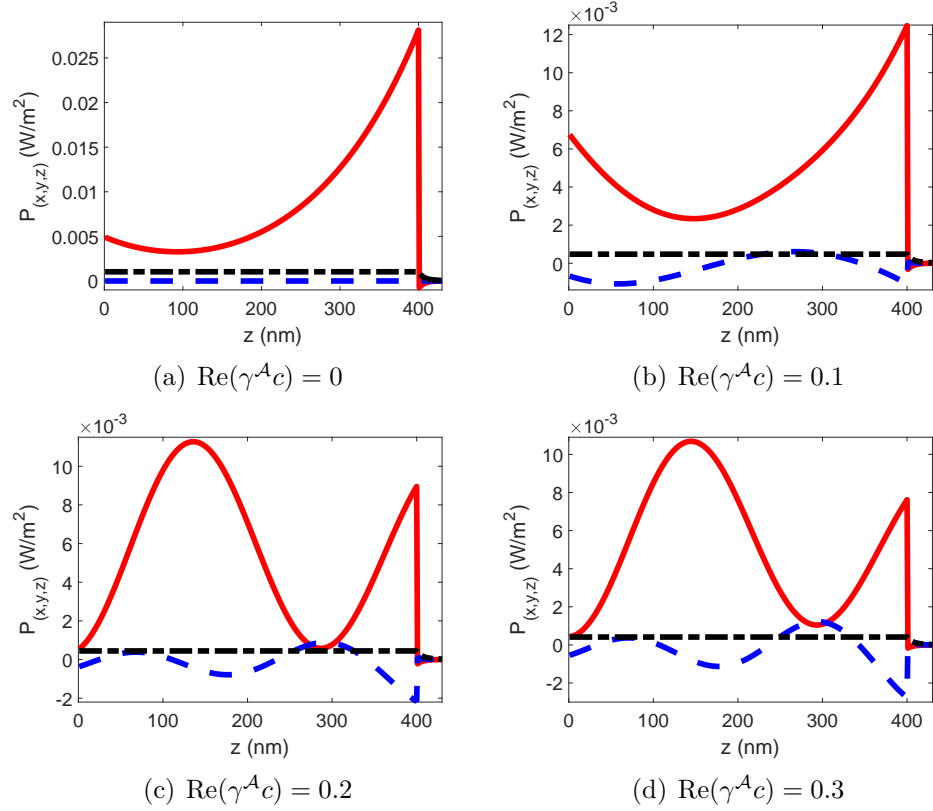


Figure 4.7: Magnitudes of the three Cartesian components of power density in the Turbadar–Otto configuration when (a) $\theta = 56.4^\circ$, (b) $\theta = 55.6^\circ$, (c) $\theta = 39.8^\circ$, and (d) $\theta = 38.1^\circ$ for p -polarized incidence when $n_p = 1.73$, $n_t = 1$, $L_A = 400$ nm, $L_B = 30$ nm, $\varepsilon_a^{\mathcal{A}} = 2$, $\varepsilon_b^{\mathcal{A}} = 3$, $\varepsilon^{\mathcal{B}} = -56 + 21i$, $\text{Im}(\gamma^{\mathcal{A}}c) = 0.0001$, and $\gamma^{\mathcal{B}} = 0$. P_x , P_y , and P_z components are shown by a solid red line, a dashed blue line, and a chain-dashed black line, respectively.

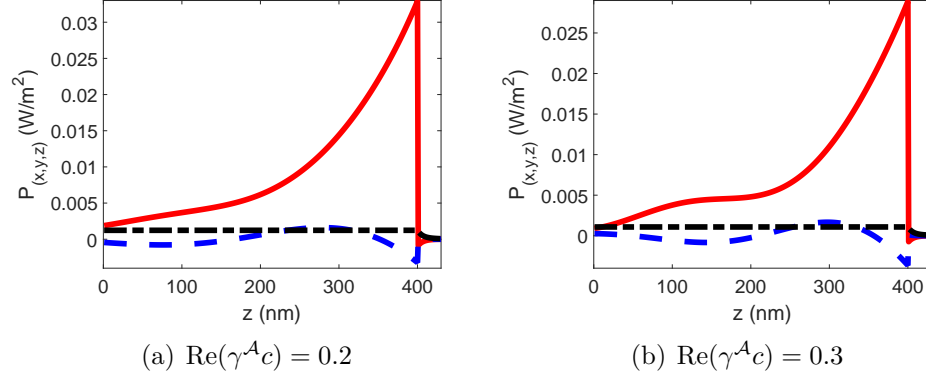


Figure 4.8: Same as Fig. 4.7 except that the incident planewave is s -polarized and (a) $\theta = 54.8^\circ$ and (b) $\theta = 52.6^\circ$.

when $\text{Re}(\gamma^A c) = 0.2$ and 0.3 . The SPP-waves excitation by the s -polarized incident electromagnetic wave is because of the coupling of s - and p -polarized waves inside the chiral medium.

4.4 Conclusions

The SPP-waves excitation at the planar interface of a non-magnetic, uniaxially chiral, bianisotropic material and a plasmonic material was investigated in the TKR and the Turbadar–Otto prism couplings. In the TKR configuration, only p -polarized incident planewave could excite the SPP waves, but in the Turbadar–Otto prism coupling, both the s - and the p -polarized planewaves could excite the SPP waves. However, only p -polarized incident light could excite the SPP waves when the chirality parameter was small and only s -polarized incident light could excite the SPP waves when the chirality parameter was large. Also, the SPP waves were found to be neither p - nor s -polarized in nature when the chirality parameter assumed large values.

References

- [1] I. V. Lindell and A. J. Viitanen, “Plane wave propagation in uniaxial bianisotropic medium,” *Electron. Lett.* **29**, 150–152 (1993).
- [2] A. J. Viitanen and I. V. Lindell, “Plane wave propagation in a uniaxial bianisotropic medium with application to a polarization transformer,” *Int. J. Infrared Millim. Waves* **14**, 1993–2010 (1993).
- [3] M. Faryad, “Surface plasmon-polariton waves guided by reciprocal, uniaxially chiral, bianisotropic material,” in: Plasmonics: Design, Materials, Fabrication, Characterization, and Applications XVII, D. P. Tsai and T. Tanaka, eds., *Proc. SPIE*. **11082**, 60–66 (2019).
- [4] A. Lakhtakia and R. Messier, *Sculptured Thin Films: Nanoengineered Morphology and Optics*, SPIE. Press (2005).
- [5] T. Turbadar, “Complete absorption of light by thin metal films,” *Proc. Phys. Soc.* **73**, 40–44 (1959).
- [6] E. Kretschmann and H. Raether, “Radiative decay of non radiative surface plasmons excited by light,” *Z. Naturforsch* **23**, 2135–2136 (1968).
- [7] A. Otto, “Excitation of nonradiative surface plasma waves in silver by the method of frustrated total reflection,” *Z. Phys. A* **216**, 398–410 (1968).
- [8] J. A. Polo Jr., T. G. Mackay, and A. Lakhtakia, *Electromagnetic Surface Waves: A Modern Perspective*, Elsevier (2013).

- [9] B. Y.-K. Hu, “Kramers–Kronig in two lines,” *Am. J. Phys.* **57**, 821 (1989).

Chapter 5

Metal and Obliquely Mounted, Uniaxially Chiral, Bianisotropic Material

In Chap. 4, I considered the excitation and the SPP-waves propagation along the planar interface of a plasmonic material and the non-magnetic, uniaxially chiral, bianisotropic materials whereas the waves were guided by the interface perpendicular to the direction of the uniaxiality and chirality. In this chapter, the SPP-waves excitation is considered when bianisotropic material is magnetic with its optic axis making an arbitrary angle with the interface plane. Such a material can be fabricated as a parallel assembly of helixes with the axis of the helixes making an arbitrary tilt angle with the metallic substrate. The canonical problem as well as the two prism-coupled configurations are investigated. The SPP-wave propagation was restricted to be in the morphologically significant plane of the bianisotropic material that contains tilted helixes.

Chapter 5 is planned as follows: The introduction and related literature review is given in Sec. 5.1. The canonical problem is formulated and solved in Sec. 5.2. The formulation and the results for the prism-coupled configurations are provided in Sec. 5.3. Conclusions are given in Sec. 5.4.

The work reported in this chapter is published in: *J. Electromagn. Waves Appl.* **34**, 1756–1770 (2020).

5.1 Introduction

Bianisotropic chiral materials combine the periodicity and the anisotropy in a special fashion where the period of the composing parallel helixes is much smaller than the wavelength of interest of electromagnetic waves. The isotropic chiral mediums have randomly oriented helixes in a dielectric host [1–4], but in a bianisotropic chiral medium, the helixes are oriented parallel to each other [5]. The simplest bianisotropic chiral medium is a uniaxially chiral, bianisotropic medium which can be realized with the parallel assembly of circular helixes [6–9] provided that the pitch of the helixes are much smaller than the wavelength of the SPP waves. These materials have potential applications in the microwave regime [10, 11], optical activity [12], reciprocal phase shifter [13], polarization transformation [14–16], non-reflecting shields and antenna radomes [17], radar-absorbing layers [18], and circular birefringence and dichroism [19], to name a few.

In chapter 4, I studied the SPP-waves propagation along the interface of a plasmonic material and the non-magnetic uniaxially chiral, bianisotropic medium, for a special case when the axis of uniaxiality was assumed perpendicular to the interface, both in the canonical problem [20] and in the prism-coupled configurations [21]. In that chapter, the permittivity dyadic was taken to be uniaxial, but the permeability dyadic was taken to be a scalar multiple of the identity dyadic. In the present work, I lift the restrictions on the “optic axis” and allow it to have an arbitrary angle with the metallic interface. Moreover, I have used a more realistic permeability dyadic, that is, as a uniaxial dyadic. I present both the canonical and the prism-coupled configurations in this chapter.

5.2 Canonical Problem

A canonical problem is a theoretical approach of finding the dispersion relation for the propagation of surface waves propagating along the interface of two half-spaces [22, 23]. Here, I am interested in the SPP waves when one half-space is filled

by a plasmonic material and the other by an obliquely mounted uniaxially chiral, bianisotropic material.

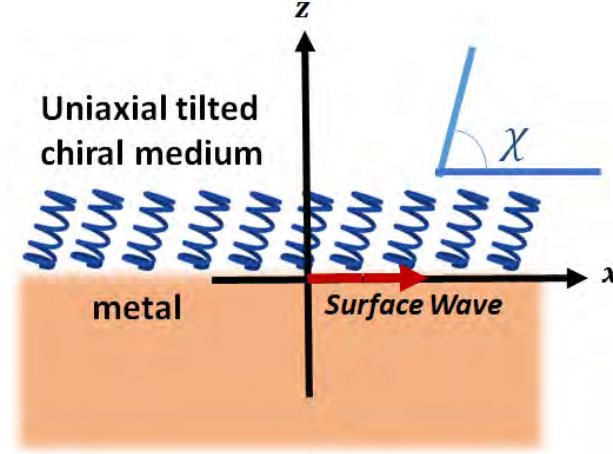


Figure 5.1: The SPP-waves propagation along the interface of a plasmonic material and the uniaxially chiral, bianisotropic medium is shown schematically in the canonical problem.

Figure 5.1 shows the canonical problem schematically. The half-space $z < 0$ is occupied by a plasmonic material with ε_{met} as relative permittivity. The half-space $z > 0$ is occupied by an obliquely mounted homogeneous, uniaxially chiral, bianisotropic medium specified by Tellegen constitutive relations [4]

$$\left. \begin{aligned} \underline{D}(\underline{r}, \omega) &= \underline{\underline{\varepsilon}} \cdot \underline{E}(\underline{r}, \omega) + \underline{\underline{\xi}} \cdot \underline{H}(\underline{r}, \omega) \\ \underline{B}(\underline{r}, \omega) &= \underline{\underline{\mu}} \cdot \underline{H}(\underline{r}, \omega) - \underline{\underline{\xi}}^T \cdot \underline{E}(\underline{r}, \omega) \end{aligned} \right\}, \quad z \geq 0. \quad (5.2.1)$$

The permittivity dyadic [8,9]

$$\underline{\underline{\varepsilon}} = \varepsilon_0 \underline{\underline{S}}_y \cdot [\varepsilon_a \hat{u}_z \hat{u}_z + \varepsilon_b \hat{u}_x \hat{u}_x + \varepsilon_b \hat{u}_y \hat{u}_y] \cdot \underline{\underline{S}}_y^{-1}, \quad (5.2.2)$$

and the permeability dyadic [8,9]

$$\underline{\underline{\mu}} = \mu_0 \underline{\underline{S}}_y \cdot [\mu_a \hat{u}_z \hat{u}_z + \mu_b \hat{u}_x \hat{u}_x + \mu_b \hat{u}_y \hat{u}_y] \cdot \underline{\underline{S}}_y^{-1}, \quad (5.2.3)$$

of the uniaxially chiral medium depend upon the rotation dyadic

$$\underline{\underline{S}}_y = \cos \chi (\underline{\hat{u}}_x \underline{\hat{u}}_x + \underline{\hat{u}}_z \underline{\hat{u}}_z) + \sin \chi (\underline{\hat{u}}_z \underline{\hat{u}}_x - \underline{\hat{u}}_x \underline{\hat{u}}_z) + \underline{\hat{u}}_y \underline{\hat{u}}_y, \quad (5.2.4)$$

that incorporates the tilt χ of the helices of the medium with respect to the y axis.

The magneto-electric constitutive dyadic is taken as [8, 9]

$$\underline{\underline{\xi}} = \underline{\underline{S}}_y \cdot i\gamma \underline{\hat{u}}_z \underline{\hat{u}}_z \cdot \underline{\underline{S}}_y^{-1}, \quad (5.2.5)$$

where the complex-valued chirality parameter γ depends upon the constitution of the bianisotropic medium fabricated as parallel helices in a host medium [8, 9]. The standard physical vapor deposition technique by directing a vapor flux at a substrate rotating about the z axis can be used for fabrication of the helicoidal morphology. The substrate is placed at an angle $\chi_v < \pi/2$ to the incident vapor flux. A wide variety of helicoidal morphologies can be made possible by controlling the two fundamental axes of substrate rotation [24].

5.2.1 Formulation of the dispersion equation

The SPP wave is assumed to propagate along the x axis. Therefore, the propagation of the SPP wave is in the plane containing the tilted helices. The field phasors in the plasmonic half-space can be specified as [25, 26]

$$\left. \begin{aligned} \underline{E}_{met}(\underline{r}) &= \left[a_s \underline{\hat{u}}_y + a_p \left(\frac{\alpha_{met}}{k_0} \underline{\hat{u}}_x + \frac{q}{k_0} \underline{\hat{u}}_z \right) \right] \exp(iqx) \\ \underline{H}_{met}(\underline{r}) &= \frac{1}{\eta_0} \left[a_s \left(\frac{\alpha_{met}}{k_0} \underline{\hat{u}}_x + \frac{q}{k_0} \underline{\hat{u}}_z \right) - a_p \varepsilon_{met} \underline{\hat{u}}_y \right] \exp(iqx) \end{aligned} \right\}, \quad z \leq 0, \quad (5.2.6)$$

where $q^2 + \alpha_{met}^2 = k_0^2 \varepsilon_{met}$. The wavenumber q of the SPP wave is complex-valued. The amplitudes of the s - and p -polarized components of the SPP waves are represented by a_s and a_p , respectively, which are unknown scalars. The condition $\text{Im}(\alpha_{met}) > 0$ must be satisfied for the SPP-waves propagation to ensure the decay of field phasors in the metal perpendicular to the interface as $z \rightarrow -\infty$.

The electromagnetic field phasors in the uniaxially chiral, bianisotropic medium

can be written as [25]

$$\left. \begin{aligned} \underline{E}(\underline{r}) &= [e_x(z)\hat{\underline{u}}_x + e_y(z)\hat{\underline{u}}_y + e_z(z)\hat{\underline{u}}_z] \exp(iqx) \\ \underline{H}(\underline{r}) &= [h_x(z)\hat{\underline{u}}_x + h_y(z)\hat{\underline{u}}_y + h_z(z)\hat{\underline{u}}_z] \exp(iqx) \end{aligned} \right\}. \quad (5.2.7)$$

Substitution of Eqs. (5.2.1) and (5.2.7) in Maxwell curl postulates results in four partial differential equations and two algebraic equations. The algebraic equations give

$$\begin{aligned} e_z &= \frac{\sin(2\chi)}{2Q} [\varepsilon_0\mu_0\mu_{ab}(\varepsilon_a - \varepsilon_b) - \gamma^2 \cos^2 \chi] e_x - \frac{i\gamma q \cos^2 \chi}{\omega Q} e_y \\ &\quad - \frac{i\gamma\mu_0 \sin(2\chi)}{2Q} [(\mu_a - \mu_b) \cos^2 \chi - \mu_{ab}] h_x - \frac{\mu_0\mu_{ab}q}{\omega Q} h_y, \end{aligned} \quad (5.2.8)$$

$$\begin{aligned} h_z &= \frac{i\gamma\varepsilon_0 \sin(2\chi)}{2Q} [\cos^2 \chi(\varepsilon_a - \varepsilon_b) - \varepsilon_{ab}] e_x + \frac{\varepsilon_0\varepsilon_{ab}q}{\omega Q} e_y \\ &\quad + \frac{\sin(2\chi)}{2Q} [\varepsilon_0\mu_0\varepsilon_{ab}(\mu_a - \mu_b) - \gamma^2 \cos^2 \chi] h_x - \frac{i\gamma q \cos^2 \chi}{\omega Q} h_y, \end{aligned} \quad (5.2.9)$$

where

$$\varepsilon_{ba} = \varepsilon_b \cos^2 \chi + \varepsilon_a \sin^2 \chi, \quad (5.2.10)$$

$$\varepsilon_{ab} = \varepsilon_a \cos^2 \chi + \varepsilon_b \sin^2 \chi, \quad (5.2.11)$$

$$\mu_{ba} = \mu_b \cos^2 \chi + \mu_a \sin^2 \chi, \quad (5.2.12)$$

$$\mu_{ab} = \mu_a \cos^2 \chi + \mu_b \sin^2 \chi, \quad (5.2.13)$$

$$Q = \varepsilon_0\mu_0\varepsilon_{ab}\mu_{ab} - \gamma^2 \cos^4 \chi. \quad (5.2.14)$$

The four differential equations can be re-arranged as the matrix ordinary differential equation [24, 25]

$$\frac{d}{dz}[\underline{f}(z)] = i[\underline{P}]\cdot[\underline{f}(z)], \quad (5.2.15)$$

where

$$[\underline{f}(z)] = \begin{bmatrix} e_x(z) \\ e_y(z) \\ h_x(z) \\ h_y(z) \end{bmatrix} \quad (5.2.16)$$

and

$$\begin{aligned}
[\underline{P}] = & \frac{\omega}{Q} \begin{bmatrix} 0 & 0 & 0 & \mu_0 \mu_b Q \\ 0 & 0 & \mu_0 \mu_b (-\varepsilon_0 \mu_0 \varepsilon_a \varepsilon_{ab} + \gamma^2 \cos^2 \chi) & 0 \\ 0 & -\varepsilon_0 \varepsilon_b Q & 0 & 0 \\ \varepsilon_0 \varepsilon_b (\varepsilon_0 \mu_0 \varepsilon_a \mu_{ab} - \gamma^2 \cos^2 \chi) & 0 & 0 & 0 \end{bmatrix} \\
& + \frac{q \varepsilon_0 \mu_0 \cos \chi \sin \chi}{Q} \begin{bmatrix} (\varepsilon_a - \varepsilon_b) \mu_{ab} & 0 & 0 & 0 \\ 0 & (\mu_a - \mu_b) \varepsilon_{ab} & 0 & 0 \\ 0 & 0 & (\mu_a - \mu_b) \varepsilon_{ab} & 0 \\ 0 & 0 & 0 & (\varepsilon_a - \varepsilon_b) \mu_{ab} \end{bmatrix} \\
& + \frac{i \gamma \omega \varepsilon_0 \mu_0 \varepsilon_b \mu_b \sin^2 \chi}{Q} \begin{bmatrix} 0 & 0 & 0 & 0 \\ 1 & 0 & 0 & 0 \\ 0 & 0 & 0 & 0 \\ 0 & 0 & 1 & 0 \end{bmatrix} + \frac{i \gamma q \cos \chi \sin \chi}{Q} \begin{bmatrix} 0 & 0 & \mu_0 \mu_b & 0 \\ 0 & 0 & 0 & \mu_0 \mu_b \\ -\varepsilon_0 \varepsilon_b & 0 & 0 & 0 \\ 0 & -\varepsilon_0 \varepsilon_b & 0 & 0 \end{bmatrix} \\
& - \frac{q \gamma^2 \cos^3 \chi \sin \chi}{Q} \begin{bmatrix} 1 & 0 & 0 & 0 \\ 0 & 1 & 0 & 0 \\ 0 & 0 & 1 & 0 \\ 0 & 0 & 0 & 1 \end{bmatrix} + \frac{q^2}{\omega Q} \begin{bmatrix} 0 & -i \gamma \cos^2 \chi & 0 & -\mu_0 \mu_{ab} \\ 0 & 0 & 0 & 0 \\ 0 & \varepsilon_0 \varepsilon_{ab} & 0 & -i \gamma \cos^2 \chi \\ 0 & 0 & 0 & 0 \end{bmatrix}. \quad (5.2.17)
\end{aligned}$$

Equation (5.2.15) can be solved to get [24]

$$[\underline{f}(z)] = \exp \{ i z [\underline{P}] \} \cdot [\underline{f}(0+)], \quad z > 0. \quad (5.2.18)$$

To write the fields in terms of the modes that represent the SPP waves, I need to find the eigenvectors and eigenvalues of the matrix $[\underline{P}]$. Let $[\underline{t}^{(n)}]$ be the eigenvectors corresponding to the eigenvalues α_n , $n \in [1, 4]$, of the $[\underline{P}]$ matrix. The fields of the SPP waves have to be written in terms of those eigenvectors of $[\underline{P}]$ that have $\text{Im}(\alpha_{1,2}) > 0$ so that the fields decay as $z \rightarrow \infty$, as [25, 26]

$$[\underline{f}(0+)] = [\underline{t}^{(1)} \quad \underline{t}^{(2)}] \cdot \begin{bmatrix} c_1 \\ c_2 \end{bmatrix}, \quad z > 0, \quad (5.2.19)$$

where c_1 and c_2 are unknown scalars. On the other side of the interface $z \leq 0$, the fields can be written as [25, 26]

$$[\underline{f}(0-)] = \begin{bmatrix} 0 & \frac{\alpha_{met}}{k_0} \\ 1 & 0 \\ \frac{\alpha_{met}}{k_0 \eta_0} & 0 \\ 0 & -\frac{\varepsilon_{met}}{\eta_0} \end{bmatrix} \cdot \begin{bmatrix} a_s \\ a_p \end{bmatrix} \quad (5.2.20)$$

using Eq. (5.2.6). The SPP waves must have their tangential electric and magnetic fields continuous across the planar interface $z = 0$, requires that $[\underline{f}(0+)] = [\underline{f}(0-)]$, which can be re-arranged to get

$$[\underline{\underline{Y}}] \cdot \begin{bmatrix} a_s \\ a_p \\ c_1 \\ c_2 \end{bmatrix} = \begin{bmatrix} 0 \\ 0 \\ 0 \\ 0 \end{bmatrix}. \quad (5.2.21)$$

The $[\underline{\underline{Y}}]$ matrix must be singular for a nontrivial solution, so that

$$\det[\underline{\underline{Y}}] = 0 \quad (5.2.22)$$

is the dispersion relation for the SPP waves. This equation need to be solved for the determination of the wavenumber q of the SPP waves. Thereafter, the fields can be found using Eqs. (5.2.6) and (5.2.18).

5.2.2 Solution of the dispersion equation

I solved the dispersion equation using Newton–Raphson method and searched the solutions q against the tilt angle χ by keeping $\varepsilon_a = 2.3 + 0.023i$, $\varepsilon_b = 3.7 + 0.037i$, $\mu_a = 0.8 + 0.008i$, and $\mu_b = 1 + 0.01i$ at $\lambda_0 = 633$ nm. Furthermore, the chirality parameter was chosen to have values $\gamma = 0.1(1 + i0.001), 0.12(1 + i0.001), 0.15(1 + i0.001), 0.2(1 + i0.001)$, and $0.3(1 + i0.001)$. These values were motivated by the experimentally obtained parameters for the uniaxially chiral bianisotropic medium fabricated in the microwave range reported in Refs. [8, 9]. Even though the values

were obtained in the microwave regime, I believe that similar values can be obtained in the optical spectral domain since these values of permittivity are typical in the optical regime and by scaling the dimensions of the helixes, similar values of the constitutive parameters can be obtained. Therefore, the chosen material is experimentally realizable. The partnering plasmonic material was assumed aluminum with $\varepsilon_{met} = -56 + 21i$.

Since this chapter is penned to focus on the chirality of the bianisotropic material, I solved the dispersion equation as a function of the tilt angle χ for several values of the complex-valued chirality parameter. Let me recall that I am investigating the SPP waves propagating in the morphologically significant plane (xz plane) that contains the helixes of the material. The $\text{Re}\{\cdot\}$ and $\text{Im}\{\cdot\}$ parts of (q/k_0) of the SPP waves are shown in Fig. 5.2(a,b), for five values of the chirality parameter. The figure indicates that the angular range of existence for the SPP waves is strongly dependent upon the chirality parameter. Indeed, I found that the SPP waves can exist for any tilt angle of the helixes in the range $[0^\circ, 90^\circ]$ when the chirality parameter had $\text{Re}(\gamma) \leq 0.11\sqrt{\varepsilon_0\mu_0}$ with its imaginary part being 1% of the real part. For the higher magnitudes of the chirality parameter, the SPP waves can exist for a narrower range which gets narrower as the magnitude of γ increases. Essentially, the solutions of the canonical problem for tilt angle χ are the same as for $180^\circ - \chi$, and if q is a solution, then $-q$ is also a solution.

To see the degree of confinement of the SPP waves to the interface, I computed the magnitudes of the three Cartesian components of power density

$$\underline{P}(\underline{r}) = \frac{1}{2} \text{Re} [\underline{E}(\underline{r}) \times \underline{H}^*(\underline{r})] \quad (5.2.23)$$

for several solutions as a function of z . The variations of the three components of $\underline{P}(\underline{r})$ are presented in Fig. 5.3 for a representative solution. The figure shows that the solutions of the dispersion relation indeed affirm the SPP waves because of decay of the components of $\underline{P}(\underline{r})$ away from the interface. Furthermore, the SPP wave is found to be strongly localized because it decays fully within about 300 nm in the bianisotropic medium, which is smaller than the typical decay length in an isotropic

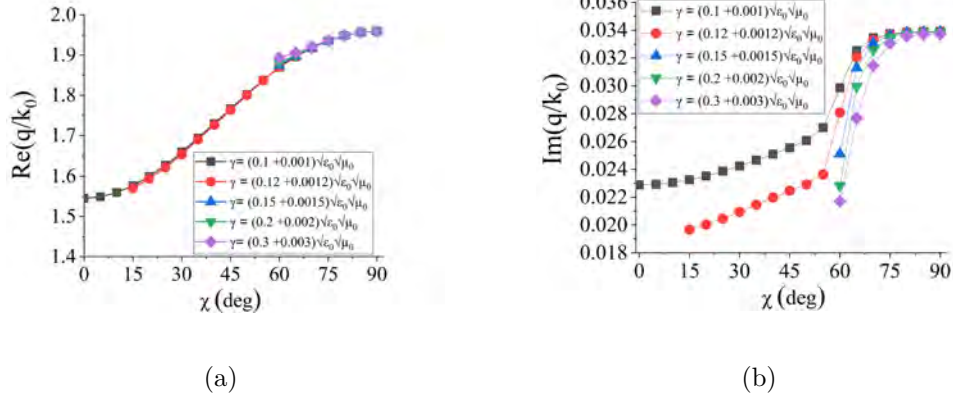


Figure 5.2: The $\text{Re}\{\cdot\}$ and $\text{Im}\{\cdot\}$ parts of q/k_0 of the SPP waves plotted against the tilt angle χ when $\varepsilon_{\text{met}} = -56 + 21i$, $\varepsilon_a = 2.3 + 0.023i$, $\varepsilon_b = 3.7 + 0.037i$, $\mu_a = 0.8 + 0.008i$, and $\mu_b = 1 + 0.01i$ were chosen.

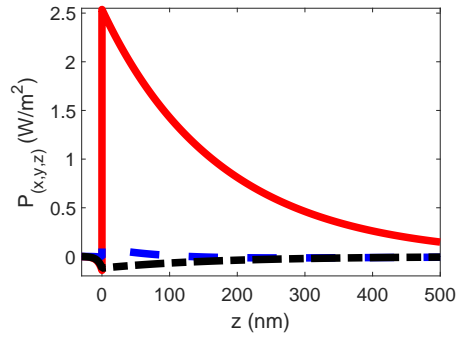


Figure 5.3: Magnitudes of the three Cartesian components of power density of the SPP wave when $\chi = 75^\circ$, $\gamma = (0.3 + 0.003i)\sqrt{\varepsilon_0\mu_0}$, and $q/k_0 = 1.9364 + 0.03306i$. The data were calculated by setting $a_p = 1$ V/m. The other parameters are the same as given in Fig. 5.2. The P_x , P_y , and P_z components are shown by solid red, dashed blue, and chain-dashed black lines, respectively.

dielectric partnering material [25].

5.3 Prism-Coupled Configurations

The prism coupling available for the SPP-waves excitation are of two types. The general schematic of the prism coupling is presented in Fig. 5.4. A prism of high refractive index is affixed to two layers of materials \mathcal{A} and \mathcal{B} . In the prism coupling [27, 28], the layer \mathcal{A} adjacent to the prism is metallic and the layer \mathcal{B} is the uniaxially chiral, bianisotropic material. In the Turbadar–Otto configuration [27, 29], layer \mathcal{A} is the uniaxially chiral, bianisotropic material and layer \mathcal{B} is metallic. In the following, the formulation is presented that is valid for both the configurations.

Let me choose the half-space (prism) $z \leq 0$ as the incidence half-space filled up by a homogeneous medium of high refractive index n_p . The region $0 \leq z \leq L_{\mathcal{A}}$ is occupied by the homogeneous material \mathcal{A} . The region $L_{\mathcal{A}} \leq z \leq L_{\Sigma} = L_{\mathcal{A}} + L_{\mathcal{B}}$ is occupied by another homogeneous material \mathcal{B} and the half-space $z \geq L_{\Sigma}$ is the transmission half-space filled up by the isotropic homogeneous dielectric material with refractive index n_t .

Let me consider a planewave propagation in the half-space $z \leq 0$ making an angle $\theta \in [0, \pi/2)$ to the z -axis, be incident at the interface $z = 0$. The incidence plane is xz plane, which is also the morphologically significant plane of the bianisotropic material occupying either layer \mathcal{A} or \mathcal{B} . This can excite the SPP wave parallel to \hat{u}_x in xy plane. The formulation of this problem is presented in Sec. 3.2 and is not repeated here.

The SPP-waves excitation in the prism-coupled configurations is discerned from the absorptance spectra by identifying the absorptance peaks that do not change with the change in the thickness of the partnering bianisotropic material. In the next section, I present the numerical results of the two prism couplings.

For all the illustrative numerical results in this section, the wavelength was assumed as $\lambda_0 = 633$ nm and the partnering plasmonic material was chosen to be aluminum, just as in the previous section for the canonical problem. Furthermore,

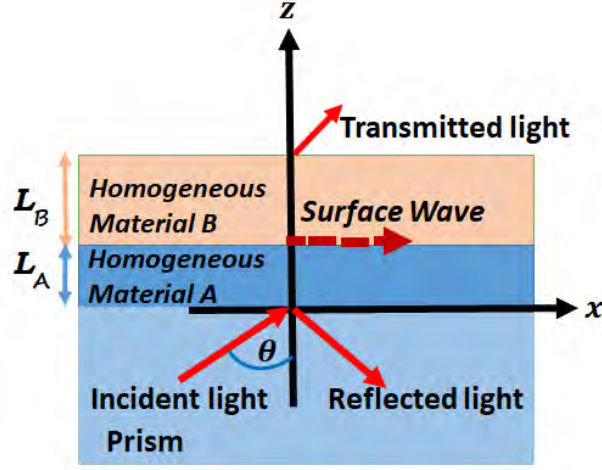


Figure 5.4: The schematic of the prism coupling for the SPP-waves excitation is shown.

the prism was taken with refractive index $N_p = 2.6$, and the transmission medium was considered to be vacuum with $n_t = 1$.

5.3.1 TKR configuration

For the TKR configuration, the formulation can be used by taking material \mathcal{A} as aluminum with $\epsilon_{met}^{\mathcal{A}} = -56 + 21i$ of thickness $L_{\mathcal{A}} = 15$ nm, and material \mathcal{B} as the uniaxially chiral, bianisotropic medium with $\epsilon_a^{\mathcal{B}} = 2.3 + 0.023i$, $\epsilon_b^{\mathcal{B}} = 3.7 + 0.037i$, $\mu_a^{\mathcal{B}} = 0.8 + 0.008i$, $\mu_b^{\mathcal{B}} = 1 + 0.01i$, and $\gamma^{\mathcal{B}} = (0.3 + 0.003i)\sqrt{\epsilon_0\mu_0}$ [8, 9] and thickness $L_{\mathcal{B}} = 400$ nm.

The absorptance spectra against the incidence angle θ and tilt angle χ for p -polarized and s -polarized incidence is shown in Figure 5.5(a,b). The absorptance band in Fig. 5.5(a) starting at $\chi = 90^\circ$ and $\theta \sim 48.7^\circ$ found to be independent of the thickness of the partnering bianisotropic material $L_{\mathcal{B}}$. Therefore, this band represents the SPP-waves excitation since the wavenumber $\kappa \sim 1.9k_0$ closely matched the real

part of relative wavenumber $\text{Re}(q/k_0) \sim 1.9$ when $\chi \in (60^\circ, 90^\circ)$. Furthermore, a comparison of Figs. 5.2 and 5.5(a) show that the SPP waves exist only in a finite range of χ as predicted by the canonical problem. The absence of any absorptance band in Fig. 5.5(b) affirms that the SPP wave has not been excited by the s -polarized incident planewave.

The excitation of the SPP wave at the band identified in Fig. 5.5(a) was further confirmed by the examination of the spatial variations of the three components $P_x(z)$, $P_y(z)$, and $P_z(z)$ of power density as presented in Fig. 5.6 for a representative value of χ and θ . The figure shows the strong confinement of the SPP waves to the interface. The power flow is predominantly along the unit vector \hat{u}_x , and the predominantly p -polarized nature of the SPP wave was deduced from the field profiles (not shown here).

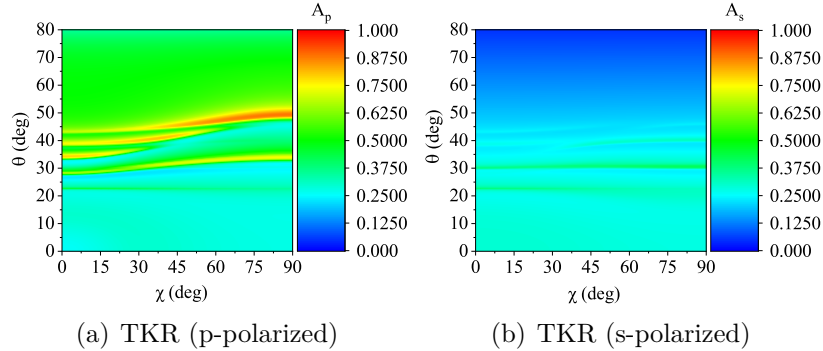


Figure 5.5: Absorptances plotted against the incidence angle θ and tilt angle χ in the TKR configuration. The absorptances for the TKR configuration are given for (a) p -polarized incident electromagnetic wave and (b) s -polarized incident wave when $n_p = 2.6$, $n_t = 1$, $L_A = 15$ nm, $\varepsilon_{met}^A = -56 + 21i$, $L_B = 400$ nm, $\varepsilon_a^B = 2.3 + 0.023i$, $\varepsilon_b^B = 3.7 + 0.037i$, $\mu_a^B = 0.8 + 0.008i$, $\mu_b^B = 1 + 0.01i$, and $\gamma^B = (0.3 + 0.003i)\sqrt{\varepsilon_0\mu_0}$.

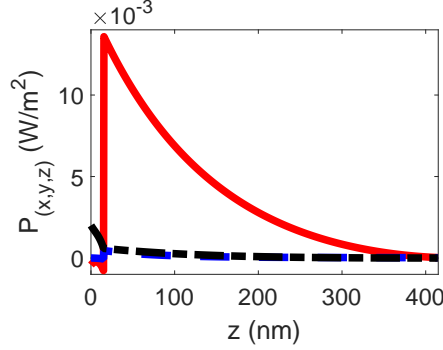


Figure 5.6: Magnitudes of the three Cartesian components of the power density in the TKR configuration vs. z when $\theta = 48.7^\circ$ and $\chi = 75^\circ$. The other parameters are $n_p = 2.6$, $n_t = 1$, $L_A = 15$ nm, $L_B = 400$ nm, $\varepsilon_{met}^A = -56 + 21i$, $\varepsilon_a^B = 2.3 + 0.023i$, $\varepsilon_b^B = 3.7 + 0.037i$, $\mu_a^B = 0.8 + 0.008i$, $\mu_b^B = 1 + 0.01i$, and $\gamma^B = (0.3 + 0.003i)\sqrt{\varepsilon_0\mu_0}$ for p -polarized incidence. The components P_x , P_y , and P_z are shown by solid red, dashed blue, and chain-dashed black lines, respectively.

5.3.2 Turbadar–Otto configuration

The Turbadar–Otto configuration is an alternative prism coupling technique where the dielectric material is sandwiched between the metallic layer and the prism. The theoretical formulation developed in Sec. 3.2 can be used by taking the material \mathcal{A} as the uniaxially chiral, bianisotropic material with $\varepsilon_a^A = 2.3 + 0.023i$, $\varepsilon_b^A = 3.7 + 0.037i$, $\mu_a^A = 0.8 + 0.008i$, $\mu_b^A = 1 + 0.01i$, $\gamma^A = (0.3 + 0.003i)\sqrt{\varepsilon_0\mu_0}$ [8,9], and $L_A = 400$ nm. Material \mathcal{B} is taken as aluminum with $\varepsilon_{met}^B = -56 + 21i$, and thickness $L_B = 30$ nm.

To delineate the SPP-waves excitation, the absorptance spectra as a function of the θ_{inc} and the tilt angle are presented in Figure 5.7(a,b) for p -polarized and s -polarized incident planewave, respectively. The figures show an absorptance band in the spectrum of A_p but multiple absorptance bands in the spectrum of A_s . The angular location of the absorptance band in the spectrum of A_p at $\theta \sim 47.8^\circ$ agrees with the solution of the canonical problem for incident planewave (p -polarized), since the wavenumber $\kappa \sim 1.9k_0$ matches with the $\text{Re}(q/k_0) \sim 1.9$ found by the canonical problem. Furthermore, this band was found to be independent of thickness L_A . Therefore, this band represents the SPP-waves excitation. However, all the bands

in the spectrum of A_s were dependent upon the thickness of bianisotropic material and cannot represent the SPP waves but represent excitation of waveguide modes. To further confirm this, the three Cartesian components of power density are shown in Fig. 5.8 at a selected value of θ and χ for p -polarized incident light and in Fig. 5.9 for s -polarized incidence. The figures show that the p -polarized planewave indeed excites the SPP wave at the chosen value of χ and θ at the absorptance band, whereas s -polarized incidence excited a waveguide mode.

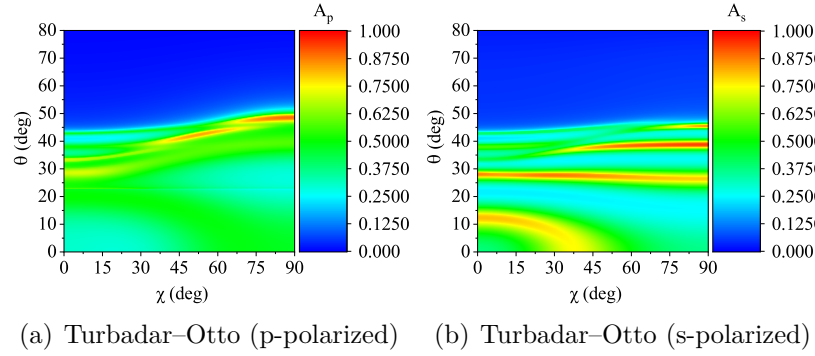


Figure 5.7: Absorptances plotted against the incidence angle θ and tilt angle χ in the Turbadar-Otto configuration for (a) p -polarized incident electromagnetic wave and (b) s -polarized incidence when $n_p = 2.6$, $n_t = 1$, $L_A = 400$ nm, $L_B = 30$ nm, $\varepsilon_a^A = 2.3 + 0.023i$, $\varepsilon_b^A = 3.7 + 0.037i$, $\mu_a^A = 0.8 + 0.008i$, $\mu_b^A = 1 + 0.01i$, $\gamma^A = (0.3 + 0.003i)\sqrt{\varepsilon_0\mu_0}$, and $\varepsilon_{met}^B = -56 + 21i$.

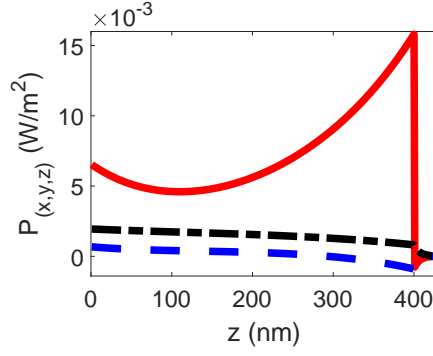


Figure 5.8: The components of power density in the Turbadar–Otto configuration when $\theta = 47.8^\circ$ and $\chi = 75^\circ$ for p -polarized incidence when $n_p = 2.6$, $n_t = 1$, $L_{\mathcal{A}} = 400$ nm, $L_{\mathcal{B}} = 30$ nm, $\varepsilon_a^{\mathcal{A}} = 2.3 + 0.023i$, $\varepsilon_b^{\mathcal{A}} = 3.7 + 0.037i$ and $\mu_a^{\mathcal{A}} = 0.8 + 0.008i$, $\mu_b^{\mathcal{A}} = 1 + 0.01i$, $\gamma^{\mathcal{A}} = (0.3 + 0.003i)\sqrt{\varepsilon_0\mu_0}$, and $\varepsilon_{met}^{\mathcal{B}} = -56 + 21i$. The components P_x , P_y , and P_z are shown by solid red, dashed blue, and chain-dashed black lines, respectively.

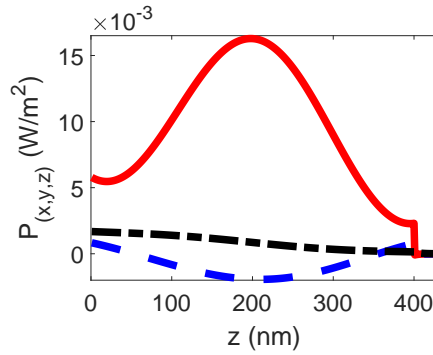


Figure 5.9: Same as Fig. 5.8 except that the planewave is s -polarized when $\theta = 45.1^\circ$.

5.4 Conclusions

The excitation and SPP-wave propagation along the planar interface of a uniaxially chiral, bianisotropic material and a plasmonic material were established for the case when the optic axis of the bianisotropic medium was oriented along an arbitrary angle with the interface plane. However, the propagation direction was restricted in the morphologically significant plane of the bianisotropic material. The canonical problem was solved to find the wavenumbers of the possible SPP waves as a function of the tilt angle of the helixes for several values of the chirality parameter and a threshold value was found for the SPP waves to exist for all tilt angles. It was found that the chirality parameter of the bianisotropic material had to have a magnitude smaller than a threshold for the SPP waves to exist for all tilt angles. The SPP-waves excitation in the TKR and the Turbadar–Otto configurations showed that the p -polarized incidence could excite the SPP waves, but the s -polarized incidence could not.

References

- [1] A. Lakhtakia, V. K. Varadan, and V. V. Varadan, *Time-harmonic electromagnetic fields in chiral media*, Springer-Verlag (1989).
- [2] J. C. Monzon, “Radiation and scattering in homogeneous general biisotropic regions,” *IEEE Trans. Antennas Propagat.* **38**, 227–235 (1990).
- [3] A. H. Sihvola and I. V. Lindell, “Bi-isotropic constitutive relations,” *Microw. and Opt. Technol. Lett.* **4**, 295–297 (1991).
- [4] A. Lakhtakia, *Beltrami Fields in Chiral Media*, World Scientific (1994).
- [5] A. Lakhtakia, “Axial propagation in general helicoidal bianisotropic media,” *Microw. Opt. Technol. Lett.* **6**, 804–806 (1993).
- [6] I. V. Lindell and A. J. Viitanen, “Planewave propagation in uniaxial bianisotropic medium,” *Electron. Lett.* **29**, 150–152 (1993).
- [7] I. V. Lindell, A. J. Viitanen, and P. K. Koivisto, “Plane-wave propagation in a transversely bianisotropic uniaxial medium,” *Microw. Opt. Technol. Lett.* **6**, 478–481 (1993).
- [8] C. Y. Chung and K. W. Whites, “Effective constitutive parameters for an artificial uniaxial bianisotropic chiral medium,” *J. Electromagn. Waves Appl.* **10**, 1363–1388 (1996).

- [9] K. W. Whites and C. Y. Chung, "Composite uniaxial bianisotropic chiral materials characterization: comparison of predicted and measured scattering," *J. Electromagn. Waves Appl.* **11**, 371–394 (1997).
- [10] S. A. Tretyakov and A. A. Sochava, "Novel uniaxial bianisotropic materials: reflection and transmission in planar structures," *Prog. Electromagn. Res.* **9**, 157–179 (1994).
- [11] I. P. Theron and J. H. Cloete, "The optical activity of an artificial non-magnetic uniaxial chiral crystal at microwave frequencies," *J. Electromagn. Waves Appl.* **10**, 539–561 (1996).
- [12] I. Tinoco Jr. and M. P. Freeman, "The optical activity of oriented copper helices. I. Experimental," *J. Phys. Chem.* **61**, 1196–1200 (1957).
- [13] M. M. I. Saadoun and N. Engheta, "A reciprocal phase shifter using novel pseudo-chiral or Ω medium," *Microw. Opt. Technol. Lett.* **5**, 184–188 (1992).
- [14] P. Koivisto, "Polarization properties of plane waves in transversely bianisotropic uniaxial medium," *Microw. Opt. Technol. Lett.* **6**, 858–862 (1993).
- [15] A. J. Viitanen and I. V. Lindell, "Uniaxial chiral quarter-wave polarisation transformer," *Electron. Lett.* **29**, 1074–1075 (1993).
- [16] I. V. Lindell and A. H. Sihvola, "Plane-wave reflection from uniaxial chiral interface and its application to polarization transformation," *IEEE Trans. Antennas Propagat.* **43**, 1397–1404 (1995).
- [17] S. A. Tretyakov and A. A. Sochava, "Proposed composite material for nonreflecting shields and antenna radomes," *Electron. Lett.* **29**, 1048–1049 (1993).
- [18] C. R. B.-Taylor, "Modelling of helix-loaded chiral radar-absorbing layers," *Proc. of Chiral'94*, 83–88 (1994).

- [19] R. E. Raab and J. H. Cloete, “An eigenvalue theory of circular birefringence and dichroism in a non-magnetic chiral medium,” *J. Electromagn. Waves Appl.* **8**, 1073–1089 (1994).
- [20] M. Faryad, “Surface plasmon-polariton waves guided by reciprocal, uniaxially chiral, bianisotropic material,” in: Plasmonics: Design, Materials, Fabrication, Characterization, and Applications XVII, D. P. Tsai and T. Tanaka, eds., *Proc. SPIE*. **11082**, 60–66 (2019).
- [21] M. Naheed and M. Faryad, “Excitation of surface plasmon-polariton waves in the prism-coupled configurations guided by reciprocal, uniaxially chiral, bianisotropic material,” *Opt. Commun.* **465**, 125611 (2020).
- [22] F. Abbas, Q. A. Naqvi, and M. Faryad, “Multiple surface plasmon–polariton waves guided by the interface of a metal and a periodically nonhomogeneous magnetic material,” *Opt. Commun.* **332**, 109–113 (2014).
- [23] M. Faryad, J. A. Polo Jr., and A. Lakhtakia, “Multiple trains of same-color surface plasmon-polaritons guided by the planar interface of a metal and a sculptured nematic thin film. Part IV: Canonical problem,” *J. Nanophotonics* **4**, 043505 (2010).
- [24] A. Lakhtakia and R. Messier, *Sculptured Thin Films: Nanoengineered Morphology and Optics*, SPIE. Press (2005).
- [25] J. A. Polo Jr., T. G. Mackay, and A. Lakhtakia, *Electromagnetic Surface Waves: A Modern Perspective*, Elsevier (2013).
- [26] J. A. Polo Jr. and A. Lakhtakia, “On the surface plasmon polariton wave at the planar interface of a metal and a chiral sculptured thin film,” *Proc. R. Soc. A* **465**, 87–107 (2009).
- [27] T. Turbadar, “Complete absorption of light by thin metal films,” *Proc. Phys. Soc.* **73**, 40–44 (1959).

- [28] E. Kretschmann and H. Raether, “Radiative decay of non radiative surface plasmons excited by light,” *Z. Naturforsch.* **23**, 2135–2136 (1968).
- [29] A. Otto, “Excitation of nonradiative surface plasma waves in silver by the method of frustrated total reflection,” *Z. Phys. A* **216**, 398–410 (1968).

Chapter 6

Conclusions and Future Work

6.1 Conclusions

The objectives of the research conducted for this thesis, as was stated in Chap. 1, were to:

1. find the fundamental properties of the partnering chiral materials that are responsible for the propagation and the excitation of surface waves;
2. to identify the parametric ranges of chirality of these partnering chiral materials that support the excitation of surface waves;
3. study the SPP-waves excitation in both the prism coupled experimental setups with partnering isotropic chiral and bianisotropic chiral materials;
4. the effects of morphology of the partnering uniaxially chiral bianisotropic materials on the characteristics of the SPP waves;
5. to find out the parametric conditions for the hybrid polarized SPP waves supported by these chiral materials.

To achieve these objectives, the propagation and excitation of the surface electromagnetic waves propagating along the interfaces of two dissimilar homogeneous materials were theoretically studied. The SPP-waves excitation with chiral materials

was extensively studied. The three canonical boundary-value problems and the four prism-coupled problems each in two configurations were investigated to find out the solutions for the surface electromagnetic waves. The excitation of the SPP waves in both the TKR and the Turbadar–Otto prism-coupled configurations was also studied, taking into the effects of the chirality parameter and anisotropy.

In Chap. 2, the numerical solution of the canonical boundary-value problem showed the propagation of surface electromagnetic waves supported by the planar interface of two isotropic chiral composite materials with complex constitutive parametric ranges. When one component material of the isotropic chiral composite material was taken as a dissipative dielectric material interfaced with another isotropic chiral composite material, the surface waves supported by the interface could be considered similar to Uller–Zenneck waves. Furthermore, when one component material of any partnering isotropic chiral composite material was plasmonic, the propagation of the SPP waves was supported by the interface. Moreover, the SPP-waves excitation was shown at the planar interface of a plasmonic material and the isotropic chiral material in Chap. 3, in both the TKR and Turbadar–Otto prism-coupled configurations. The SPP-waves excitation was shown to exist from the appearance of the peaks in the absorptance spectrum. These peaks were found independent of the thickness of the partnered materials. Also, the excitation of the SPP waves was verified by the power profiles. It was shown that the SPP waves could only be excited by the p -polarized incident planewave and not by the s -polarized planewave. However, the SPP wave could exist only when the chirality pseudoscalar was smaller than a threshold value. This finding can be helpful in the design of plasmonic switches.

The SPP-wave excitation at the planar interface of a non-magnetic uniaxially chiral, bianisotropic material and a plasmonic material was studied in Chap. 4. The formulation and representative numerical results of both the prism-coupled configurations were presented. Moreover, the numerical results were also presented for the SPP waves in the canonical boundary-value problem. In the TKR configuration, only p -polarized incident planewave could excite the SPP wave, but in the Turbadar–Otto

configuration, both the p - and s -polarized planewaves could excite the SPP waves. However, only p -polarized planewave could excite the SPP wave when the complex-valued chirality parameter was small, and only s -polarized incident planewave could excite the SPP wave when the complex-valued chirality parameter was large. Moreover, the SPP wave could also be excited that was neither s - nor p -polarized.

The above-stated findings were followed by an investigation of the excitation of the SPP wave at the interface of a plasmonic material and an obliquely-mounted uniaxially chiral, bianisotropic material with an optic axis making an arbitrary angle with the interface plane in Chap. 5. The canonical boundary-value problem was solved to investigate the wavenumbers of the possible SPP waves as a function of the tilt angle of the helixes for several values of the chirality parameter. The direction of propagation of the SPP wave was confined to be in the morphologically significant plane of the bianisotropic material. However, it was found that the complex-valued chirality parameter had to have a magnitude smaller than a threshold value for the SPP wave to exist for all the tilt angles of helixes. Secondly, the SPP-wave excitation in the TKR and the Turbadar–Otto configurations showed that only the p -polarized incident planewave could excite the SPP wave but not the s -polarized incidence for an obliquely mounted, uniaxially chiral, bianisotropic material.

In summary, the following conclusions were inferred:

1. The planar interface of two different isotropic chiral materials can support the surface waves for specific parametric ranges and can simultaneously support the amplification and attenuation of the surface electromagnetic waves.
2. The threshold value for the complex-valued chirality exists for the excitation of the surface electromagnetic waves.
3. The p -polarized incident planewave can support the SPP-waves excitation in both the TKR and the Turbadar–Otto prism-coupled configurations. However, the s -polarized incident planewave can support the SPP-waves excitation in the Turbadar–Otto configuration.

4. The morphology of the chiral materials affects the threshold value for the excitation of SPP waves.
5. The SPP waves that are neither s - nor p -polarized can exist for the large values of the complex-valued chirality parameter.

These findings relate to the objectives (1)-(5) in the same order.

6.2 Future Work

This thesis lays down the foundation for work on the surface electromagnetic waves guided by the interfaces with the chiral materials. In particular, I propose the following work.

- The design of optical sensors to sense chirality parameter of these materials and use them in applications of the SPP waves.
- The presence of threshold value of the chirality in both the isotropic and bianisotropic chiral media for the existence of the SPP waves can be used to design plasmonic switches.
- The methodology can be used to set up the canonical and the prism-coupled problems to investigate the SPP waves guided by more complex materials.
- The excitation and propagation of the SPP waves with chiral materials can be studied in the grating-coupled and waveguide-coupled configurations for integrated optical components.
- The possibility of multiple surface waves can be investigated by making the chiral materials periodically nonhomogeneous.

Appendix A

Metal and Columnar Thin Film

If the chirality pseudoscalar of the chiral uniaxial bianisotropic material is made zero, then the medium exhibits the properties of the simple uniaxial dielectric material. The work reported in this Appendix is meant to be an aiding prologue for grasping a good understanding of the behavior of the uniaxial bianisotropic materials. In this work, the study of the SPP-waves excitation with columnar thin films (CTFs) in both the TKR and Otto configurations is presented. The CTFs generalize uniaxial dielectric materials since CTFs are biaxial. This Appendix presents a comparison of the excitation of the SPP waves using the two possible prism couplings. This Appendix is planned as follows: The introduction and related literature review is given in Sec. A.1. The illustrative numerical results are discussed and presented in Sec. A.2. The conclusions are given in Sec. A.3.

A.1 Introduction

There are two types of prism-coupled configurations to excite the SPP waves using evanescent waves: (i) The TKR configuration [1, 2] and (ii) the Turbadar–Otto configuration [2, 3]. The TKR configuration, as shown in Fig. A.1, is very popular in exciting the SPP waves because of its easier adaptation to optical sensing of fluids that replaces the partnering dielectric material or infiltrates it. In this technique, the

The work reported in this appendix is published in: *J. Nanophoton.* **13**, 036001 (2019).

prism is coupled to a thick dielectric material through a very thin metal layer [4]. In the Turbadar–Otto prism coupling, the dielectric partnering material is sandwiched between the metallic film and the prism as shown in Fig. A.2. The generation of the evanescent waves in the Turbadar–Otto prism coupling requires a thinner dielectric layer. A comparison of the TKR and the Turbadar–Otto configurations for an isotropic dielectric material shows that the latter offers a clearer and easier identification of the reflectance dips than the former for the identification of the SPP-waves excitation.

The columnar thin films (CTFs) are porous films of columnar morphology with all columns parallel to a straight line [5]. These films are normally deposited using the physical vapor deposition technique by directing a vapor flux at a substrate at an oblique angle [6]. The SPP-waves excitation at the interface of a plasmonic material and a CTF in the TKR configuration [7, 8] has been studied for designing plasmonic optical sensors [9, 10] since the CTFs are the porous anisotropic films with a permittivity dyadic that depends on the fluid infiltrating the vacant spaces in the CTF. The anisotropic porous dielectric partnering materials, such as the CTF, can sometime have advantages over isotropic dielectric partnering materials when it comes to optical sensing. For example, the sensitivity can be enhanced significantly by infiltrating the anisotropic partnering material with metallic particles [11] or by making the anisotropic partnering material as a hyperbolic medium [12]. The alternative to the TKR is the Turbadar–Otto configuration, which is the focus of this work. Does the Turbadar–Otto configuration offer any advantage over the TKR when the anisotropic dielectric materials are used? The research reported in this Appendix was endeavored to answer this question.

The TKR configuration is advantageous to the Turbadar–Otto configuration when sensing liquids since the homogeneous infiltration of the not-very-thick CTF would be very difficult in the Turbadar–Otto configuration because of the capillary forces if the infiltration has to be done from the sides. However, for the gases, this problem will not be present. So, the Turbadar–Otto configuration discussed here will be more

amenable to implementation for the sensing of the gases than the liquids. For the liquids, an experimental strategy will have to be developed for easier and homogeneous infiltration of the CTF.

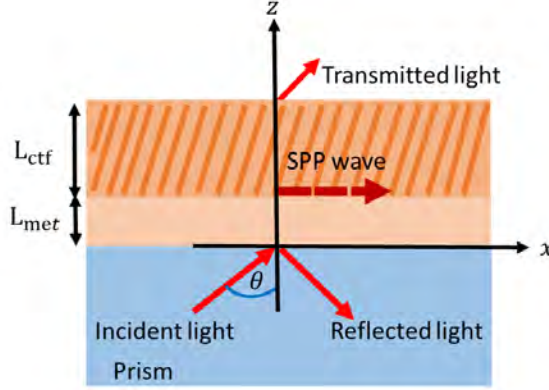


Figure A.1: The schematic of the TKR configuration is shown. A linearly polarized electromagnetic wave is incident at the metal-CTF bilayer. The CTF is infiltrated by a fluid of which the refractive index is to be sensed.

A.2 Results and Discussion

A.2.1 Problem description

Consider the geometry of the problem for the Turbadar–Otto configuration as depicted in Fig. A.2. The half-space $z \leq 0$ is filled up by an unbounded isotropic homogeneous dielectric material (prism) with a refractive index n_p . The region $0 \leq z \leq L_{ctf}$ is occupied by a CTF with permittivity dyadic given by

$$\underline{\underline{\varepsilon}}_{ctf} = \varepsilon_0 \underline{\underline{S}}_y \cdot (\varepsilon_a \hat{u}_z \hat{u}_z + \varepsilon_b \hat{u}_x \hat{u}_x + \varepsilon_c \hat{u}_y \hat{u}_y) \cdot \underline{\underline{S}}_y^{-1} \quad (\text{A.2.1})$$

where ε_a , ε_b , and ε_c are the relative permittivity scalars, and

$$\underline{\underline{S}}_y = \cos \chi (\hat{u}_x \hat{u}_x + \hat{u}_z \hat{u}_z) + \sin \chi (\hat{u}_z \hat{u}_x - \hat{u}_x \hat{u}_z) + \hat{u}_y \hat{u}_y \quad (\text{A.2.2})$$

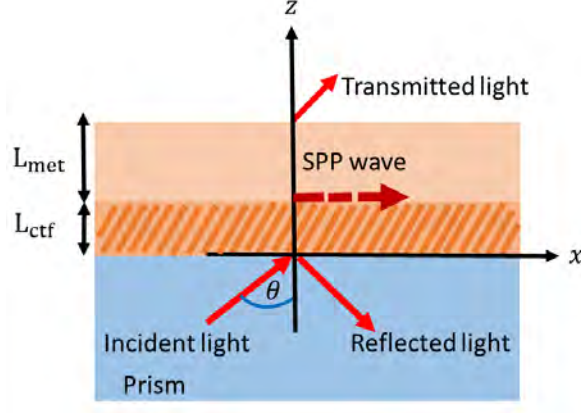


Figure A.2: The schematic of the Turbadar–Otto configuration is shown. A linearly polarized electromagnetic wave is incident at the CTF-metal bilayer from the CTF side.

represents the rotation in the xz plane around the y axis, and the principal relative permittivity scalars are chosen for a CTF made of titanium oxide, with \hat{u}_x , \hat{u}_y , and \hat{u}_z representing the unit vectors in the Cartesian coordinate system. The relative permittivity scalars for the uninfiltated CTF are taken to be that of titanium oxide as [13]

$$\left. \begin{aligned} \varepsilon_a &= [1.0443 + 2.7394v - 1.3697v^2]^2 \\ \varepsilon_b &= [1.6765 + 1.5649v - 0.7825v^2]^2 \\ \varepsilon_c &= [1.3586 + 2.1109v - 1.0554v^2]^2 \end{aligned} \right\} \quad (\text{A.2.3})$$

with

$$\left. \begin{aligned} v &= 2\chi_v/\pi \\ \chi &= \tan^{-1}[2.8818 \tan \chi_v] \end{aligned} \right\}, \quad (\text{A.2.4})$$

where $\chi_v \in [0, \pi/2)$ is the angle of projection of physical vapors with the substrate. The inclination of the nano-columns of the CTF with the substrate is denoted by χ . The morphologically significant plane is taken as the xz plane for the CTF and the incident electromagnetic wave is directed at an angle $\theta \in [0, \pi/2)$ to the z axis.

The region $L_{ctf} \leq z \leq L_{ctf} + L_{met}$ is occupied by a plasmonic material with ε_m as relative permittivity, and the half-space $z \geq L_{ctf} + L_{met}$ is again filled up by the same unbounded isotropic homogeneous dielectric material as that of the prism. Correspondingly, the characterization of the homogeneous anisotropic non-magnetic CTF is given by the constitutive relations in the frequency-domain as follows

$$\left. \begin{aligned} \underline{D}(\underline{r}, \omega) &= \underline{\varepsilon}_{ctf} \cdot \underline{E}(\underline{r}, \omega) \\ \underline{B}(\underline{r}, \omega) &= \mu_0 \underline{H}(\underline{r}, \omega) \end{aligned} \right\}, \quad (\text{A.2.5})$$

where $\underline{\varepsilon}_{ctf}$ is the permittivity dyadic of the CTF. The homogeneous isotropic non-magnetic plasmonic material is characterized by the following constitutive relations in the frequency domain as follows,

$$\left. \begin{aligned} \underline{D}(\underline{r}, \omega) &= \varepsilon_0 \varepsilon_m \underline{E}(\underline{r}, \omega) \\ \underline{B}(\underline{r}, \omega) &= \mu_0 \underline{H}(\underline{r}, \omega) \end{aligned} \right\}, \quad (\text{A.2.6})$$

and is specified only by its complex-valued relative permittivity ε_m .

The formulation of the canonical problem of planewave reflection and transmission is as follows. Let me consider a planewave propagating in the half-space $z \leq 0$ at an angle $\theta \in [0, \pi/2)$ with the z axis in the xz plane, and making an angle ψ with the x axis in the xy plane; be incident at the interface $z = 0$. This will excite the SPP wave propagating along the unit vector $\hat{u}_1 = \cos \psi \hat{u}_x + \sin \psi \hat{u}_y$ in the interface plane. The unit vector perpendicular to \hat{u}_1 and \hat{u}_z is given by $\hat{u}_2 = -\sin \psi \hat{u}_x + \cos \psi \hat{u}_y$. The incident, reflected, and transmitted electric field phasors of a planewave are derived as,

$$\left. \begin{aligned} \underline{E}_{inc}(\underline{r}) &= \left(a_s \underline{s} + a_p \underline{p}_+ \right) \exp[i(\hat{u}_1 \kappa + \hat{u}_z k_0 n_p \cos \theta) \cdot \underline{r}], z \leq 0 \\ \underline{E}_{ref}(\underline{r}) &= \left(r_s \underline{s} + r_p \underline{p}_- \right) \exp[i(\hat{u}_1 \kappa - \hat{u}_z k_0 n_p \cos \theta) \cdot \underline{r}], z \leq 0 \\ \underline{E}_{tr}(\underline{r}) &= \left(t_s \underline{s} + t_p \underline{p}_+ \right) \exp[i(\hat{u}_1 \kappa + \hat{u}_z k_0 n_p \cos \theta) \cdot (\underline{r} - \hat{u}_z L_\Sigma)], z \geq L_\Sigma \end{aligned} \right\}, \quad (\text{A.2.7})$$

where $L_{ctf} + L_{met} = L_\Sigma$, $\kappa = k_0 n_p \sin \theta$, $\underline{s} = \hat{u}_2$, $\underline{p}_+ = -\hat{u}_1 \cos \theta + \hat{u}_z \sin \theta$, and $\underline{p}_- = \hat{u}_1 \cos \theta + \hat{u}_z \sin \theta$; a_s and a_p represent the scalar amplitudes of the s - and p -polarized

components of the incident planewave, r_s and r_p are the reflection coefficients and the transmission coefficients are denoted by t_s and t_p . The boundary-value problem is solved to determine the reflection and the transmission coefficients in terms of a_s and a_p . The corresponding incident, reflected, and transmitted magnetic field phasors of a planewave are derived from Maxwell's curl postulates as follows,

$$\left. \begin{aligned} \underline{H}_{inc}(\underline{r}) &= \frac{n_p}{\eta_0} \left(a_s \underline{p}_+ - a_p \underline{s} \right) \exp[i(\hat{u}_1 \kappa + \hat{u}_z k_0 n_p \cos \theta) \cdot \underline{r}], z \leq 0 \\ \underline{H}_{ref}(\underline{r}) &= \frac{n_p}{\eta_0} \left(r_s \underline{p}_- - r_p \underline{s} \right) \exp[i(\hat{u}_1 \kappa - \hat{u}_z k_0 n_p \cos \theta) \cdot \underline{r}], z \leq 0 \\ \underline{H}_{tr}(\underline{r}) &= \frac{n_p}{\eta_0} \left(t_s \underline{p}_+ - t_p \underline{s} \right) \exp[i(\hat{u}_1 \kappa + \hat{u}_z k_0 n_p \cos \theta) \cdot (\underline{r} - \hat{u}_z L_\Sigma)], z \geq L_\Sigma \end{aligned} \right\}. \quad (\text{A.2.8})$$

The electromagnetic fields in the region $0 \leq z \leq L_\Sigma$ are represented in phasor form as,

$$\left. \begin{aligned} \underline{E}(\underline{r}) &= \underline{e}(z) \exp(i\kappa \hat{u}_1 \cdot \underline{r}) \\ \underline{H}(\underline{r}) &= \underline{h}(z) \exp(i\kappa \hat{u}_1 \cdot \underline{r}) \end{aligned} \right\}, \quad 0 \leq z \leq L_\Sigma. \quad (\text{A.2.9})$$

Substitution of Eqs. (A.2.6) and (A.2.9) in Maxwell curl postulates, i.e.,

$$\left. \begin{aligned} \nabla \times \underline{E}(\underline{r}, \omega) &= i\omega \underline{B}(\underline{r}, \omega) \\ \nabla \times \underline{H}(\underline{r}, \omega) &= -i\omega \underline{D}(\underline{r}, \omega) \end{aligned} \right\}, \quad (\text{A.2.10})$$

results in the two algebraic equations as follows,

$$\left. \begin{aligned} e_{zm}(z) &= -\frac{\kappa}{\omega \epsilon_0 \epsilon_m(z)} [h_y(z) \cos \psi - h_x(z) \sin \psi] \\ h_{zm}(z) &= \frac{\kappa}{\omega \mu_0} [e_y(z) \cos \psi - e_x(z) \sin \psi] \end{aligned} \right\}, \quad L_{ctf} < z < L_\Sigma, \quad (\text{A.2.11})$$

and four partial differential equations are also obtained, which can be re-arranged in the matrix ordinary differential equation form (MODE) as,

$$\frac{d}{dz} [\underline{f}(z)] = i[\underline{P}(z)] \cdot [\underline{f}(z)], \quad (\text{A.2.12})$$

where

$$[\underline{f}(z)] = \begin{bmatrix} e_x(z) \\ e_y(z) \\ h_x(z) \\ h_y(z) \end{bmatrix} \quad (\text{A.2.13})$$

and $[\underline{P}(z)]$ is the 4×4 $[\underline{P}_{met}]$ matrix inside the plasmonic medium with

$$\begin{aligned} [\underline{P}_{met}] &= \omega \begin{bmatrix} 0 & 0 & 0 & \mu_0 \\ 0 & 0 & -\mu_0 & 0 \\ 0 & -\varepsilon_0 \varepsilon_m & 0 & 0 \\ \varepsilon_0 \varepsilon_m & 0 & 0 & 0 \end{bmatrix} \\ &+ \frac{\kappa^2}{\omega \varepsilon_0 \varepsilon_m} \begin{bmatrix} 0 & 0 & \cos \psi \sin \psi & -\cos^2 \psi \\ 0 & 0 & \sin^2 \psi & -\cos \psi \sin \psi \\ 0 & 0 & 0 & 0 \\ 0 & 0 & 0 & 0 \end{bmatrix} \\ &+ \frac{\kappa^2}{\omega \mu_0} \begin{bmatrix} 0 & 0 & 0 & 0 \\ 0 & 0 & 0 & 0 \\ -\cos \psi \sin \psi & \cos^2 \psi & 0 & 0 \\ -\sin^2 \psi & \cos \psi \sin \psi & 0 & 0 \end{bmatrix}. \end{aligned} \quad (\text{A.2.14})$$

When Eqs. (A.2.5) and (A.2.9) are substituted in Maxwell curl postulates, i.e., Eq.(A.2.10), for a CTF, the same form, as given in Eq. (A.2.12), is obtained except that the $[\underline{P}(z)]$ matrix is replaced with $[\underline{P}_{ctf}]$ matrix in the CTF with

$$\begin{aligned}
[\underline{P}_{ctf}] = & \omega \begin{bmatrix} 0 & 0 & 0 & \mu_0 \\ 0 & 0 & -\mu_0 & 0 \\ 0 & -\varepsilon_0 \varepsilon_c & 0 & 0 \\ \varepsilon_0 \varepsilon_d & 0 & 0 & 0 \end{bmatrix} \\
& + \kappa \frac{\varepsilon_d [\varepsilon_a - \varepsilon_b]}{\varepsilon_a \varepsilon_b} \sin \chi \cos \chi \begin{bmatrix} \cos \psi & 0 & 0 & 0 \\ \sin \psi & 0 & 0 & 0 \\ 0 & 0 & 0 & 0 \\ 0 & 0 & -\sin \psi & \cos \psi \end{bmatrix} \\
& + \frac{\kappa^2}{\omega \varepsilon_0} \frac{\varepsilon_d}{\varepsilon_a \varepsilon_b} \begin{bmatrix} 0 & 0 & \cos \psi \sin \psi & -\cos^2 \psi \\ 0 & 0 & \sin^2 \psi & -\cos \psi \sin \psi \\ 0 & 0 & 0 & 0 \\ 0 & 0 & 0 & 0 \end{bmatrix} \\
& + \frac{\kappa^2}{\omega \mu_0} \begin{bmatrix} 0 & 0 & 0 & 0 \\ 0 & 0 & 0 & 0 \\ -\cos \psi \sin \psi & \cos^2 \psi & 0 & 0 \\ -\sin^2 \psi & \cos \psi \sin \psi & 0 & 0 \end{bmatrix}, \tag{A.2.15}
\end{aligned}$$

and the two algebraic equations are obtained as follows,

$$\left. \begin{aligned} e_z(z) &= \frac{\varepsilon_d [\varepsilon_a - \varepsilon_b] \sin \chi \cos \chi}{\varepsilon_a \varepsilon_b} e_x(z) + \frac{\kappa}{\omega \varepsilon_0} \frac{\varepsilon_d}{\varepsilon_a \varepsilon_b} [h_x(z) \sin \psi - h_y(z) \cos \psi] \\ h_z(z) &= -\frac{\kappa}{\omega \mu_0} [e_x(z) \sin \psi - e_y(z) \cos \psi] \end{aligned} \right\}, \tag{A.2.16}$$

where

$$\varepsilon_d = \varepsilon_a \varepsilon_b / \varepsilon_a \cos^2 \chi + \varepsilon_b \sin^2 \chi. \tag{A.2.17}$$

The incident and reflected electric field phasors (A.2.7) and the corresponding magnetic field phasors (A.2.8) give

$$[\underline{f}(0-)] = [\underline{K}] \cdot [a_s \ a_p \ r_s \ r_p]^T, \tag{A.2.18}$$

where

$$[\underline{K}] = \begin{bmatrix} -\sin \psi & -\cos \psi \cos \theta & -\sin \psi & \cos \psi \cos \theta \\ \cos \psi & -\sin \psi \cos \theta & \cos \psi & \sin \psi \cos \theta \\ -(\frac{n_p}{\eta_0}) \cos \psi \cos \theta & (\frac{n_p}{\eta_0}) \sin \psi & (\frac{n_p}{\eta_0}) \cos \psi \cos \theta & (\frac{n_p}{\eta_0}) \sin \psi \\ -(\frac{n_p}{\eta_0}) \sin \psi \cos \theta & -(\frac{n_p}{\eta_0}) \cos \psi & (\frac{n_p}{\eta_0}) \sin \psi \cos \theta & -(\frac{n_p}{\eta_0}) \cos \psi \end{bmatrix}. \quad (\text{A.2.19})$$

Similarly, the transmitted electric and magnetic field phasors give

$$[\underline{f}(L_{\Sigma}+)] = [\underline{K}] \cdot [t_s \ t_p \ 0 \ 0]^T. \quad (\text{A.2.20})$$

A.2.2 Turbadar–Otto configuration

The solution of the MODE (A.2.12) in the Turbadar–Otto configuration, results in

$$[\underline{f}(L_{\Sigma}-)] = e^{i[\underline{P}_{met}]L_{met}} \cdot e^{i[\underline{P}_{ctf}]L_{ctf}} \cdot [\underline{f}(0+)]. \quad (\text{A.2.21})$$

Using the standard boundary conditions

$$\left. \begin{aligned} [\underline{f}(0-)] &= [\underline{f}(0+)] \\ [\underline{f}(L_{ctf}-)] &= [\underline{f}(L_{ctf}+)] \\ [\underline{f}(L_{\Sigma}-)] &= [\underline{f}(L_{\Sigma}+)] \end{aligned} \right\} \quad (\text{A.2.22})$$

across the interfaces, i.e., equating the tangential components of electromagnetic field phasors, result in the following equation,

$$\begin{bmatrix} t_s \\ t_p \\ 0 \\ 0 \end{bmatrix} = [\underline{K}]^{-1} \cdot e^{i[\underline{P}_{met}]L_{met}} \cdot e^{i[\underline{P}_{ctf}]L_{ctf}} \cdot [\underline{K}] \cdot \begin{bmatrix} a_s \\ a_p \\ r_s \\ r_p \end{bmatrix}. \quad (\text{A.2.23})$$

The reflection and transmission coefficients can be obtained by simple mathematical manipulation of Eq. (A.2.23). The absorptances can then be determined with the

help of the reflection and transmission coefficients by using,

$$A_s = 1 - \frac{|r_s|^2 + |r_p|^2 + |t_s|^2 + |t_p|^2}{|a_s|^2}, a_p = 0, \quad (\text{A.2.24})$$

for s -polarized incident light, and

$$A_p = 1 - \frac{|r_s|^2 + |r_p|^2 + |t_s|^2 + |t_p|^2}{|a_p|^2}, a_s = 0, \quad (\text{A.2.25})$$

for p -polarized incident light.

A.2.3 Numerical results for Turbadar–Otto configuration

The excitation of surface waves can be discerned from the angular spectrum of planewave absorption. Those peaks in the absorptance spectrum represent the excitation of the SPP waves whose angular location is independent of the thickness of the dielectric partnering materials beyond a threshold thickness. Furthermore, the wavenumber of the incident electromagnetic wave at the angle where the absorption peak is supposed to excite the SPP wave should match the $\text{Re}(q/k_0)$ of the SPP wave that is predicted by the underlying canonical problem. In the canonical problem, both the partnering materials (metal and the CTF in the present case) are assumed to fill up the half-spaces, and the possible SPP waves that can propagate at their planar interface are found.

For the illustrative numerical results in this section, I chose $\varepsilon_m = -56 + 21i$ (aluminum), $\chi_v = 30$ deg, and $\psi = 20$ deg, where $\psi \in [0, 2\pi)$ is the angle between the incidence plane and the morphological significant plane of the CTF (xy plane). The prism material was chosen as zinc selenide with refractive index $n_p = 2.6$. The wavenumber q of the SPP waves can be found by solving the underlying canonical problem [7, 8] for the chosen parameters. For the uninfiltrated CTF, the canonical problem gave $q = (2.0989 + 0.0225i)k_0$.

To see the SPP-waves excitation in the Turbadar–Otto prism coupling, the absorptances were computed and are shown in Fig. A.3 as a function of the θ_{inc} for fixed $L_{met} = 30$ nm but different thicknesses of the CTF for both the p - and s -polarized

incident electromagnetic waves. The figure shows that an absorptance peak is present for all three thicknesses in the absorptance spectrum for the p -polarized incident electromagnetic wave. No absorptance peak is present for the s -polarized incidence. The θ_{peak} (the angular location of the absorptance peak) changes very little with the thickness of the CTF as shown in Table A.1. The component of the wave vector of the electromagnetic wave travelling parallel to the direction of propagation of the SPP wave $\kappa = n_p k_0 \sin \theta_{peak}$ also matches the real part of q . Therefore, the absorptance peak signifies the SPP-wave excitation.

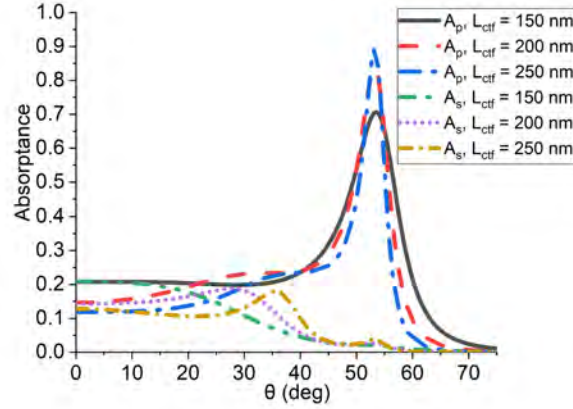


Figure A.3: The absorptances plotted against the incidence angles θ for various thicknesses of the CTF when $\psi = 20$ deg, $\chi_v = 30$ deg, $\lambda_0 = 633$ nm, $L_{met} = 30$ nm, $\epsilon_m = -56 + 21i$, and $n_p = 2.6$. The CTF was chosen to be made of titanium oxide and uninfiltrated.

To further confirm the SPP-waves excitation and the localization to the interface, the spatial variation of the three components of power density

$$\underline{P}(\underline{r}) = \frac{1}{2} \text{Re} [\underline{E}(\underline{r}) \times \underline{H}^*(\underline{r})] , \quad (\text{A.2.26})$$

were examined, where the asterisk delineates the complex conjugate. Figure A.4 shows the strong confinement of the SPP waves to the CTF/metal interface.

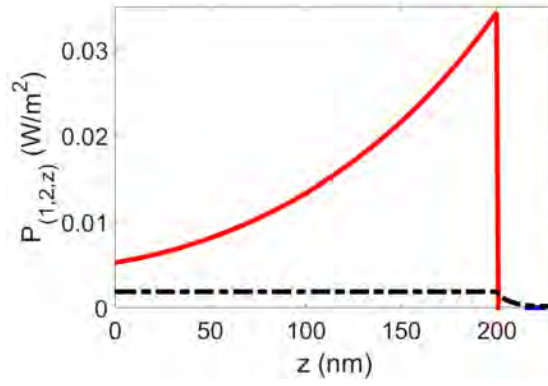


Figure A.4: The magnitudes of the three components of power density $\underline{P}(0, 0, z)$ vs. z in the Turbadar–Otto configuration when p -polarized planewave is incident on the CTF-metal interface at $\theta = 53.2^\circ$, and $L_{ctf} = 200$ nm. The other parameters are the same as given in Fig. A.3. The components parallel to \hat{u}_1 , \hat{u}_2 , and \hat{u}_z , are shown by a solid red line, a dashed blue line, and a chain-dashed black line, respectively.

A.2.4 TKR configuration

The solution of the MODE (A.2.12) in the TKR configuration results in

$$[\underline{f}(L_\Sigma -)] = e^{i[\underline{P}_{ctf}]L_{ctf}} \cdot e^{i[\underline{P}_{met}]L_{met}} \cdot [\underline{f}(0+)]. \quad (\text{A.2.27})$$

Using the standard boundary conditions

$$\left. \begin{aligned} [\underline{f}(0-)] &= [\underline{f}(0+)] \\ [\underline{f}(L_{met}-)] &= [\underline{f}(L_{met}+)] \\ [\underline{f}(L_\Sigma-)] &= [\underline{f}(L_\Sigma+)] \end{aligned} \right\} \quad (\text{A.2.28})$$

across the interfaces, i.e., equating the tangential components of electromagnetic field phasors, result in the following equation,

$$\begin{bmatrix} t_s \\ t_p \\ 0 \\ 0 \end{bmatrix} = [\underline{K}]^{-1} \cdot e^{i[\underline{P}_{ctf}]L_{ctf}} \cdot e^{i[\underline{P}_{met}]L_{met}} \cdot [\underline{K}] \cdot \begin{bmatrix} a_s \\ a_p \\ r_s \\ r_p \end{bmatrix}. \quad (\text{A.2.29})$$

The reflection and transmission coefficients can be obtained by simple mathematical manipulation of Eq. (A.2.29). The absorptances can then be found by using the same Eqs. (A.2.24) and (A.2.25) for s -polarized and p -polarized incident planewaves, respectively.

A.2.5 Comparison with TKR configuration

To compare the excitation in the Turbadar–Otto configuration with the TKR configuration, the absorptances in the TKR configuration are shown in Fig. A.5 for $L_{met} = 15$ nm. The figure shows the SPP-waves excitation for the p -polarized incidence. The values of the incidence angles for all three values of the CTF thickness and the angular location are also provided in Table A.1. The data presented in the table clearly show that full-width at half-maximum (FWHM) of the absorptance peaks indicating the SPP-wave excitation is much smaller for the Turbadar–Otto configuration than for the TKR configuration. Furthermore, the change in the angular location of the absorptance peak is smaller for the Turbadar–Otto than for the TKR configuration when the thickness of the CTF is increased. It is probably due to the minimum dissipation on the incidence side as the incident light is coupled with the anisotropic CTF medium in the Turbadar–Otto configuration, compared to the TKR configuration where the incident light is coupled with the metallic thin film (lossy material). That's why the values of κ are well matched to $\text{Re}(q)$ in Table A.1, but the TKR values of κ are not. The smaller peak width offers clearer identification of the SPP-wave excitation and can help design more sensitive optical sensors using the Turbadar–Otto configuration than the TKR configuration.

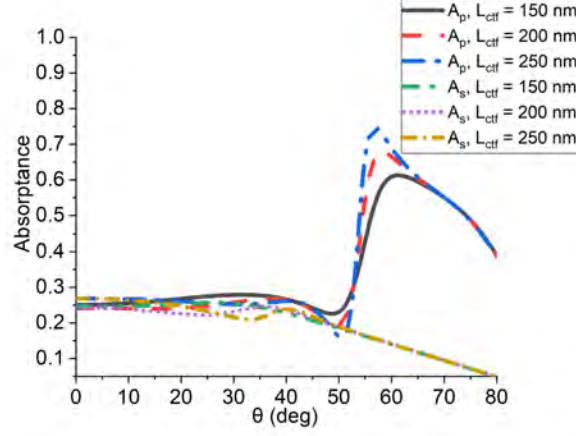


Figure A.5: Same as Fig. A.3 except that the absorbances are computed in TKR configuration for $L_{met} = 15$ nm.

A.2.6 Sensing in the Turbadar–Otto configuration

To demonstrate the optical sensing using the Turbadar–Otto configuration, the absorbance spectra were computed against the refractive index n_ℓ of the fluid infiltrating the vacant spaces of the CTF. The permittivities for the CTF for $n_\ell \neq 1$ were used from Ref. [9] computed from Bruggemann formalism after finding the nanoscale parameters of the CTF from the inverse Bruggemann formalism implemented upon the CTF with $n_\ell = 1$ [6, 14]. The absorbance profiles presented in Fig. A.6 clearly show the potential for sensing of the Turbadar–Otto configuration. Moreover, the absorbance peak showing the SPP-wave excitation clearly remains sharp as n_ℓ increases.

The values of the θ_{peak} where the absorbance peak occurs, are tabulated in Table A.2. Also provided in the table is the sensitivity

$$\rho = \frac{\Delta\theta_{peak}}{\Delta n_\ell}, \quad (\text{A.2.30})$$

where $\Delta\theta_{peak}$ is the shift in the angular location of the peak showing the SPP-waves

Table A.1: The values of the θ_{peak} , FWHM ($\Delta\theta$), and the wavenumber $\kappa = n_p k_0 \sin \theta_{inc}$, are given for different thicknesses of the CTF for the TKR and the Turbadar–Otto configurations. The solution of the underlying canonical problem is $q = (2.0989 + 0.0225i)k_0$.

	TKR ($L_{met} = 15$ nm)			Turbadar–Otto ($L_{met} = 30$ nm)		
L_{ctf} (nm)	θ_{peak} (deg)	FWHM	κ/k_0	θ_{peak} (deg)	FWHM	κ/k_0
150	61.2	30	2.2784	53.5	11.9	2.0901
200	58.3	28.6	2.2121	53.2	7.8	2.0818
250	56.8	27.4	2.17558	53.3	5.5	2.0847

excitation when the refractive index of the fluid infiltrating the CTF increases by 0.1, i.e., $\Delta n_\ell = 0.1$. The value of the sensitivity ρ in Table A.2 is typical of the basic sensor based on the SPP waves and, in principle, should be the same as that in the TKR configuration.

Table A.2: The incidence angle θ_{peak} where the absorptance peak shows the excitation of the SPP waves and the sensitivity vs. the refractive index n_ℓ of the fluid infiltrating the CTF.

n_ℓ	1	1.1	1.2	1.3	1.4	1.5
θ_{peak} (deg)	53.7263	55.2654	56.8561	60.1694	62.0675	64.3559
ρ (deg/RIU)	15.3910	15.9070	33.1330	18.9810	22.8840	—

The advantage of the Turbadar–Otto configuration over the TKR configuration is the narrower absorptance peak of the angular absorptance spectrum obtained in the Turbadar–Otto configuration.

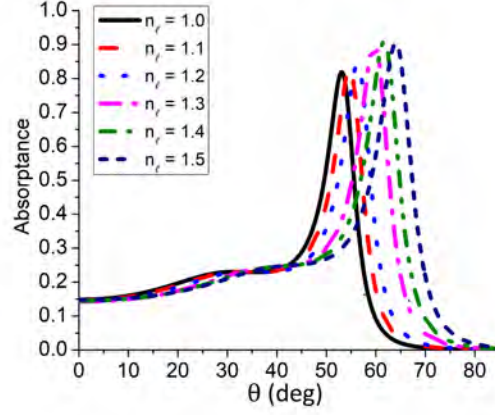


Figure A.6: Same as Fig. A.3 except that the CTF is now infiltrated with a fluid of refractive index $n_\ell = \{1, 1.1, 1.2, 1.3, 1.4, 1.5\}$, and $L_{ctf} = 200$ nm for the p -polarized incidence.

A.3 Conclusions

The SPP-waves excitation at the planar interface of columnar thin films and a plasmonic material in an experimental setup of Turbadar–Otto prism-coupled configuration was reported theoretically. The numerical results showed that the Turbadar–Otto prism-coupled configuration has an edge over the typically used experimental setup of the TKR configuration for the clearer and easier identification of absorbance peaks in the angular absorbance spectrum as absorbance peaks found in the former were narrower and easier to discern for the SPP-waves excitation. Turbadar–Otto configuration was found to be more amenable to implementation for the sensing of the gases than the liquids since the homogeneous infiltration of the thin CTFs would be very difficult. However, the development of experimental technique will pave the way for easier and homogeneous infiltration of the CTFs. The usefulness of the Turbadar–Otto configuration was also shown for the optical sensing of a fluid infiltrating the vacant spaces of the CTF.

References

- [1] E. Kretschmann and H. Raether, “Radiative decay of non radiative surface plasmons excited by light,” *Z. Naturforsch* **23**, 2135–2136 (1968).
- [2] T. Turbadar, “Complete absorption of light by thin metal films,” *Proc. Phys. Soc.* **73**, 40 (1959).
- [3] A. Otto, “Excitation of nonradiative surface plasma waves in silver by the method of frustrated total reflection,” *Z. Phys. A* **216**, 398–410 (1968).
- [4] J. A. Polo Jr., T. G. Mackay, and A. Lakhtakia, *Electromagnetic Surface Waves: A Modern Perspective*, Elsevier (2013).
- [5] S. E. Swiontek and A. Lakhtakia, “Vacuum-metal-deposition and columnar-thin-film techniques implemented in the same apparatus,” *Mater. Lett.* **142**, 291–293 (2015).
- [6] A. Lakhtakia and R. Messier, *Sculptured Thin Films: Nanoengineered Morphology and Optics*, SPIE. Press (2005).
- [7] J. A. Polo Jr., S. R. Nelatury, and A. Lakhtakia, “Propagation of surface waves at the planar interface of a columnar thin film and an isotropic substrate,” *J. Nanophotonics* **1**, 013501 (2007).
- [8] A. Lakhtakia and J. A. Polo Jr., “Morphological influence on surface-wave propagation at the planar interface of a metal film and a columnar thin film,” *Asian J. Phys.* **17**, 185–191 (2008).

- [9] T. G. Mackay and A. Lakhtakia, “Modeling columnar thin films as platforms for surface–plasmonic–polaritonic optical sensing,” *Photonics Nanostruct.* **8**, 140–149 (2010).
- [10] S. E. Swiontek, M. Faryad, and A. Lakhtakia, “Surface plasmonic polaritonic sensor using a dielectric columnar thin film,” *J. Nanophotonics* **8**, 083986 (2014).
- [11] S. E. Swiontek and A. Lakhtakia, “Influence of silver-nanoparticle layer in a chiral sculptured thin film for surface-multiplasmonic sensing of analytes in aqueous solution,” *J. Nanophotonics* **10**, 033008 (2016).
- [12] K. V. Sreekanth, Y. Alapan, M. ElKabbash, E. Ilker, M. Hinczewski, U. A. Gurkan, A. D. Luca, and G. Strangi, “Extreme sensitivity biosensing platform based on hyperbolic metamaterials,” *Nat. Mater.* **15**, 621–627 (2016).
- [13] I. J. Hodgkinson, Q. H. Wu, and J. Hazel, “Empirical equations for the principal refractive indices and column angle of obliquely deposited films of tantalum oxide, titanium oxide, and zirconium oxide,” *Appl. Opt.* **37**, 2653–2659 (1998).
- [14] T. G. Mackay and A. Lakhtakia, “Determination of constitutive and morphological parameters of columnar thin films by inverse homogenization,” *J. Nanophotonics* **4**, 041535 (2010).

Turnitin Originality Report

Surface electromagnetic waves guided by interfaces with isotropic chiral and uniaxially chiral materials by Maimoona Naheed .

From DRSM (DRSM L)

- Processed on 04-Oct-2021 07:27 PKT
- ID: 1664398178
- Word Count: 26412

Similarity Index

18%

Similarity by Source

Internet Sources:

9%

Publications:

16%

Student Papers:

2%

sources:

- 1 1% match ()
[Mackay, Tom, Noonan, James. "On electromagnetic surface waves supported by an isotropic chiral material", 'Elsevier BV', 2019](#)
- 2 1% match (publications)
[John A. Polo, Tom G. Mackay, Akhlesh Lakhtakia. "Surface-Plasmon-Polariton Waves II", Elsevier BV, 2013](#)
- 3 1% match (publications)
[Farhat Abbas, Muhammad Faryad. "A highly sensitive multiplasmonic sensor using hyperbolic chiral sculptured thin films", Journal of Applied Physics, 2017](#)
- 4 1% match (publications)
[Xuerong Xiao, Muhammad Faryad, Akhlesh Lakhtakia. "Multiple trains of same-color surface-plasmon-polaritons guided by the planar interface of a metal and a sculptured nematic thin film. Part VI: Spin and orbital angular momentums", Journal of Nanophotonics, 2013](#)
- 5 1% match (publications)
[John A. Polo, Tom G. Mackay, Akhlesh Lakhtakia. "Surface-Plasmon-Polariton Waves I", Elsevier BV, 2013](#)
- 6 1% match (publications)
[Muhammad Faryad, Akhlesh Lakhtakia. "On surface plasmon-polariton waves guided by the interface of a metal and a rugate filter with a sinusoidal refractive-index profile", Journal of the Optical Society of America B, 2010](#)
- 7 < 1% match ()
[Zhou, Chenzhang, Mackay, Tom G., Lakhtakia, Akhlesh. "Surface-plasmon-polariton wave propagation supported by anisotropic materials: multiple modes and mixed exponential and linear localization characteristics", 'American Physical Society \(APS\)', 2019](#)
- 8 < 1% match ()
[Mackay, Tom, Noonan, James. "On electromagnetic surface waves supported by an isotropic chiral material", 'Elsevier BV', 2019](#)
- 9 < 1% match ()
[Zhou, Chenzhang, Mackay, Tom G., Lakhtakia, Akhlesh. "Dyakonov-Tamm surface waves featuring Dyakonov-Tamm-Voigt surface waves", 2020](#)
- 10 < 1% match ()

Palw
Focal Person (Turnitin)
Quaid-i-Azam University
Islamabad

Professor
Department of Electronics
Quaid-i-Azam University
Islamabad